Operando Structure-Activity Profiling in Fixed-Bed Reactors using Synchrotron-Based X-Ray Techniques

Vom Promotionsausschuss der
Technischen Universität Hamburg

zur Erlangung des akademischen Grades
Doktor-Ingenieurin (Dr.-Ing.)

genehmigte Dissertation

von
Birte Wollak

aus
Hamburg

2023

1. Gutachter: Prof. Dr. rer. nat. Raimund Horn
2. Gutachter: Prof. Dr. rer. nat. Christian G. Schroer
Tag der mündlichen Prüfung: 05.06.2023
https://doi.org/10.15480/882.5162

Abstract

It is a long-term goal of modern heterogeneous catalysis research to understand, model, and predict complex phenomena that occur inside catalytic reactors in space and time. This is a challenging task due to the complicated interplay between mass transport, heat transport, catalytic reactions, and catalyst dynamics. A crucial step towards reaching this goal is to resolve the strong gradients found in fixed-bed reactors and further to combine catalyst activity with catalyst property measurements under realistic operation conditions by means of *operando* techniques. Due to the high experimental complexity of combining spatial profiling methodologies with *operando* techniques, most studies measure either catalyst activity or catalyst properties in a spatially-resolved manner. Only in a limited number of studies, both sides of the chemical system were measured spatially-resolved (*operando* profiling). To date, *operando* profile experiments are mainly restricted to laboratory-based characterization techniques such as Raman spectroscopy.

In this work, the catalyst characterization portfolio for *operando* profile studies was extended to X-Ray Absorption spectroscopy (XAS) as well as X-Ray Diffraction (XRD) using synchrotron radiation. Both techniques provide highly complementary information, representing a beneficial combination to obtain detailed structural information about the catalyst during operation. While XAS spectra reveal bulk average metal oxidation states of the probed catalyst, XRD patterns allow to deduce crystalline phases in a qualitative and quantitative manner. For the synchrotron-based *operando* profile experiments, a lab-scale catalytic profile reactor setup is presented, capable of simultaneously measuring spatially-resolved temperature, concentration, and catalyst structure in transmission geometry. Since *operando* profile measurements coupled to XRD and XAS are not feasible with laboratory-based X-ray sources, a significant unexploited potential in spatially-resolved *operando* catalysis research was accessed in this work.

To validate the new methodologies, the oxidative dehydrogenation of ethane to ethylene over a MoO_3/γ-Al_2O_3 catalyst was used as a test system. This system was chosen because the catalyst has a dynamic and reversible reduction/reoxidation behavior with pronounced changes in color, performance and structure. Species concentration profiles show how the catalyst changes its reaction mechanism from oxidation to steam reforming and water-gas-shift reactions with increasing reaction progress along the catalyst bed. In combination, the bulk molybdenum oxidation state deduced from XAS and the crystalline phase composition obtained from XRD reveal distinct structural changes due to catalyst reduction.

This work demonstrates the strengths of *operando* profile studies at synchrotron radiation facilities by providing a comprehensive insight into the catalytic reactor under operation. This newly gained knowledge can have major beneficial implications for the development of detailed reactor models, resulting in a more accurate, efficient and sustainable optimization of catalytic processes in the future.

Contents

1 Introduction

Catalytic fixed-bed reactors are among the most commonly utilized reactors in the chemical and petrochemical industry [1–3]. In fixed-bed reactors, the reaction mixture flows through and around solid catalyst particles, which are fixed in space. The purpose of the catalyst is to accelerate the rate of the desired reaction path the system is capable of. To achieve a high efficiency of industrial catalytic reactors, usually an optimization process is performed, in which high-throughput screening experiments are applied [4–6]. In those sets of measurements, the catalyst activity, selectivity, and deactivation behavior are examined by correlating the in- and outlet flows of the reactant and product phase ("end of pipe"), respectively, under a wide range of process conditions, e.g., temperature, pressure, gas flow rate, and different feedstocks. Consequently, the screening requires a large number of trial and error experiments and is therefore very time consuming. Furthermore, the end of pipe analysis treats the reactor itself and the catalyst as a black box, resulting in a deficiency in the fundamental understanding of catalysts and the actual processes inside the reactor. This unsustainable conventional optimization approach is still considered the state of the art in industrial chemistry.

A major goal in modern heterogeneous catalysis research is to promote a time and resource-efficient development and optimization of catalytic reactors and catalysts. A crucial step towards this goal is to unravel complex catalyst structure-activity relationships in order to tune the material properties and change the process conditions for the required chemical outcome [7, 8]. The field of *operando* research techniques evolved to meet this crucial challenge [9–12], aiming to gain an in-depth understanding of the underlying processes through multimodal experimental approaches [13–17] and detailed modeling [18, 19].

Operando measurement concepts in catalysis combine catalytic activity measurements (gas composition and temperature analysis) with structural characterization (spectroscopic and scattering techniques) under industrially-relevant reaction conditions, i.e., in the relevant working state of the catalyst. The latter is of particular importance due to the dynamic behavior of catalytic materials, demonstrated in various in-situ and *operando* studies [20–22]. In simplified terms, this means that the chemical composition, surface or bulk structure, type and number of active sites and defects, as well as electronic properties of a catalyst are strongly influenced by temperature, pressure, flow velocity, and composition of the reaction mixture. Since structural changes on the atomic level also induce changes in chemical properties, catalyst dynamics have a direct impact on catalytic performance. Hence, it is crucial to derive catalyst structure-function relationships in relevant and well-defined reaction conditions. This is where the field of *operando* measurements separate themselves from ex-situ and in-situ ones.

Multimodal *operando* measurement concepts aim to combine multiple techniques within the same reactor covering as much relevant information as possible on various space and time scales [13–17, 23]. This includes the simultaneous application of catalyst characterization methods that provide highly complementary information and the combination with spatially-resolved measurement techniques to address spatial heterogeneity within catalytic reactors. Spatially-resolved measurements are implemented as a relatively common tool in *operando* catalysis research, providing localized information throughout the entire catalyst bed [24–26]. Most *operando* reactor systems allow the measurement of catalyst properties in a spatially-resolved manner. Concentration and temperature information are obtained at both the reactor in- and outlet. One example is the standard quartz Capillary Micro-Reactor (CMR). The small sample sizes of CMRs, typically less than 1.5 mm diameters, make this reactor system compatible with various X-ray characterization tools [27–30] and almost universally applicable to study small powder samples. Larger reactor diameters (> 4 mm) are predominantly applied in *operando* studies using high-energy X-rays [31–35]. High-energies are required to provide sufficient penetration power to measure reliably through rather thick reactor diameters. However, compared to CMRs, it is obvious that larger reactor diameters provide a more realistic sample environment and also offer the opportunity to apply the capillary sampling technique developed by Horn et al. [36, 37]. Here, a sampling capillary runs through the center of the catalyst bed, allowing to resolve concentration and temperature information along the catalyst bed. The simultaneous measurement of spatially-resolved gas composition, temperature, and catalyst property profiles is referred to as *operando* profiling in this work. Normally, due to the high experimental complexity involved in the development of appropriate *operando* profile reactor systems and implementation of *operando* profile experiments, most studies measure either catalyst activity or catalyst property in a spatially-resolved manner, hence addressing only one side of the chemical system in a given experiment.

In the last decade, laboratory studies have demonstrated the strengths of *operando* profile measurements using spectroscopic methods, e.g., Raman-spectroscopy [22, 38] and laser-induced fluorescence spectroscopy [39]. In these studies, measurements are carried out in reflection mode or through spectroscopic fibers. The use of synchrotron radiation and the versatile tools available at synchrotron light sources could significantly expand the characterization portfolio of such experiments, because measurements through rather thick reaction tubes in transmission can be carried out. This technique has gained traction in the last decade, string with the pioneer work conducted by Stewart et al. [40], in which X-ray absorption spectroscopy (XAS), concentration, and temperature profiles through a powdered catalyst bed under industrial conditions was simultaneously determined for the first time. The applied heating technique has the drawback that a uniform heating along the catalyst bed cannot be achieved, as described by Newton et al. [41]. This is especially problematic for larger reactors and sample sizes, because it can result in unrealistic or unrepresentative structural and chemical gradients due to non-uniform process conditions. To date, there is still a lack of kinetically well-defined and established *operando* profile reactor systems at synchrotron radiation sources, which can be considered untapped potential with respect to *operando* catalysis research.

The aim of this work is the extension of the *operando* profiling methodology with powerful synchrotron-based characterization methods by a proof of principle and highlighting their potential at the same time. For this purpose, a catalytic profile reactor setup in lab-scale was developed that allows the simultaneous acquisition of local catalyst activity and structural information by means of synchrotron-based X-ray techniques in transmission mode. The new *operando* profiling methodologies were developed for XAS and X-ray diffraction and validated using the oxidative dehydrogenation of ethane to ethylene (ODH) over a supported molybdenum oxide catalyst as a test reaction system. The chosen chemical system shows distinct catalyst dynamics in color, performance and structure as well as structural reversibility as a function of the reaction environment. Furthermore, the system combines the advantages of being relatively well understood, having a comparably low degree of complexity due to only one transition metal of interest, and easy to handle gas phase species. While the system serves as a model system, gaining a fundamental understanding of different oxygen species on selectivity along with the development of highly-selective catalysts play a decisive role in optimizing selective oxidation catalysis processes.

2 Theoretical Background

This chapter gives an overview of spatial profiling in *operando* catalysis research and the methods used in this thesis. Firstly, an introduction to heterogeneous catalysis with a focus on Oxidative Dehydrogenation (ODH) of hydrocarbons is given. Thereafter, the state of the art of profile reactors for catalyst activity profiling and *operando* structure-activity profiling are reviewed. Subsequently, synchrotron radiation sources are introduced, followed by explaining the fundamentals of synchrotron-based X-ray Absorption Spectroscopy (XAS) and X-ray Diffraction (XRD). Finally, details on Gas Chromatography (GC) and Mass Spectrometry (MS) are briefly described.

2.1 Introduction to Heterogeneous Catalysis

In heterogeneous catalysis, the phase of the catalyst differs from the phase of reactants and products. In this section, the focus lies on gas-solid phase reactions, where the catalyst is present in the solid phase while the reactants and products in the gas phase, due to its relevance in this work. Heterogeneously catalyzed reactions play a key role in the economic and ecologic efficiency of many industrially relevant processes [1,3,7,42]. Catalysts that contain transition metals are utilized for the production of fuels, energy carriers, and important base chemicals [42]. For instance, in the Haber-Bosch process the hydrogenation of nitrogen to ammonia is catalyzed by iron oxide catalysts [42,43], in the Ostwald-process Pt-Rh catalysts are used for ammonia oxidation to form nitric acid [42,44], in steam reforming Ni catalysts are applied to produce synthesis gas [42,45], from which methanol is generated using Cu catalysts [42], and in the contact process sulfuric acid is produced by V-oxide catalysts [42]. An overview of the reactions of these processes is given in Eq. 2.1 – 2.5.

$$N_2 + 3\,H_2 \rightleftharpoons 2\,NH_3 \tag{2.1}$$

$$4\,NH_3 + 5\,O_2 \longrightarrow 4\,NO + 6\,H_2O \tag{2.2}$$

$$CH_4 + H_2O \rightleftharpoons CO + 3\,H_2 \tag{2.3}$$

$$CO + 2\,H_2 \rightleftharpoons CH_3OH \tag{2.4}$$

$$2\,SO_2 + O_2 \rightleftharpoons 2\,SO_3 \tag{2.5}$$

The above-mentioned reactions are carried out in catalytic fixed-bed reactors. In this type of reactor, a solid catalyst remains fixed in space and the reaction mixture flows through and around the catalyst. The catalyst can either be in the form of particles, which are randomly packed into a catalyst bed, as is the case in steam reforming over supported nickel catalysts, or structured, as in the case of gauzes applied in ammonia oxidation [3, 42]. There are various modifications to fixed-bed reactors to suit the individual process requirements that overall aim to maximize the target variables conversion, selectivity, and yield under safe process operation. For instance, multitubular reactors are used for strongly exothermic or endothermic reactions, enabling a high rate of heat removal or supply, or fluidized bed reactors that allow removing the catalyst for regeneration from the reactor.

To design a fixed-bed reactor the rate law must be derived from experimental observations. The rate law is a mathematical description that correlates the reaction rates of reacting species with the reaction conditions (temperature, pressure, species concentration, catalyst). The rate law allows us to obtain the design equation, which expresses the reaction rate of component i as a function of conversion ($-r_i = f(X)$), that is required to size any reactor [46] (Eq. 2.6).

$$r_{i,m_{cat}} = \frac{1}{m_{cat}} \frac{dn_i}{dt} \tag{2.6}$$

The presence of strong concentration and temperature gradients as well as transport effects within catalytic reactors result in a varying reaction rate with the position in the reactor. In order to obtain the pure rate law of a catalytic reaction, kinetic measurements are performed in laboratory kinetic test reactors that possess a well-defined mixing behavior and reaction conditions. Furthermore, good contact between catalyst and gas phase reactants, as well as the absence of transport effects, must be ensured [3, 47, 48]. A common kinetic test reactor is the differential plug flow reactor, which is often used in high-throughput screening experiments [4–6]. The latter, as their name implies, are measurement concepts consisting of a large number of test reactors, designed to screen the performance and deactivation behavior of catalysts as a function of operating conditions. In this way, the best catalyst is selected from several hundred catalytic materials.

However, a major drawback of this catalytic testing approach, also known as the "black box approach", is that only the reactor in- and outlet flows are correlated. The catalytic processes occurring within the fixed-bed remain hidden, leaving a lack of fundamental understanding of the actual processes inside the reactor. Therefore, new measurement concepts and research reactors are developed, aiming to resolve the strong gradients inside the catalytic reactor under operation, introduced in Subsection 2.2.1.

Further, complex experimental concepts come strongly into focus which combine catalyst activity with structural investigations of the catalyst, known as *operando* measurements (Subsection 2.2.2). By using *operando* methodologies, the reaction mechanism or catalyst dynamics can be analyzed in response to temperature, total pressure, or composition of the reaction mixture. Nowadays, the importance of catalyst dynamics is widely known and the subject of modern catalysis research, aiming to unravel the structure-activity relations of catalysts. The rather dynamic behavior of catalysts applied in selective oxidation catalysis research for producing olefins and proposed reaction mechanisms are part of the next subsection.

2.1.1 Oxidative Dehydrogenation of Alkanes

Light olefins such as ethylene and propylene are base chemicals, which are considered as basic building blocks in the manufacture of important chemical products [49, 50]. The main process for the production of ethylene and propylene is steam cracking of hydrocarbons [51, 52]. The process consists of several steps, including the mixing of a hydrocarbon feed with steam, then heating the mixture for milliseconds to around 850 °C, followed by rapid cooling of the mixture [51, 53]. The strong heat treatment splits or "cracks" the hydrocarbons into smaller components. Steam cracking is carried out in large tubular reactors heated by furnaces, called steamcrackers. Conventional hydrocarbon feedstocks are fossil naphtha or natural gas. [51, 53]

Steam cracking is one of the most energy-intensive processes in the chemical industry due to the highly endothermic nature of the thermal cracking and the high process temperatures required for operation [54]. The high temperature is realized by burning fossil fuels. This, in addition to the fossil-based feedstock inputs, makes stream cracking responsible for more than 300 million tonnes CO_2 global emissions per annum [55]. Under consideration of reaching the goals of the Paris Agreement for climate neutrality of the European Union by 2050 [56], the replacement or modification of existing energy and fossil raw material intensive processes such as steam cracking is crucial for the chemical industry.

Strategies to replace fossil feedstock inputs with renewable or recycled feedstocks are planned, as well as to implement a more sustainable energy supply of steamcrackers [55], currently tackled by a cooperation of BASF, SABIC, and Linde for the development of electrically heated steam cracker furnaces [57]. When electricity is generated from renewable sources, the new technology has the potential to reduce CO_2 emissions by as much as 90 % [57].

A more selective alternative route of olefin production, compared to thermal catalytic cracking applied in steamcrackers, is the direct catalytic dehydrogenation of alkanes [51, 58, 59].

$$\mathrm{C}_n\mathrm{H}_{2n+2} \rightleftharpoons \mathrm{C}_n\mathrm{H}_{2n} + \mathrm{H}_2 \tag{2.7}$$

$$-RT \ln K_p = \Delta G^0_{C_nH_{2n}} - \Delta G^0_{C_nH_{2n+2}} \tag{2.8}$$

However, alkanes are very unreactive and as is the case for cracking reactions, also alkane dehydrogenation reactions are endothermic reactions. The thermodynamic equilibrium is on the alkane side at low temperatures which induce the need of high process temperatures for obtaining economically attractive olefin yields. By introducing a hydrogen acceptor such as oxygen the dehydrogenation reaction becomes strongly exothermic, reducing the energy required in operation, and further shifting the thermodynamic equilibrium far to the alkene side, which allows to consider the reaction as irreversible [58]. Additionally, the presence of oxygen largely eliminates coke deposition [58]. This catalytic reaction is known as ODH (Eq. 2.9).

$$C_nH_{2n+2} + 0.5\,O_2 \rightleftharpoons C_nH_{2n} + H_2O \tag{2.9}$$

$$-RT\ln K_p = \Delta G^0_{C_nH_{2n}} + \Delta G^0_{H_2O} - \Delta G^0_{C_nH_{2n+2}} \tag{2.10}$$

ODH processes are not industrially implemented yet. Besides facing technical challenges related to the process, e.g., temperature control at high heat formation rates, sufficient heat removal to prevent run-away, flammability and explosivity of the hydrocarbon-oxygen mixture, severe constraints are imposed for producing alkenes selectively [58, 60, 61]. To illustrate this point, a reaction mixture of hydrocarbons mixed with oxygen provides a complex network of possible consecutive and parallel reaction pathways, forming oxygenates as aldehydes, acids, or total oxidation products. Concerning the ODH of ethane to ethylene, used as a test reaction in this work, the direct oxidation of ethane or further oxidation of ethylene is likely to occur, both reducing ethylene selectivity. Especially, due to the higher reactivity of ethylene compared to ethane, consecutive reactions of ethylene are prone to take place. Ethylene is an intermediate, obtained by kinetic control, since thermodynamics favor carbon dioxide and water formation. Therefore, catalysts that are tailored for accelerating the desired reaction pathways, i.e., the abstraction of hydrogen to form alkenes (k_1) as target product, and at the same time hinder other pathways towards oxygenates or carbon oxides (k_2, k_3), plays a decisive role for process efficiency, simplified illustrated in Figure 2.1 [58, 59].

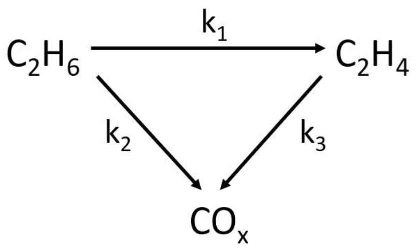

Figure 2.1: Simplified reaction scheme of ethane ODH.

Transition metal or transition metal oxide catalysts based on Mo and V, supported on oxides of alumina, silica, and titania, have shown promising performance in selective oxidation catalysis with distinct catalyst dynamics [51,62]. These catalysts actively participate in hydrocarbon oxidation reactions and show considerable changes in their redox states. The oxide ions in the catalyst lattice are in equilibrium with the gas phase oxygen, i.e., each having the same chemical potential [58].

$$\mu_{chem,O_2} = \mu_{chem,O^{-2}} = \mu^0_{chem,O_2} + RT\ln p_{O_2} \tag{2.11}$$

A change in the chemical potential of oxygen in the gas phase induces a change in the stoichiometric composition of the catalyst [58].

$$(\text{metal:oxygen})_{\text{oxide}} = f(p_{O_2}) \tag{2.12}$$

Therefore, distinct oxygen concentration gradients along a catalyst bed affect and directly change the structural composition.

In catalysis research, particular focus is given to the role of different oxide species on catalytic performance, including lattice, catalyst surface, and bulk phase oxygen [63, 64]. A basic understanding of selectivity in selective oxidation catalysis was given by Haber's concepts of electrophilic and nucleophilic oxidation reactions [64,65]. Here, reactions proceeding via initial oxygen activation result in the formation of strongly electrophilic oxygen species that attack C-C bonds and favor total oxidation reactions, whereas nucleophilic oxidation reactions start with hydrocarbon activation favor selective hydrogen abstraction and nucleophilic oxygen insertion [65]. Mars-Van Krevelen (MVK) proposed a mechanistic description for selective oxidation reactions over transition metal oxide catalysts [66], in which all hydrocarbon reactions occur via lattice oxygen. In this reaction process, the hydrocarbon molecule must first absorb on the catalyst surface. The catalyst provides lattice oxygen for hydrocarbon oxidation, which creates an oxygen vacancy and in turn reduces the catalyst. The oxygen vacancy is refilled by gaseous oxygen and thereby re-oxidizing the catalyst.

In this work, ODH of ethane was performed on a supported molybdenum oxide catalyst. This catalyst possesses poor performance in terms of ethylene selectivities, but presents a good model system for method development due to its distinct catalyst dynamics [22] and its reduced chemical complexity. The knowledge obtained from this model system builds the framework to study more complex, multi-element molybdenum oxide catalytic materials with outstanding catalyst performance in selective oxidation catalysis [62, 67, 68]. A prominent example is the M1 phase catalyst [68–70], consisting of an MoVTe oxide phase.

2.2 Profile Reactors in Heterogeneous Catalysis

The development of improved catalysts and catalytic processes requires knowledge of the involved processes within catalytic reactors. Catalytic profile reactors have been established to meet this challenge, allowing to resolve the strong gradients in fixed-bed reactors. In this section, the current states of research in the development and application of profile reactors for measuring spatially-resolved concentration and temperature information along the catalyst bed as well as *operando* profile reactors, that add structural information about the catalyst, are described.

2.2.1 Profile Reactors for Catalyst Activity Profiling

In order to follow the chemical evolution along the catalyst bed (e.g., concentrations of reactants, intermediates, products as well as temperatures), spatial resolution techniques have been developed [24,25]. Compared to the black box approach, the accessible information content in the catalytic process is significantly enlarged by using spatially-resolved measurement techniques. To illustrate this point, inlet and outlet concentrations measured in the black box approach provide a single kinetic data point for a set of reaction parameters, whereas spatially-resolved approaches scan over a broad range of kinetic data points within one experiment.

To obtain spatially-resolved reactor data novel reactor concepts such as the Zapfstellenreaktor [3] were developed. These novel reactor concepts are capable of measuring the gas composition and temperature information at discrete points along the catalyst bed. The gas samples are withdrawn through a fixed number of lateral sampling ports (typically less than ten). The same sampling ports allow to insert a thermocouple for obtaining local temperature information. Major drawbacks of the Zapfstellenreaktor are the fixed and low number of sampling points, often resulting in insufficiently resolved axial gradients in between the sampling points. Furthermore, gas samples are taken close to the reactor wall, a region that is affected by flow channeling in packed beds due to higher void fractions as well as by heat transfer processes to the reactor walls. As a consequence, sampled gas compositions are not representative of the radially averaged gas composition at the actual bed position [3].

To overcome the drawbacks of the Zapfstellenreaktor, Horn et al. [36, 37] developed the capillary sampling technique which allows us to measure species profiles with significantly higher resolution in addition to taking gas samples from the center of the catalyst bed. A schematic representation describing the working principle of the capillary sampling technique is shown in Figure 2.2.

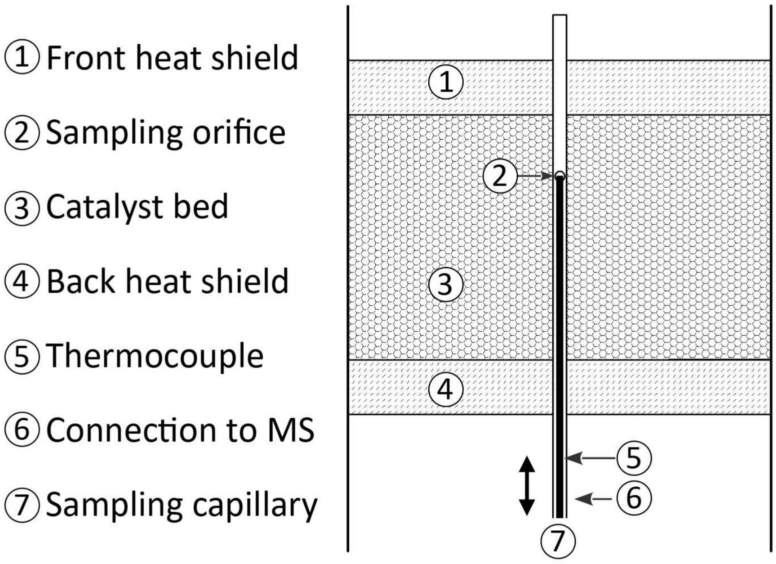

Figure 2.2: Working principle of the capillary sampling technique developed by Horn et al. adopted from [36].

In this case, a small orifice is drilled into a capillary. Through the orifice, gas samples are continuously extracted and analyzed by various analytical devices like gas chromatography [71], MS [36], and Fourier-transform infrared spectroscopy [72]. The capillary and thus the orifice is positioned at any axial position within the catalyst bed with μm resolution through the centerline of the catalyst bed by using a translation stage [36]. The diameter of the sampling orifice is a compromise between spatial resolution, the sampling flow rate, and the transfer time to the analytical instrument. A thermocouple [36] or pyrometer fiber [71, 73] located within the sampling capillary, tip-aligned with the sampling orifice, enables the simultaneous measurement of gas phase or solid phase temperature profiles. Notably, since the profile technique uses a physical probe, i.e., the capillary within the reactor, it is important to consider the invasiveness of the sampling methodology. For example, by reducing the invasiveness on the hydrodynamic flow conditions by adjusting a low sampling flow rate from the reactor. However, so far the usage of physical probes located outside of the reactor provides no adequate alternative for resolving species concentration and temperatures within fixed-beds.

The introduced profile methodology was the basis for the development of many highly-specialized profile reactor setups and the founding of Reacnostics GmbH, a spin-off from TUHH, in the working group of Horn. For example, a bench scale profile reactor was developed, coping with extreme process operation conditions up to 1300 °C and up to 45 bar, for investigating the Catalytic Partial Oxidation (CPO) of methane to synthesis gas on different randomly packed or shaped catalysts, among other reactions [73, 74]. Another profile reactor setup in bench scale was developed, tailored for studying ammonia oxidation under industrial conditions as part of the Ostwald process [75]. Here, profile experiments were combined with detailed CFD simulations for gaining a deeper understanding of the measured phenomena. The capillary sampling technique was further adopted to other profile reactor systems at Queen's University Belfast and Karlsruhe Institute of Technology (KIT). At Queen's University Belfast the Spatially Resolved Capillary Inlet Reactor System for Fixed Beds (SPACI-FB) was developed. Spaci-FB is a laboratory-sized profile reactor, whose working principle was demonstrated by the oxidation of carbon oxide promoted by hydrogen over a Pd catalyst [76–78]. This principle of the spatial profile measurement technique with the Spaci-FB reactor is similar to that described earlier in this subsection. The main difference is that the catalyst bed is translated vertically, instead of a roto-translational movement of the capillary, illustrated in Figure 2.3. The probe volume, formed by sampling orifice and thermocouple, remains fixed in space. The reactor tube containing the catalyst bed is shifted laterally along this probing volume with micrometer resolution.

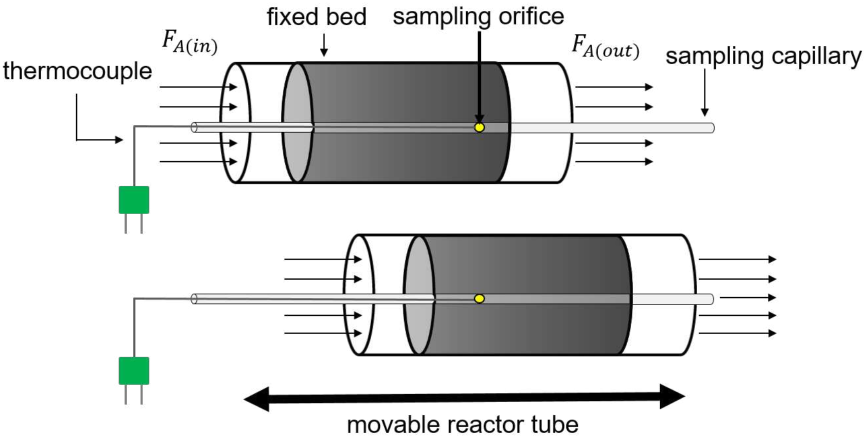

Figure 2.3: Working principle of the spatial profile measurement technique by moving the reactor tube while the capillary and thereby the sampling orifices remain fix in position. F denotes the molar flow rate of a chemical species in the reaction mixture.

One drawback of this reactor design involves the use of hot air blowers as heating systems. Even though the applied hot air blower was equipped with a specially designed nozzle [77], Newton et al. demonstrated that uniform heating along the catalyst bed employing hot air is difficult to achieve [41]. This is especially problematic with larger reactors and sample sizes, and can feasibly result in unrealistic or unrepresentative chemical gradients due to non-uniform process conditions.

A further example for lab-scale profile reactor setups was introduced by Serrer et al. [79] from KIT to study axially resolved profiles of gas phase composition and temperature along a Ni/γ-Al_2O_3 and a NiFe/γ-Al_2O_3 catalyst during carbon dioxide methanation. Here, the combination of local temperature and gas composition analysis revealed a hotspot in the first-third of the fixed-bed, which led to CO formation as an undesired by-product. To achieve uniform heating of the catalyst bed, an oven unit encloses the fixed-bed. However, the reactor design is not tailored for flexible and fast setup assembly. This aspect was tackled by Reacnostics GmbH who introduced the Compact Profile Reactor (CPR) onto the market, capable of simultaneously measuring spatially-resolved gas composition and temperature information through catalytic fixed beds. As the name implies, the CPR design is tailored to provide a compact as well as integrated profile reactor in laboratory size, enabling flexible and straightforward reactor integration for various applications. The CPR is already widely used in various research facilities and applications. A pioneering example for studying and further revealing new insights into the complex reaction mechanism of iron-based Fischer-Tropsch synthesis by concentration profiles is shown by Wolke et al. [80]. The application portfolio was further extended to liquid phase reactions in the master thesis of Andrés Aquino from TUHH [81], who studied propylene epoxidation to propylene oxide on titanium silicalite (HPPO-Process).

Overall, spatial gradients resolved by the profile measurement technique by Horn et al. provide valuable kinetic and mechanistic information about the reaction under study. In combination, several studies demonstrated the particular synergy effects between spatially-resolved catalyst activity data and theoretical investigations through the development and validation of more detailed models and CFD simulations [75, 82, 82, 83]. Such detailed theoretical models of a reaction system give, for instance, insight to why there is a change in the performance of a catalyst and are therefore essential for gaining a deeper understanding of the actual processes within fixed-bed reactors.

The measurement of catalyst performance via spatially-resolved gas phase composition and temperature analysis, described to this point, considers only one part of the chemical system. Since catalytic performance and structure are inseparably linked, the simultaneous measurement of catalyst structure-function relations represents a promising approach for revealing complex reaction mechanisms. Such measurement concepts require highly-specialized reactor setups, which is the focus of the next subsection.

2.2.2 *Operando* Profile Reactors for Structure-Activity Profiling

The field of in-situ and *operando* research evolved to answer challenging questions about the interplay of the chemical evolution and the catalyst structure [9–12]. Questions that can be answered using these techniques are: How do change catalysts their structure according to local reaction conditions, how do structural changes influence catalytic performances, and how can catalytic processes be systematically optimized for a given application.

The terms in-situ and *operando* have no clear definition. In this work the terms are defined as follows: in-situ measurements comprise experiments that are conducted in specific atmospheres different from the reaction, e.g., switching between artificial oxidative or reductive gas atmospheres such as oxygen or hydrogen in nitrogen. Here, structural changes in the catalyst are induced and measured, and at the same time, the gas atmosphere and temperature are precisely monitored. In contrast to in-situ, *operando* experiments cover the simultaneous measurement of catalyst performance and catalyst structure during industrially relevant and kinetically well-defined reaction conditions. In other words, *operando* experiments represent a holistic approach to study the chemical system in its relevant working state by revealing structure-activity relations of interest for the process under investigation.

In the last two decades, *operando* research has been established as a substantial field in catalysis research [8–12], going hand-in-hand with the development of new *operando* reactor concepts that enable optical access to the reactor bed for various characterization techniques combined with catalyst activity measurements. Prominent examples of *operando* reactor concepts are reactor cells [84, 85], Capillary Micro-Reactors (CMRs) (ID < 1.5 mm) [29, 86], larger tubular fixed-bed reactors (ID > 4 mm) [31–35], and profile reactors [22, 38–40] – all having unique strengths and limitations. Hence, the choice of an appropriate *operando* reactor strongly depends on the goals of the study, the requirements of the characterization technique as well as the operating conditions of the process.

Reaction cells are typically designed for a certain or multiple spectroscopic, scattering, or related catalyst characterization techniques and thus, are highly specialized with rather no limit to the application of available techniques. Each characterization technique captures certain information about a given chemical system. Since catalytic phenomena occur on various space and time scales the usage of different techniques, as well as their combination, is often preferred to gain a deeper understanding. In most reaction cells, catalyst properties are obtained at one measurement point within the catalyst bed, while the temperature information is measured close to the catalyst bed and gas compositions are analyzed at the reactor in- and outlet flows. However, apart from the informative value of *operando* data by using different characterization techniques, the quality of the data plays a decisive role in deducing meaningful correlations of the system. Many reaction cells are optimized towards the spectroscopic method, but are restricted to specific reaction atmospheres (field of in-situ) and often kinetically ill-defined. The latter results in non-uniform process conditions and can easily lead to falsified structure-activity correlations [87].

The abovementioned limitations of many spectroscopic cells were overcome with the development of CMRs, which have plug flow geometry. CMRs are widely used in *operando* catalysis research [27–30]. The small sample sizes are heated via one or two hot air blowers. Hot air blowers enable easy access to the reactor for spectroscopic analysis and make high process temperatures up to 900 °C feasible. Consequently, CMRs are compatible with diverse characterization techniques and are therefore widely used with X-ray techniques at synchrotron radiation facilities. A recent extension of the standard CMR setup is the aRCTIC setup [86], which utilizes a rotatable CMR. By adding the rotation dimension hard X-ray tomography measurements become feasible. Additionally, both systems allow studying the catalyst in spatially-resolved manner, simply by moving the entire reactor system in μm ranges along the catalyst bed. The increased information content achievable in this way and the rather straightforward use of the CMR coupled to spatial profiling and comparable *operando* profile reactor systems have led to their implementation as a relatively common tool in *operando* catalysis research. However, the small sample sizes of CMRs allow us to measure only the catalyst in a spatially-resolved manner, while concentration and temperature measurements are restricted to the reactor in- and outlet.

In this work, the simultaneous measurement of concentration, temperature, and catalyst property information in a spatially-resolved manner is carried out, referred to as *operando* profiling or spatially-resolved structure-activity profiling. *Operando* profiling methodologies involve high experimental complexity. To illustrate this point, such experiments require to insert a (moveable) gas sampling device (e.g., capillary sampling technique) in the catalyst bed, to make the reactor bed optically accessible for various characterization techniques, and at the same time to enable well-defined reaction conditions of larger reactor diameters along the entire catalyst bed. A comparison between typical reactor sizes applied in CMRs versus *operando* profile reactors is illustrated in Figure 2.4. As a result of these demands on the reactor setup, most studies measure either catalyst activity (see Subsection 2.2.1) or catalyst properties in a spatially-resolved manner, hence addressing only one side of the chemical system in a given experiment.

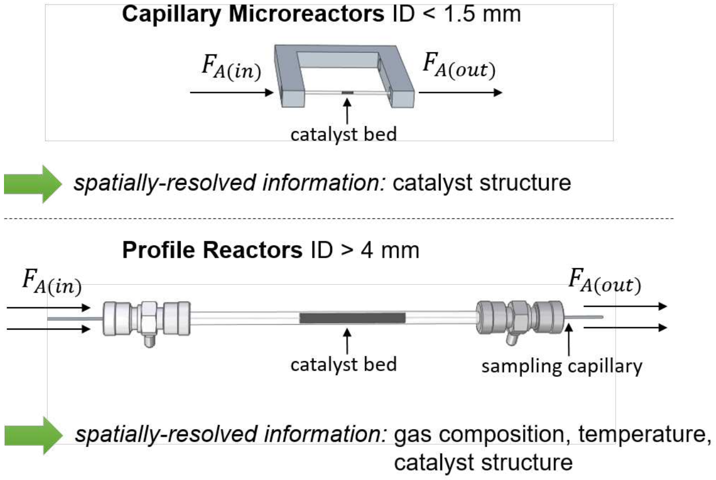

Figure 2.4: Typical sizes of CMRs (top) compared to *operando* profile reactor systems (bottom). F denotes the molar flow rate of a chemical species in the reaction mixture.

Few laboratory studies have demonstrated the strength of combined spatially-resolved *operando* measurements, combining the profile measurement technique developed by Horn et al. [36,37] with spectroscopic methods. A schematic overview of this *operando* methodology is shown in Figure 2.5.

By placing spectroscopy fibers inside the sampling capillary, spatial concentration, temperature, and spectroscopic reactor profiles were measured along the centerline of the catalyst bed. Using this approach, spatially-resolved *operando* Raman spectroscopy [22], pyrometry [71,73], and laser-induced fluorescence spectroscopy [39] were performed. An additional approach is to combine the profile measurement technique with an electromagnetic probe located outside of the reactor. The CPR, introduced in the previous Subsection 2.2.1, is equipped with an external optical window allowing to direct Raman light from the outside onto the

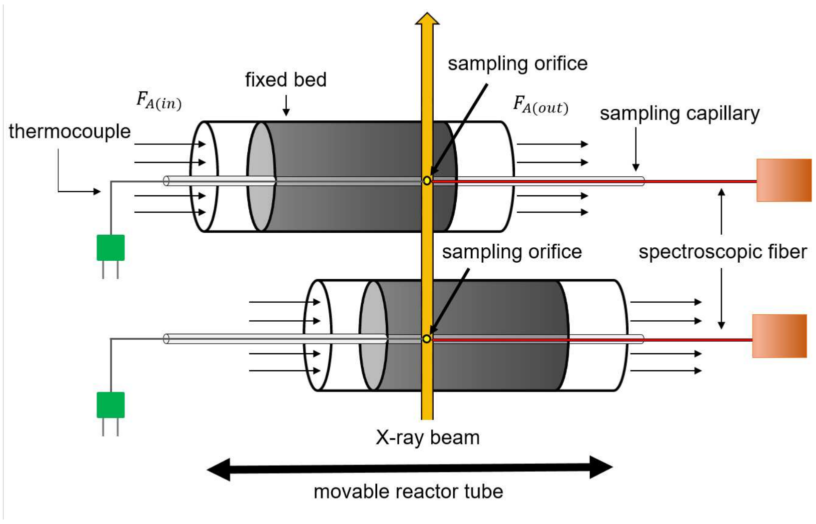

Figure 2.5: Extension of the spatial profile measurement technique by measuring localized structural information using spectroscopic fibers located inside the sampling capillary to transmit laser light onto the sample, or by passing the laser/X-ray beam from the outside on the sample through the reactor tube wall. F denotes the molar flow rate of a chemical species in the reaction mixture.

sample through the reactor tube and collecting the reflected light on the same way back. This measurement configuration is known as reflection mode and was carried out to study propane dehydrogenation over gallium–platinum supported catalytically active liquid metal solutions [38]. The catalytic performance profiles showed an enhanced deactivation of the catalyst at the end of the catalyst bed. Raman spectroscopy complemented this observation by revealing an increased formation of carbon deposits in this bed range.

The rather thick reactor diameters (4 – 6 mm Inner Diameter (ID)) applied so far restrict spatially-resolved *operando* profiling to measurements in reflection mode or using spectroscopic fibers. For measurements in other configurations such as transmission mode an intense X-ray source is required, as provided by synchrotron radiation facilities (see Section 2.3). Furthermore, the environment of experts and the versatile tools available at synchrotron light sources significantly improve the development of new measurement concepts. However, in addition to the high experimental complexity, synchrotron studies have strict time constraints for setup assembly and performing the actual experiment, as well as usually limited space for the accommodation of large setups at the beamline.

Therefore, a quasi-simultaneous or sequential approach to study CO_2 methanation over Ni-based catalysts was used by Serrer et al. [79]. In this study, Serrer et al. compared concentration and temperature profiles obtained in a lab-scale profile reactor (Subsection 2.2.1) with local structural information obtained by quick-XAS in a CMR. Similar reaction conditions were achieved in the two reactor systems that differed in scale, heating concepts, contact times, and gas dosing systems. However, in order to correlate reactive structure observations from multiple sources, it is optimal to conduct experiments under the very same reaction conditions.

The SPACI-FB reactor system, introduced in the previous chapter, was extended to SPACI-FB-XAFS and for the first time used to perform the simultaneous measurement of XAS, concentration and temperature profiles through a powdered catalyst bed under industrial conditions at the Diamond Light Source, UK [40]. The combined spatial profile approach provided previously unobserved insights into the nature of the promotional effect of H_2 on the oxidation of CO. Related to the heating system, also the SPACI-FB-XAFS system applies only one hot air blower and thereby does not overcome earlier drawbacks of the SPACI-FB system (Subsection 2.2.1), resulting most likely in non-uniform temperature conditions and thereby unrealistic or unrepresentative structural and chemical gradients [41]. To illustrate the impact on data quality in *operando* profile experiments: For precise catalyst structure-activity correlations, fixed-bed tubular reactors need to fulfill plug flow behavior and the reaction temperature needs to be known along the entire length of the catalyst bed, excluding the presence of significant radial gradients in temperature or concentration. In contrast, in kinetically ill-defined systems with non-uniform process conditions resulting from channeling, bypass flows, dead volumes or insufficient heat removal or supply, the kinetic parameters are non-uniform. In turn, the catalyst sees different local reaction conditions and adapts its performance and structure accordingly. Concentration and temperature information are measured in the center of the catalyst bed, representing the values for a given axial position in radial direction, equal to the X-ray technique that produces radially averaged data at a fixed axial position. The presence of strongly varying local reaction conditions hinders obtaining meaningful data in *operando* measurements. One further drawback of the SPACI-FB reactor system, as of other contemporary reactor setups, is the number of individual parts, which need to be assembled and integrated at the beamline.

In conclusion, utilizing the profile measurement technique combined with synchrotron X-ray techniques is a promising approach to significantly expand the characterization portfolio. The drawbacks of current setups stimulated the development of a flexible spatial profile reactor setup for synchrotron measurements using a more sophisticated heating concept, which was addressed in this work by developing a synchrotron CPR in collaboration with Reacnostics GmbH and experts from different fields.

2.3 Introduction to Synchrotron Light Sources

Synchrotron light sources are research facilities that represent a particular type of cyclic particle accelerator used to produce intense X-rays, also known as synchrotron light. The special characteristics of synchrotron light combined with the dedicated research infrastructure found at synchrotron facilities provide a unique tool for studying the structure of materials. To give the reader a clearer picture of synchrotron radiation, the first Subsection 2.3.1 begins with a brief outline of the properties and generation of synchrotron radiation.

At present, there exist more than 50 synchrotron facilities around the world. The capabilities and constraints of the numerous synchrotron facilities differ and depend on various technical factors. Since all synchrotron studies presented in this work were carried out at the PETRA III synchrotron radiation source at DESY (Hamburg, Germany), the following Subsection 2.3.2 describes the design and functional principle of this synchrotron light source. A comprehensive overview of the versatile subjects related to synchrotron light sources is beyond the scope of this work. The reader is referred to [88] for obtaining information on different synchrotron facilities worldwide or to the respective synchrotron website. Further, specialized Journals such as the Journal of Synchrotron Radiation show the diverse research landscape employing synchrotron radiation, and books as [89,90] provide a detailed description of underlying physics.

2.3.1 Synchrotron Radiation

Synchrotron-produced X-rays are a form of electromagnetic radiation with high-energies and short-wavelengths, ranging from about 0.001 to 10 nm, corresponding to energies of 124 eV to 1240 keV [91]. The range relevant for catalysis research using synchrotron X-ray techniques covers approximately a few keV up to 100 keV. The wide and tunable energy range combined with the unique properties of synchrotron radiation has established a broad field of various spectroscopic, scattering, and imaging techniques applied in catalysis research [92–94], enabling to study the structure at atomic scale. Key interactions for this are X-ray absorption, as X-rays provide sufficient energy to ionize atoms, as well as X-ray scattering since X-ray wavelengths are on the order of interatomic distances.

The underlying physical principle that enables the production of synchrotron light is that moving electrons emit energy as they change direction [89, 90]. In synchrotron machines, electrons are accelerated near to the speed of light and are circulated in a synchrotron ring. As the extremely fast-moving electrons change direction, the emitted energy is at the desired short-wavelength range. X-ray tubes in laboratory machines or hospitals are able to produce short-wavelength radiation as well. However, synchrotron radiation facilities generate X-ray beams that are approximately 10 trillion times brighter compared to laboratory machines [95]. The brightness, as well as the flux, flux density, and brilliance, are interrelated quantities that are typically used for quantifying the quality of an X-ray beam [89, 96]. The photon flux describes the number of X-ray photons emitted per second, while the flux density is synonymous with concentration or intensity, described by the flux per unit area. The brightness of a beam describes the photon flux per unit solid angle, which defines the cone in space into which the beam spreads out. Hence, the brightness considers the angular divergence of the beam, whereas the last quantity, the brilliance or spectral brightness, additionally takes into account the beam size, defined as brightness per cross-sectional area of the beam.

$$[\text{Brilliance}] = \frac{\text{photons}}{s \cdot mrad^2 \cdot mm^2 \; 0.1 \; \%} \tag{2.13}$$

All quantities – flux, flux density, brightness, brilliance – are defined to as the photons that fall within 0.1 % of the central photon wavelength. This wavelength or frequency range is described by the Bandwidth (BW) of 0.1 %, and thus considering monochromaticity of the beam. The brilliance, more specifically the product of angular divergence and beam size, cannot be changed by optical means [96]. Therefore, the optimization of the brilliance represents the driving force behind developing new synchrotron light sources, aiming to provide a maximum number of X-ray photons of a specific wavelength concentrated on a sample per unit time. New and major technical achievements have led to different synchrotron generations. There is currently the fourth generation synchrotron light source. The first one of this generation is the European Synchrotron Radiation Facility (ESRF) in Grenoble, France, having a brilliance value above $10^{21}\ \frac{\text{photons}}{s \cdot mrad^2 \cdot mm^2\ 0.1\ \%}$, approximately 100 times brighter than its predecessor [95]. At present, a similar upgrade is planned for the synchrotron radiation source PETRA III to IV at DESY [97].

2.3.2 PETRA III - Deutsches Elektronen-Synchrotron DESY

Synchrotron work was carried out at the PETRA III synchrotron radiation source at DESY (Hamburg, Germany), a shared research center chiefly supported by the Federal Government (90 %) and the city Hamburg (10 %) [98]. In the following, the working principle of a synchrotron radiation facility is explained based on this example.

PETRA III is the so-called storage ring, which is a closed tube maintained under vacuum. The electrons are circulated for hours around the PETRA III ring that has a considerable length of 2304 m [99]. This length makes PETRA III the biggest storage ring in the world, and at the same time, one of the brightest storage-ring-based X-ray light sources, providing a brilliance greater than $10^{21}\ \frac{\text{photons}}{s \cdot mrad^2 \cdot mm^2\ 0.1\ \%}$ [99]. Figure 2.6 shows an aerial view of PETRA III, denoted in orange, as well as the three experimental halls, denoted in blue. The experimental halls are ‘Ada Yonath’ (left), ‘Max von Laue’ (curved building in the middle), and ‘Paul P. Ewald’ (right) [99].

Before electrons are injected and stored at a particle energy of 6 GeV in the PETRA III ring, they undergo an injector chain consisting of several sections [101]. A schematic overview is shown in Figure 2.7, left. First, electrons are generated in an electron gun and directed into a pre-buncher, which packs the electrons

Figure 2.6: Aerial view of the PETRA III storage ring and the three experimental halls at Deutsches Elektronen Synchrotron DESY, Hamburg, Germany. Picture is adopted from [100](modified). Copyright: DESY, Britta Liebaug Illustration, Reimo Schaaf Picture.

in “bunches”. The electron bunches are pre-accelerated to 450 MeV in a linear accelerator, called Linac II. Subsequently, the electron bunches are stored in the small storage ring PIA with a length of 29 m. In the final step, before the electrons reach PETRA III, they are transmitted to a circular accelerator, known as the booster ring DESY II. The booster ring has a length of 293 m and accelerates the electrons to 6 GeV.

As the electrons move in the PETRA III ring, synchrotron radiation is produced whenever the electron bunches are transversely accelerated. In second-generation synchrotrons, this was achieved by powerful bending magnets, while third-generation sources such as PETRA III utilize special insertion magnet devices as undulators. Synchrotron radiation used in this work is provided by undulators [104] that are the most powerful generators of synchrotron radiation at storage rings. Undulators are installed in the straight sections of the ring, which are composed of small magnets of opposite polarity, forcing the electrons to follow an undulating wave path. In this way, emitted X-rays from each bend overlap and interfere, creating a highly brilliant beam by constructive interference at tuned energies [101].

Radiation branches off the storage ring and enters experimental facilities, known as beamlines. 26 beamlines (including inline branches) are distributed over the

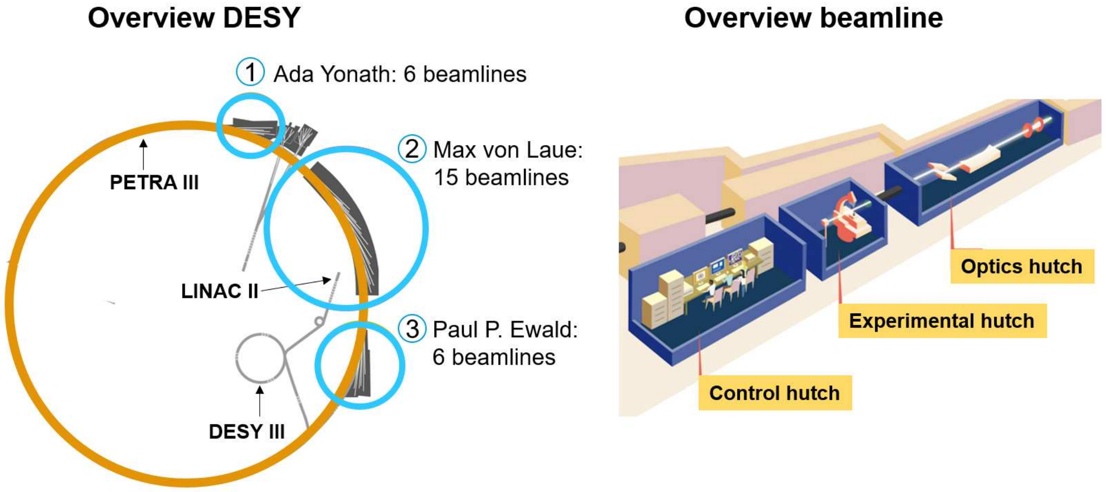

Figure 2.7: Overview of the DESY facility from electron generation, electron storage and produced radiation from the storage ring entering specialized beamlines (left) as well as of the main hutches in a beamline (right). Illustration, left adopted from [102] (modified). Copyright: DESY, Britta Liebaug. Illustration, right adopted from [103] (modified).

three experimental halls [105]. A beamline consists of the optics, experimental and control hutches, aligned in a row (Fig. 2.7, right). First, the raw X-ray beam provided by the undulators is refined in the optics hutch that comprises several devices as monochromators, selecting a particular photon energy, and focusing optics (i.eg. lenses, mirrors). Second, the experimental hutch provides space and infrastructure to put the sample in the X-ray beam, including custom-designed chambers and reactors for ex-situ, in-situ and *operando* experiments, as well as different types of detectors. Third, from the control hutch sample positioning by motors, beam alignment, and data acquisition are controlled.

External scientists can apply for beamtime to carry out experiments at allocated beamlines at PETRA III twice a year (regular procedure). The application is in form of a proposal that gives a detailed description of the experiment and its scientific value for the community and society, reviewed by an external peer-review panel. The choice of a beamline is determined by the experiment and the scientific question to be answered since beamlines are highly specialized for certain techniques. The next section describes two prominent synchrotron techniques of relevance for this work.

2.4 Synchrotron Catalyst Characterization Techniques

There are various spectroscopic, scattering, and imaging X-ray techniques commonly established to analyze structural properties of the catalyst. Each technique captures a certain information of the catalyst and the choice of the respective technique highly depends on the scientific questions to be answered as well as on the requirements of the given application. A comprehensive overview of developed synchrotron techniques is beyond the scope of this work. Hence, the reader is referred to [16, 89, 92–94, 106, 107] for more detailed information on the wide field of synchrotron techniques and related research. Prominent techniques are XAS [108–111] and XRD [91, 112, 113]. Both techniques were used in this work and are presented in the following subsections.

2.4.1 Fundamentals of X-Ray Absorption

XAS presents a versatile and practical technique for structural analysis of materials, applied in a wide range of scientific fields. From XAS spectra, information on the chemical state, coordination chemistry, and on the local structure from materials that possess long or no long-range order are obtainable. As the name suggests, in XAS experiments X-ray photons are used to bombard a sample material in order to probe the amount of absorption as function of energy. The X-ray photons must be of a defined energy, which is changed to scan over a range of approximately 1000 eV with sufficient resolution in energy ($\approx$ 1 eV) [109]. This requires an energy-tunable and intense X-ray source, making XAS a technique which is preferable and often essential to perform at synchrotron radiation light sources (see Section 2.3).

At specific energies characteristic for the elements in the material, an X-ray photon is absorbed, known as photoelectric absorption [109, 110]. A simplified schematic illustration of the photoelectric absorption event, exemplified for a Mo atom with three shells (K, L, M), is shown in Figure 2.8. An incoming X-ray photon is absorbed (i.e., destroyed) when its energy is equal or greater than the binding energy of a core electron, causing the excitation or ejection of the core electron as photoelectron [109, 110]. Core electron binding energies of Mo atoms are listed in Table 2.1. For example, in order to liberate an electron from the K-shell the incident X-ray photon must possess a minimum energy of 20 keV [114]. The energy difference between the X-ray photon and core electron is given to the ejected photoelectron (E – E_{kin}) [108, 109].

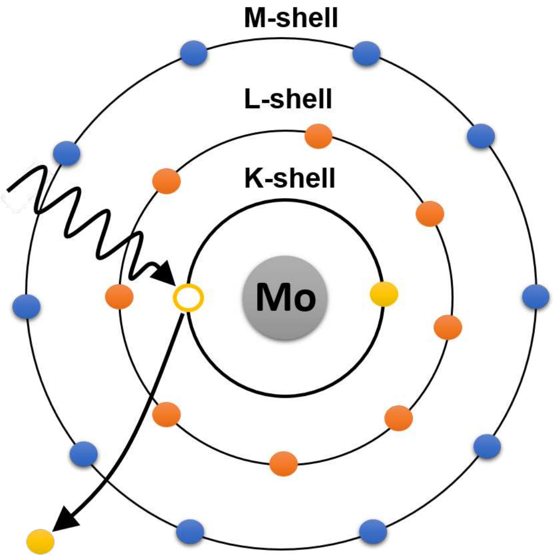

Figure 2.8: A simplified schematic representation of the photoelectric absorption event occurring at the K-shell of a Mo atom.

Table 2.1: Edge energies of shells in Mo atoms [114].

Shell	Edge energy
K	19.9995
L_1	2.8655
L_2	2.6251
L_3	2.5202

After the X-ray absorption event, the atom is in an excited state with a core hole on the particular orbital present. The excited state decays typically within femtoseconds because the core hole is refilled by X-ray fluorescence or the Auger-effect [109, 110]. X-ray fluorescence occurs when a core electron from a higher energy shell drops into the core hole on the deeper energy shell, producing an

X-ray with a well-defined energy. For example, if the core hole on the Mo K-shell is refilled by an electron from the L_1 shell, the fluorescence energy of a K_α line is emitted. The Auger-effect takes place when an electron drops from a higher electron shell and a second electron is ejected. In XAS experiments, absorption can be quantified by all three effects [109, 110], while the focus in the following section is on the first absorption event, as it was used in this work.

The physical quantity measured in XAS is the absorption coefficient μ(E), which expresses how many X-ray photons are absorbed by a sample material as a function of X-ray energy. By measuring the incident X-ray energy (upstream of a sample) and the exiting X-ray intensity (downstream of a sample), μ(E) can be derived according to Beer's law [110]:

$$I = I_0 \exp^{-\mu(E)x} \tag{2.14}$$

where I_0 is the incident X-ray intensity, x is the sample thickness, and I is the transmitted intensity through the sample. This measurement configuration is called transmission geometry, where commonly ion chambers are utilized as detectors (Figure 2.9).

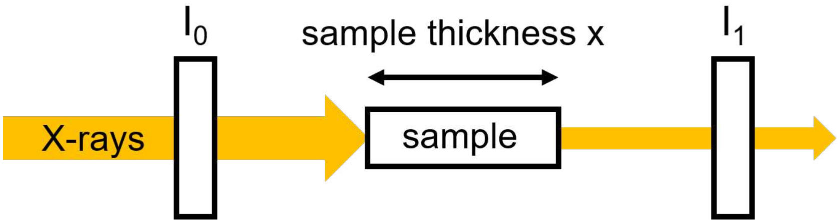

Figure 2.9: Schematic of XAS measurements carried out transmission geometry.

μ(E) has strong dependencies on the sample density ρ, the atomic number Z, atomic mass A, and the X-ray energy E [109].

$$\mu \approx \frac{\rho Z^4}{AE^3} \tag{2.15}$$

The number of absorbing atoms present in a given sample thickness (i.e., density) is directly proportional to μ(E). In order to compare μ(E) between different elements, the normalized mass absorption coefficient $\mu_m(E)$ is used. $\mu_m(E)$ is obtained by dividing μ(E) with the density [110].

$$\mu_m(E) = \frac{\mu(E)}{\rho} \tag{2.16}$$

The mass absorption coefficient $\mu_m(E)$ is well tabulated for chemical elements [114], illustrated in Figure 2.10 for Pt, Mo, and Ni as function of energy.

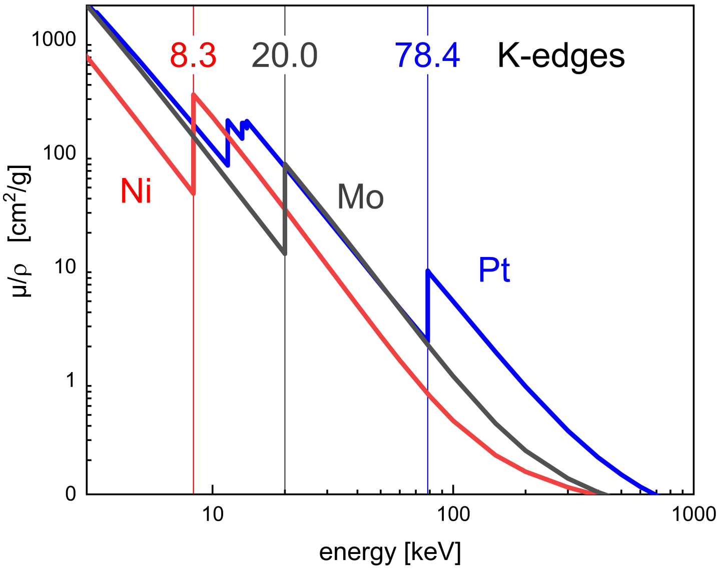

Figure 2.10: Mass absorption coefficients for Pt, Mo, and Ni as function of energy, emphasizing corresponding edge jumps [114].

One basic property of X-rays interacting with matter is illustrated by the smoothly decreasing trend of μ_m with increasing energy ($1 \propto \mathrm{E}^{-3}$), i.e., X-rays become more penetrating through materials with higher energies [109]. Due to the strong dependence of μ on $\propto \mathrm{Z}^4$ (Pt = 78, Mo = 42, Ni = 28), most elements have very different μ values, enabling to distinguish many elements. A sudden rise in μ_m occurs at energies characteristic to the different elements. For example, Pt at 78.4 keV, Mo at 20.0 keV, and Ni at 8.3 keV, corresponding to the onset of photoelectric absorption at the respective K-edges [114]. In case of Pt, the three L-edges are found additionally within the illustrated energy range (Fig. 2.10). The difference between the edge energies is large and varies strongly with the atomic number $\propto Z^2$ [109]. Most elements can be measured with X-ray energies between 5 – 35 keV, making use of K-, L-, and M-shells, depending on the atom type.

Figure 2.11 presents an experimental XAS spectrum of MoO_3 (prepared as pellet) measured in transmission geometry around the Mo K-edge (20,000 eV). The absorption coefficient is shown as a function of the incident X-ray photon energy over a scan range of 19,000 – 21,000 eV. The spectrum illustrates several common features to most XAS spectra [110]. The features are described for MoO_3 below.

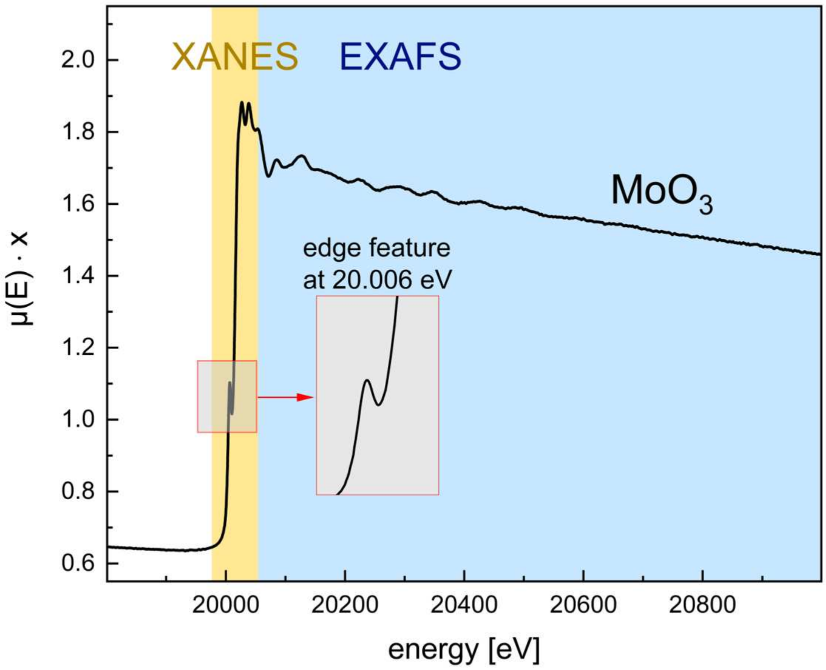

Figure 2.11: A XAS spectrum of MoO_3 measured around the Mo K-edge energy.

1. The sudden and sharp rise in the absorption coefficient observed at 20,000 eV is known as the absorption edge, i.e., Mo K-edge.

2. A small peak on the rising edge at 20,006 eV, denoted as edge feature.

3. Oscillations in the $\mu(E)$ above the absorption edge ($\approx$ 50 – 1000 eV from the edge).

4. The $\mu(E)$ decreases smoothly as energy increases, (see Eq. 2.15), referred to as the background.

The term XAS comprises several different techniques, including X-ray Absorption Near Edge Spectroscopy (XANES) and Extended X-ray Absorption Fine Structure Spectroscopy (EXAFS). The techniques refer to two different regions in the spectrum, denoted in yellow (XANES) and blue (EXAFS) in Figure 2.11 [109, 110]. The transition between the two regions is smooth. While XANES corresponds to the region where low-energy photoelectrons are produced, EXAFS refers to the region with high-energy photoelectrons. Both techniques have the same physical origin, but contain different information. XANES describes the features near or on the edge (19,980 – 20,050 eV), allowing to determine the oxidation state and coordination (e.g., tetrahedral coordination) of the absorbing atom, while EXAFS describes the oscillations above the edge (20,050 – 21,000 eV), enabling to deduce type, number, and distance of atoms surrounding the absorbing atom. XANES cannot be described mathematically in a simple equation, as it is possible for EXAFS [109,110]. In turn, XANES analysis is more straightforward compared to EXAFS, allowing to fingerprint phases and oxidation states by comparing the spectra of a sample to spectra from known reference compounds. For instance, the shape and position of the absorption edge, as well as the heights and positions of pre-edge peaks, are evaluated. Related to EXAFS, the energy-dependent oscillations in the μ(E) value represent a characteristic interference pattern, obtained by describing the ejected photoelectron from the absorbing atom as a wave. The ejected photoelectron waves are scattered by neighboring atoms and the scattered waves return to the original, absorbing atoms. As a result, the photoelectron can interfere constructively and destructively with itself. The probability of absorption (measured quantity μ(E)) oscillates due to this constructive and destructive interference and is enhanced with constructive [109, 110]. The obtained interference pattern results from the sum of contributions from backscattered photoelectron waves, which individually correspond to different types, numbers, and bonding configurations of neighboring atoms. Therefore, the measured frequencies and amplitudes yield a characteristic interference pattern for the structure of a material, mathematically described by the function χ(k), also known as the EXAFS equation [110].

$$\chi\left(k\right)=S_0^2\sum_i N_i\frac{f_i\left(k\right)}{kD_i^2}e^{-\frac{2D_i}{\lambda(k)}}e^{-2k^2\sigma_i^2}\sin\left(2kD_i+\delta_i\left(k\right)\right) \tag{2.17}$$

where k is the wavenumber, S_0^2 is the amplitude reduction factor, $\lambda(k)$ is the mean free path, σ_i^2 the mean square radial displacement (thermal or static disorder in the neighbor atom). Important structural parameters such as distance, number, and type of neighboring atoms are deduced from D_i, the distance between absorbing and neighboring atom, that influences the spacing (frequency) of the oscillations. Further, from N_i, the number of scattering atoms nearby, as well as from the two scattering parameters $f(k)$ and $\delta(k)$, which depend on Z and thereby on the type of the neighboring atom. N_i and the scattering factors have impact on the amplitude of the oscillation. For a more detailed derivation of the EXAFS equation and meaning of the parameters the reader is referred to [110].

2.4.2 Fundamentals of X-Ray Diffraction

In heterogeneous catalysis, XRD is a prominent characterization method to determine the average bulk structure on solid catalysts in powder form that possess a long-range order, i.e., crystalline substances above a minimum crystallite size. XRD analysis standardly includes the identification and quantification of crystalline phases in a mixture. XRD does not belong to the spectroscopic methodologies since diffraction is a geometric phenomenon, having signals measured as a function of angle compared to wavelength (or related parameters) as in spectroscopy. XRD results from a fundamental interaction of X-rays with a crystalline material, known as elastic scattering. As an incoming X-ray (electromagnetic wave with a high frequency) interacts with an electron (charged particle) of an atom shell, the electron starts oscillating with the same frequency. Through this oscillation the electron itself becomes a source of electromagnetic radiation, emitting a spherical electromagnetic wave with the same frequency as the incoming wave [112]. In short, incident X-rays are scattered elastically by electrons of atoms. Crystals have an ordered arrangement of atoms in space, each having (several) electrons around the nucleus, functioning as a scatterer respectively. The individual scattered waves interfere constructively and destructively with each other, producing a characteristic interference pattern for a certain material. It is this interference pattern in which the information of atomic spacing and positions is encoded. At constructive interference, intense signals of the outgoing radiation in specific directions occur, described by the fundamental law of diffraction, namely the Braggs' law [91, 112].

$$n \cdot \lambda = 2 \cdot d \cdot \sin(\theta) \tag{2.18}$$

where n is a positive integer number (1, 2, 3,...n), d is the spacing between crystal lattice planes, θ is the Bragg angle, and λ is the wavelength of the beam. Figure 2.12 shows the derivation of Bragg's law geometrically with a simplified crystal structure in 2D and two incoming X-ray waves as green lines.

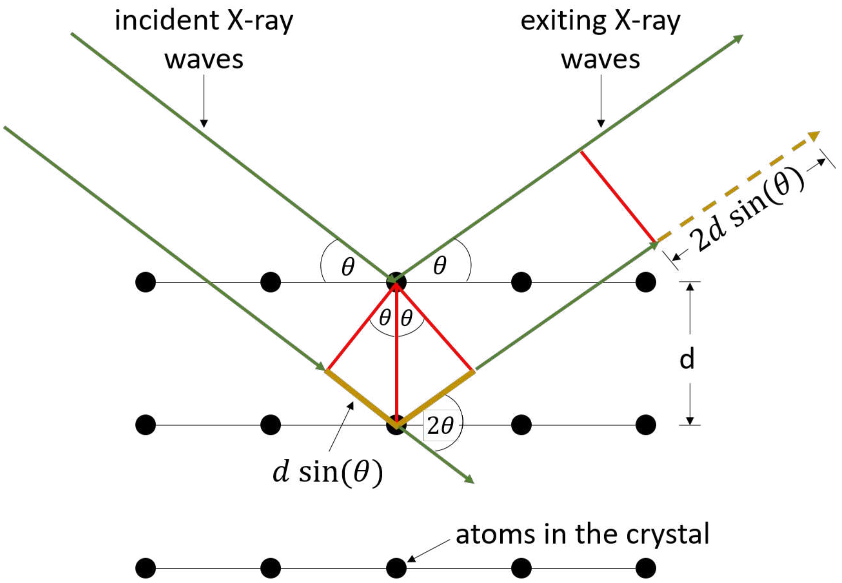

Figure 2.12: Geometrical derivation of Bragg's law adopted from [112] (modified).

Here, three lattice planes parallel to one another, having a crystal plane distance d and five atoms each, are illustrated. The incoming X-ray waves, having the same wavelength and being in-phase, are diffracted by two different lattice planes. The angles are equal between the incident beam and the lattice plane as well as between the diffracted beam and the lattice plane. Bragg's law is fulfilled, i.e., constructive interference occurs, when the path-length difference between the upper and lower wave ($2 \cdot d \cdot \sin(\theta)$) equals an integer multiple of the incident X-rays ($n \cdot \lambda$). Since distances between atoms are in the order of magnitude of a few angströms

(1 Å^{-1} = 10^{-10} m), X-rays are required to determine crystal lattice structures via diffraction. A crystal has a periodic arrangement of atoms in space and different sets of parallel lattice planes, each causing constructive interference at a certain angle. Noteworthy, a set of lattice planes is clearly defined in space by the so called Miller indices [91, 112].

A typical powder XRD pattern of a solid catalyst sample is shown in Figure 2.13.

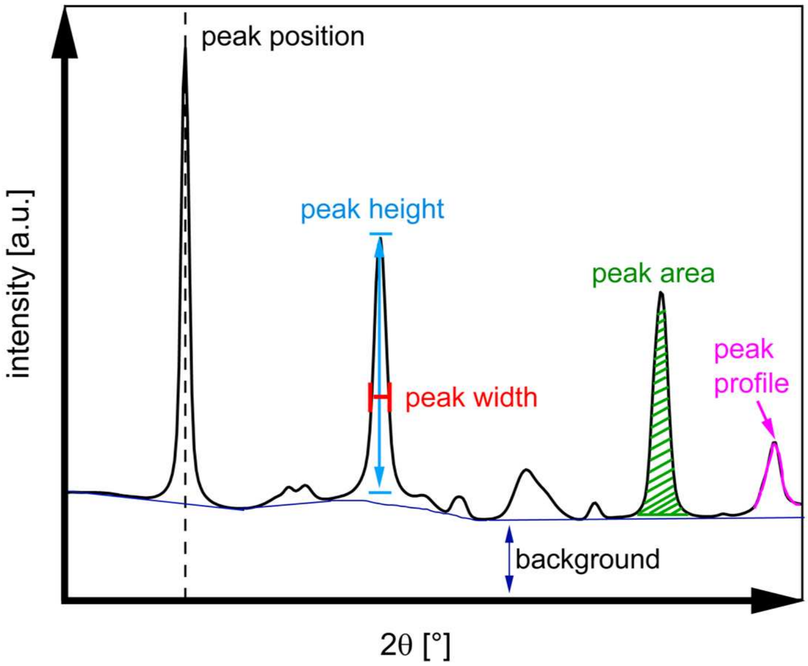

Figure 2.13: A typical XRD pattern of a solid catalyst sample showing several Bragg peaks and ways of peak analysis.

The pattern shows the intensity of various diffraction signals referred to as Bragg peaks (also called diffraction peaks, lines, reflections) as a function of the diffraction angle 2θ. Information can be deduced from the peak position, intensity, and shape (e.g., peak width and profile) [91, 112], marked in color in Figure 2.13. From the position of each reflection the distance between parallel planes of atoms in a crystal, referred to as the d-spacing according to Bragg's law, as well as lattice parameters can be obtained. Shorter plane distances occur at larger angles and vice versa. Peak intensities provide information on crystallinity as well as number and type of atoms present on a given crystal plane set. A high crystallinity results in

narrow, intense peaks due to a high number of parallel, diffracting crystal planes that enhance wave amplitudes at constructive interference. In addition to this, the scattering power of a certain crystal plane set correlates with the number of electrons, and thus with the number of atoms present on a crystal plane and corresponding atomic numbers. Furthermore, from intensities, the amount of a certain phase in a phase mixture can be revealed. Intensities are evaluated in two ways, either using the peak height (maximum intensity) or, more precisely, the peak area (integral intensity). Peak shapes, e.g., Gaussian, Lorentzian, Voigt, as well as peak widths (Full Width at Half Maximum (FWHM)) tell us something about crystallite sizes and defects, which are present in real crystal structures [91, 112]. When the crystallite size becomes too low, materials are XRD amorphous and contribute to XRD patterns through diffuse scattering, generating a background signal without identifiable peaks. Phase identification is conducted by comparing measured XRD patterns with references from databases, while phase quantification is determined by comparing relative peak intensities or by fitting a calculated XRD pattern to an experimental, known as Rietveld refinement.
In order to obtain an XRD pattern as shown in Figure 2.13, different experimental geometries are feasible. Commonly applied experimental geometries are Bragg-Brentano in reflection mode or Debye-Scherrer in transmission mode [91, 112]. The latter is further described due to its relevance in this work. In transmission mode, the X-ray beam passes through a powder sample with a defined and fixed energy. Cone-shaped diffraction signals, known as Debye-Scherrer cones, are obtained from the diffraction of the X-ray beam by the randomly orientated crystals in the powder sample. In Figure 2.14 (left) two Debye-Sherrer cones (d_1, d_2), formed in transmission XRD, are illustrated. The diffracted signal is collected on a large area detector, located downstream of the sample. The signals are observed in the forms of several Debye-rings on the detector (Figure 2.14, right). The number and position of the Debye-rings are characteristic to the material, corresponding to the number and position of Bragg reflections shown in Figure 2.13.

For evaluating observed Debye-rings on the detector, the energy of incoming X-rays and experiment geometry must be precisely defined, including positions in space of the sample, beam and detector. For example, Debye-ring positions on the detector depend on the distance between sample and detector, and ring shapes on

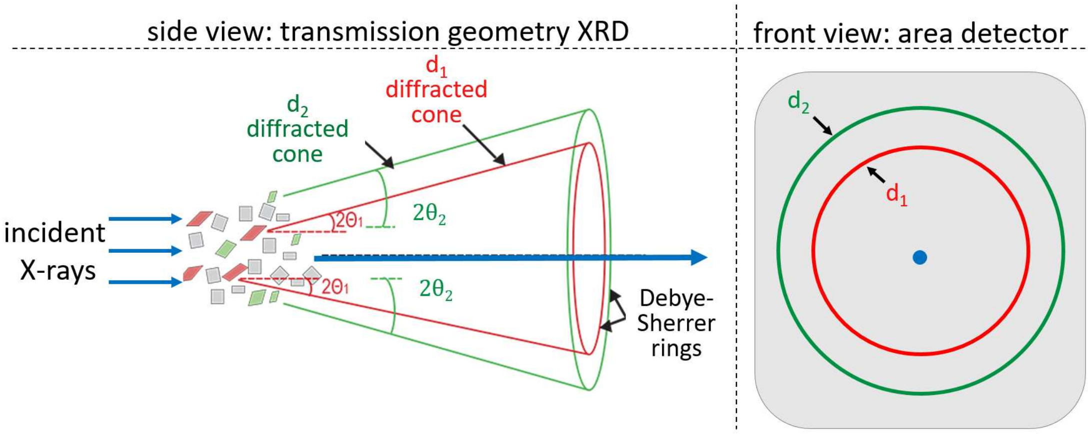

Figure 2.14: Debye-Scherrer cones formed during transmission XRD (left) and corresponding Debye-Scherrer rings measured on an area detector (right). Figure, left adopted from [115] (modified).

the angular position of the beam to the detector surface, aiming to be orthogonal to obtain circle-shaped signals.

For the interpretation of formed Debye-rings two concepts are in combination beneficially to use: the reciprocal lattice and the Ewald sphere [91, 112]. As the name suggests, the reciprocal lattice is inversely proportional to the signal in real space, providing an alternative view on the crystal lattice. The reciprocal lattice consists of a number of Reciprocal Lattice Points (RLP) on a regular grid. The advantage of this concept is the relation to the crystallographic planes and Miller indices. Each RLP has a certain Miller index, which corresponds to a family of crystallographic planes, and thus each representing a diffraction possibility. The second concept is the Ewald's sphere, typically being a sphere with a radius of $\frac{1}{\lambda}$, where λ is the set wavelength of the X-rays in the experiments. The combination of both concepts is illustrated in 2D in Figure 2.15.

As both concepts are combined, it allows to deduce the occurrence of diffraction during a given experiment according to Bragg's law. The criterion of Bragg's law is fulfilled whenever a RLP (other than the origin O) intersects with the circumference (surface of the sphere in 3D) of the Ewald sphere [91,112]. By rotating the incident beam with respect to the crystal and thereby the Ewald's sphere around the origin, all RLP will eventually fulfill the diffraction condition. Powder sam-

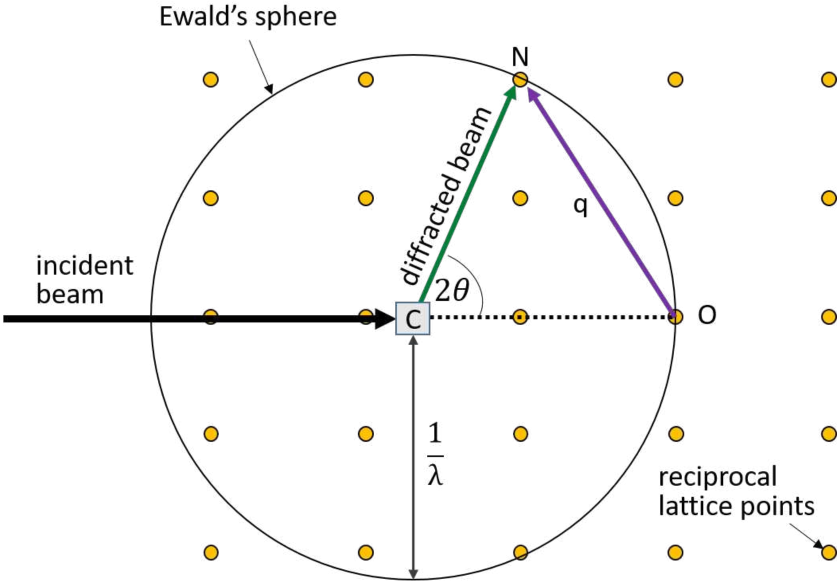

Figure 2.15: The Ewald sphere in reciprocal space adoopted from [112] (modified).

ples consist of numerous crystallites of identical reciprocal lattices but randomly oriented in space and with respect to each other. Hence, the signal appears as a ring instead of a single point.

Since the size of the Ewald's sphere depends on the wavelength applied in the measurement, accessible Bragg peaks vary with the wavelength. Likewise, the same Bragg reflection varies in its angular position in a XRD pattern (Fig. 2.13). Since energies can be chosen flexible at synhcrotron radiation sources, compared to lab-based X-ray instruments, powder diffraction experiments carried out at synchrotron light sources often plot XRD data as a function of the length of the reciprocal lattice vector q (Å^{-1}), providing an independent scale [112]. In other words, Bragg reflections occur at the same q position, no matter at which wavelength the measurement was conducted. The angular range can be converted into q and vice versa, according to Eq. 2.19.

$$q = \frac{4\pi}{\lambda} \cdot \sin(\theta) \tag{2.19}$$

2.5 Gas Analysis

The qualitative or quantitative gas analysis of sampling streams is another important task in catalysis research. Various analytical techniques are implemented to analyze gas samples. The choice of the respective technique highly depends on the research question and the requirements of the chemical system under study. In this section, two of the most commonly used analytical techniques, GC and mass spectrometry (MS), are briefly described due to their relevance in this work.

2.5.1 Gas Chromatography

GC is a common analytical technique to determine the composition of a gas mixture by separating the compounds based on a different partitioning behavior between mobile and stationary phases. Among the various types of GC, in this work, the term GC is referred to as gas-solid chromatography, where the mobile phase is a gas and the stationary phase is a solid. The following subsection briefly summarizes basic aspects related to this type of GC based on comprehensive literature [116–118]. A schematic representation of the basic instrumentation of a GC is shown in Figure 2.16, consisting of a carrier gas, a sample injection port, columns, ovens, heaters, detectors, and a data acquisition system.

The mobile phase, also known as the carrier gas, is an inert gas such as helium or argon that serves the purpose of carrying the analytes through the columns. In order to mix and carry the sample with the mobile phase, the sample must be in a gaseous state. The gas sample is injected into columns, where the actual separation process takes place due to different interactions of each component with a stationary phase.

Capillary columns have been established as the predominant column type, consisting of a long open tube ($\approx 15 - 100$ m, ID $0.1 - 0.53$ mm) made of fused silica and coated with polyimide [119]. The stationary phase is immobilized on the inner capillary tubing walls or supported onto a solid inert packing. The latter column type, so-called Porous Layer Open Tubular (PLOT) capillary columns, is of relevance for this work. The PLOT column has a porous layer of a solid material (e.g., alumina, molecular sieves, Porapak) attached to the capillary inner wall that

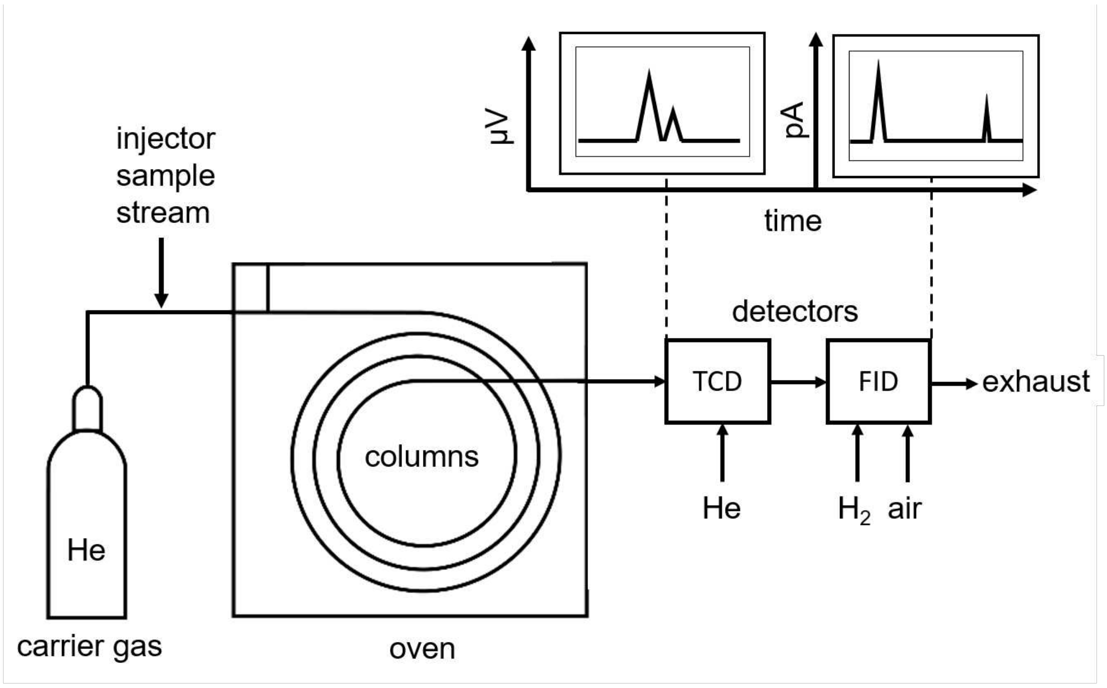

Figure 2.16: Schematic overview of the main components of a GC system.

serves as the adsorbent. PLOT columns are suited for separating light hydrocarbons, CO_2 and H_2O based on differences in polarity as well as permanent gases based on size (molecular sieves) [119]. The retention time of each component on the column is determined by the strength of interaction and thus, by the structure and functional groups of each component. By tuning physical column parameters (internal diameter, length, stationary phase) and conditions (temperature and flow velocity), the separation is optimized for a given process.

Detectors are used to measure the separated components eluted from the column. The time at which the detector signal is produced corresponds to the retention time (qualitative analysis), whereas the signal amount (peak area, intensity) corresponds to the concentration of the compound. Widely established detector types are the Thermal Conductivity Detector (TCD) and the Flammable Ionization Detector (FID). The TCD measures the gas sample non-specifically and non-destructively based on the difference in thermal conductivities between the carrier gas flow (reference channel) and the eluent flow (sample channel), i.e., carrier gas mixed with the sample components. The channels are temperature-controlled cells with a heated filament placed inside. A temperature difference between the filament and cell is adjusted in order to enable a heat flow from the filament to the cell wall. Applied carrier gases have higher thermal conductivities than most analytes. As a result, the heat flow rate is decreased in the sample channel causing a higher filament temperature and a different electrical resistance compared to the reference channel. The difference in resistance of the filaments is often measured by a Wheatstone bridge circuit, producing a measurable voltage. The voltage signal is proportional to the resistance difference in the channels and thus, to the gas concentration. The chromatographic signal produced is in μV as a function of time. The thermal conductivities of most organic and inorganic compounds are different from the carrier gases (He, H_2, Ar), making the TCD a universal detector for the detection of many different components.

One drawback of TCDs is their lower sensitivity up to $\approx$ 1 ppm compared to other detectors as the FID. FIDs provide large linear dynamic detection ranges up to $\approx$ 1 ppb [120], but in turn, destroy the gas sample during analysis and restrict the measurement to organic (C-H bonds) components. The operating principle of FIDs is based on the generation and detection of cations. A hydrogen-air flame is used to ionize the organic compounds in the gas sample stream. The formed positive cations are attracted and collected at electrodes, called collector plates, and produce a measurable current. This signal is amplified in an electrometer and proportional to the number of molecules ionized, i.e., species concentration in the gas. The obtained chromatographic signal is in pA as a function of time.

2.5.2 Mass Spectrometry

Another common analytical device to analyze the composition of gas samples are MSs. In comparison to GCs, MSs have the advantage of significantly faster data acquisition and higher flexibility. In MSs gas samples are separated and analyzed according to the mass-to-charge ratio m/z. In general, the processes inside MSs can be divided into four steps: In the first step, the sample is transferred into a high vacuum chamber. Subsequently, the sample is ionized and then the ions are separated according to their mass-to-charge ratio. Finally, the ions are detected by an ion detector, recording the measured signal. In this work, a Hiden Analytical

HPR 20 was used. Thus, the working principles of the basic components of this MS are explained in this subsection. For a more detailed review of the various types of MSs the reader is referred to [121–123].

In the Hiden Analytical HPR 20 gas is dosed effusively through a heated inlet capillary into a vacuum chamber. The gas sample is subsequently ionized by electron impact ionization using a beam of high-energy electrons at 70 eV. The sample molecules are bombarded with electrons with high kinetic energies, exceeding the energy required for ionization of a species IE_s, resulting with a certain probability P_i in the formation of positively charged ions.

$$\begin{gathered} S + e^- \rightarrow S^+ + 2e^- \\ P_i(E < IE_s) = 0,\ P_\mathrm{i}(E \geq IE_s) = f_\mathrm{i}(E) \end{gathered} \tag{2.20}$$

In addition to the formation of singly positively charged ions, also ions with a charge number z greater than one and fragmentation of molecules occur. For the fragmentation of a molecule not only the ionization energy but also the dissociation energy DI_XY of a bond between two parts of the molecule X-Y needs to be exceeded in order to generate the fragmented molecule with a probability P_d [121].

$$\begin{gathered} XY + e^- \rightarrow X^+ + Y + 2e^- \\ P_\mathrm{d}(E < IE_\mathrm{XY} + DI_\mathrm{XY}) = 0,\ P_\mathrm{d}(E \geq IE_\mathrm{XY} + DI_\mathrm{XY}) = f_\mathrm{d}(E) \end{gathered} \tag{2.21}$$

Signal contributions of single charged, multiple charged, and molecule fragments sum up to a characteristic fingerprint pattern of a species, which allows for identification [121].

The positively charged ions are accelerated by a focus electrode, directing the ion stream toward a mass separation filter. In the case of the Hiden Analytical HPR 20 a quadrupole mass filter is used. Quadrupole mass filters are composed of four hyperbolic or cylindrical rods arranged in an equidistant, quadratic order. A potential composed of a direct current DC voltage U and radio frequency RF voltage V is applied to the rods. Two opposing rods form a pair to which the same potential is applied, while the antipodal potential is applied to the second rod pair as shown in Figure 2.17.

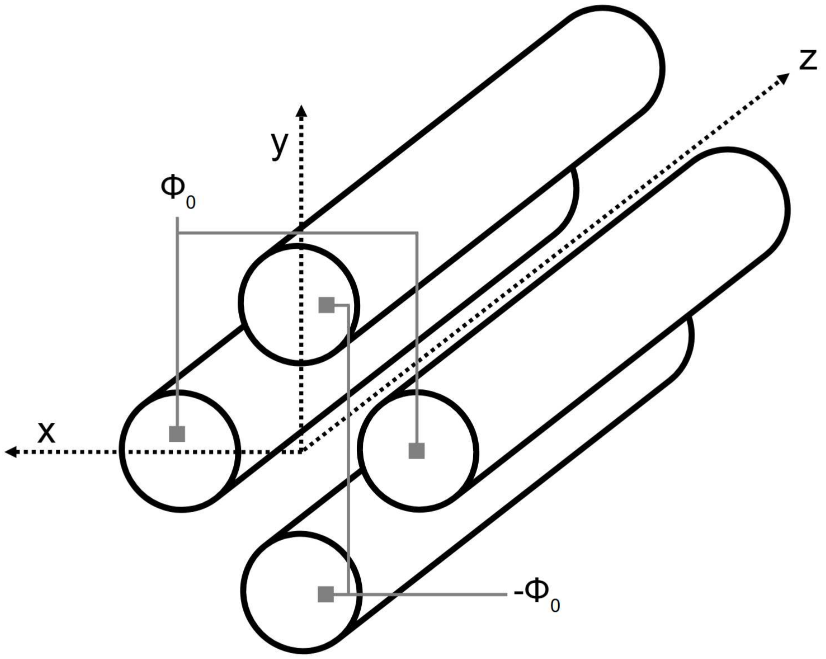

Figure 2.17: Cylindrical rod pairs with antipodal potentials forming a quadrupole mass filter, adopted from [121] (changed).

The rods form an oscillating field, which interacts with the positively charged ions, resulting in a helical flight path of the ions through the quadrupole. Only ions with the correct mass-to-charge ratio m/z for a given applied potential have a stable trajectory and thus, pass the quadrupole [122].

After separation, ions passing the quadrupole are detected in the Hiden Analytical HPR 20 using a Faraday cup. A Faraday cup is composed of a conductive metal, the so called collector electrode, that is connected to an amplifier with a high impedance using a large feedback resistance. The ion beam, which passes the quadrupole and hits the Faraday cup, charges the collector electrode, and results in a voltage drop across the resistance directly proportional to the amount of ions hitting the detector. This voltage is measured to provide the signal of the MS [122]. Due to the direct proportionality of the measured voltage and thus, the resulting signal, Faraday cups provide stable signals, but come at the cost of slower response times compared to other alternatives like secondary electron multipliers.

3 Materials and Methods

In this chapter the material and methods used in this work are introduced. First, catalyst synthesis is described followed by an overview of the experimental setup used for measuring spatial gradients inside fixed-beds. In the next sections details on catalytic activity investigations as well as kinetic modeling are given. The used *operando* profile methodologies (XAS and XRD) are presented individually in two subsequent sections, each including a description on a general methodological approach, setup integration at the respective beamline, gas analysis, experimental details of conducted profile measurements, and data evaluation. Finally, procedures for gas quantification and deriving the target variables (conversion and selectivity) are described.

3.1 Materials

In this section preparation of the catalyst material and gases utilized in this work are given. It should be emphasized that catalyst synthesis was conducted by Christina Laarmann who is working as chemical-technical assistant at TUHH.

3.1.1 Catalyst Synthesis

The MoO_3 supported on γ-Al_2O_3 catalysts were prepared by wet impregnation according to [22]. Different target weight loadings of MoO_3 were produced, complying with the methodological requirements. Alumina spheres were provided by Sasol with a diameter of 1 mm and a specific surface area of 160 m^2/g [124]. The spheres were crushed and sieved to the desired particle size, before impregnation with the molybdenum precursor solution. As a molybdenum precursor Ammonium Heptamolybdate Tetrahydrate (AHM) $(NH_4)_6Mo_7O_{24}$ x 4 H_2O, 99.0 %) from

Merck was used. The required mass of AHM was dissolved in deionized water at a pH of 5.2. The support was impregnated with the precursor solution in 15 – 20 steps. The solvent was removed in a rotary evaporator (40 °C, 100 mbar, 5 h) in between each impregnation step. After impregnation, the catalyst was dried at 120 °C overnight. Catalyst calcination was carried out in the profile reactor at a maximum temperature in the range of 540 – 550 °C for 3 h in synthetic air flow, prior to starting profile measurements.
Details on the utilized MoO_3 weight loadings and particle sizes are given in the experimental details of the respective sections.

3.1.2 Gases

The gases listed in Table 3.1 were either used for the feed mixture, calibration or gas analytics. Gas purity of the same gas type was kept uniform throughout all experiments.

Table 3.1: Information about gases utilized for the reaction or gas analytic.

Species	Purity	Application
C_2H_6	3.5	reactant, calibrant
O_2	5.0	reactant, calibrant
C_2H_4, CH_4, CO, CO_2	3.5	product, calibrant
H_2	5.0	product, calibrant
N_2, Ar, He	5.0	carrier gas (GCs), internal standard, inert

3.2 Overview Experimental Setup

In this work, an experimental setup was developed to obtain spatial gradients inside the catalytic fixed bed during ethane ODH over a $MoO_3/\gamma\text{-}Al_2O_3$ catalyst. An overview of the experimental setup is shown in Figure 3.1. The setup consisted of four main parts: (i) gas dosing system; (ii) spatial profile reactor; (iii) gas analytics, and (iv) characterization technique.

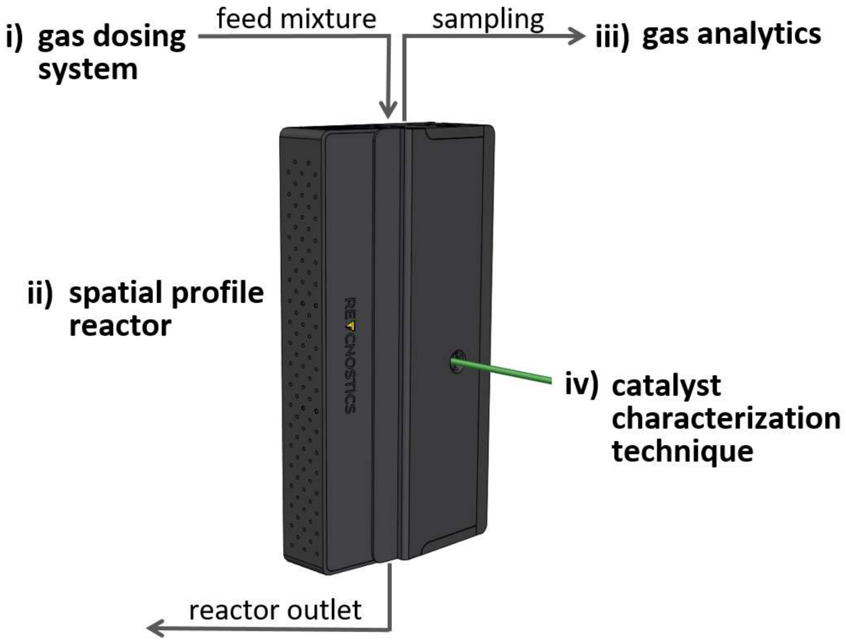

Figure 3.1: Schematic overview of the main parts of the experimental setup used for spatial profile measurements. (i) gas dosing system; (ii) spatial profile reactor; (iii) gas analytics; (iv) catalyst characterization technique.

The gas dosing system comprised several thermal from the EL-Flow Select Series by Bronkhorst High-Tech B.V (Fig. 3.1, i) that allowed to dose precisely the feed mixture into the reaction tube. The feed mixture consisted of two reactants (ethane, oxygen) and one inert component as diluent. Since the inert component was additionally used as internal standard, the gas type varied depending on the requirements of the applied gas analytic. An in-line filter was used to properly mix the feed compounds before entering the reactor tube. In order to prevent bypass flows the reactor and the reactor tube within were vertically mounted and the flow was directed from top to bottom.

Spatial gradients inside the catalyst bed during the reaction were measured by the CPR, developed by REACNOSTICS GmbH (Fig. 3.1, ii). The CPR utilizes the capillary sampling technique to obtain local information within the catalyst bed. The working principle of this technique is thoroughly described in Section 2.2. A schematic overview of the inside of the CPR is presented in Fig. 3.2, illustrating an enlarged view of the heating block which covers the reactor tube and contains a slit-shaped optical access window (Fig. 3.2, A), the reactor tube filled with the catalyst bed and the sampling capillary in the center (Figure 3.2, B), as well as the sampling capillary with the thermocouple located inside (Fig. 3.2, C). The green line represents the incident laser or X-ray signal, aligned with the sampling orifice, the thermocouple tip and the opening of the reactor block.

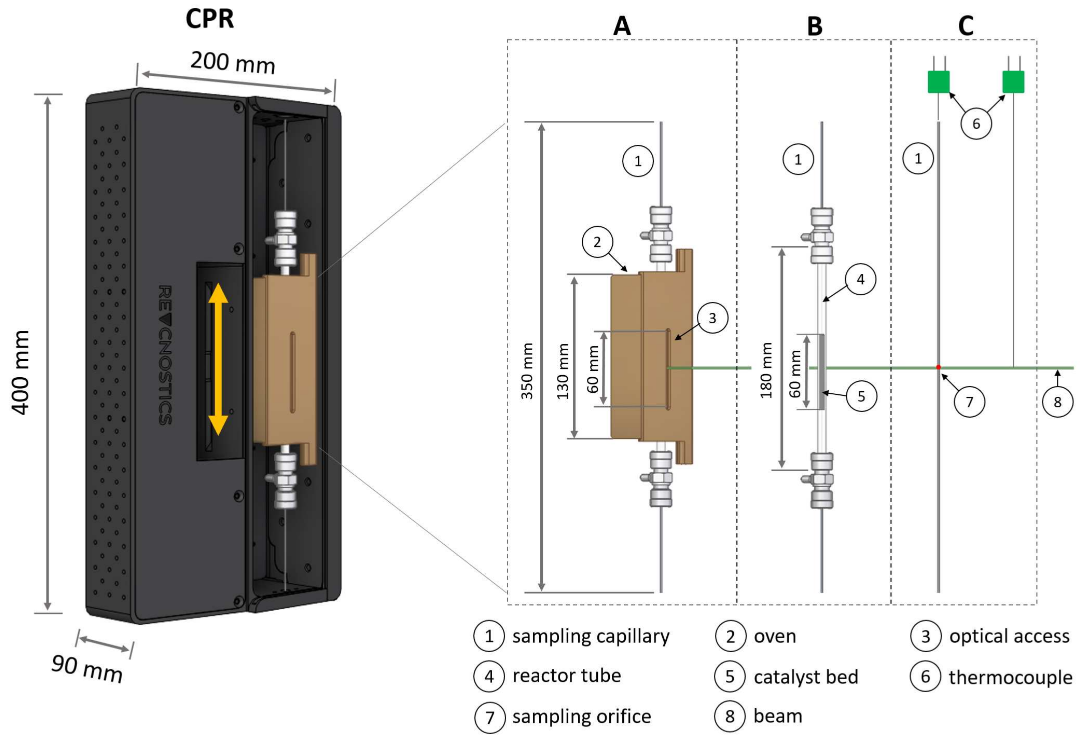

Figure 3.2: Illustration of the Compact Profile Reactor (CPR, left) and components inside (A – C). This figure is included in an article submitted to [125].

The reactor tube had a length of 180 mm and was made of fused silica (Ilmasil PN, QSIL GmbH). While the Outer Diameter (OD) was fixed to 6.0 mm, reactor IDs varying in between 4.0 – 5.6 mm depending on the applied wall thickness. The catalyst bed was packed inside the reactor tube and fixed in position with quartz wool. A stainless steel sampling capillary (OD 700 µm, ID 520 µm) was placed in the center of the catalyst bed. The capillary had four side sampling orifices (50 – 100 µm), illustrated in Figure 3.3. The sampling orifices were laser drilled and arranged with an angular offset of 90° at the same axial position (LaserMicronics GmbH).

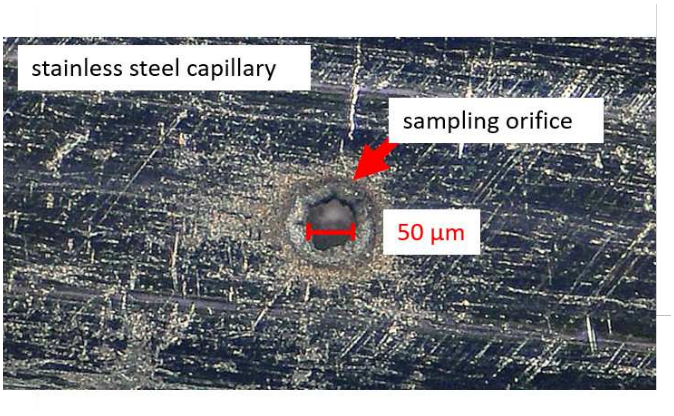

Figure 3.3: Photograph of a sampling orifice laser-drilled in a stainless steel sampling capillary.

The sampling capillary was fixed in space while the reactor tube was movable, allowing to probe a 6.0 cm long catalyst bed. Small gas samples were continuously extracted through the side orifices and analyzed by GC or MS, (Fig. 3.1, iii). In order to reduce the invasiveness of the sampling method on the hydrodynamic conditions inside the reactor, sampling flow rates were controlled to approximately 5 % of the total flow rate by a gas control valve. A micrometering needle valve (Valco Instruments Co. Inc. Vici AG International) was used, enabling precise gas control in the range of 2 – 175 ml/min with a maximum tolerable temperature of 315 °C. The needle valve could be heated and installed either in the sampling or reactor outlet line, depending on the applied gas analytic, reaction conditions (total flow rate, pressure, temperature, catalyst bed length, particle size), and the size of the sampling orifices. Furthermore, for the actual profile measurements, gas samples were taken against the flow direction, i.e., the catalyst bed was positioned upstream of the sampling orifice, fixed in position, while the catalyst bed was moved stepwise in the downstream direction. In this way, a constant total flow rate upstream of the sampling orifice was guaranteed.

To ensure a uniform radial temperature profile for larger reactor diameters (ID 4.0 – 5.6 mm), the reactor tube was heated via an oven. The oven was in direct contact with the reactor tube and covered the reactor tube almost completely, except for the optical access. Reaction temperatures up to 550 °C can be achieved. The oven allowed further to heat a rather long catalyst bed in the axial direction (maximum bed length 6 cm) and to heat the dosed feed mixture to the desired reaction temperature before reaching the beginning of the catalyst bed through a long preheating zone of 4 cm. Notably, two thermocouples were installed, which are relevant for the reaction temperature in the catalyst bed. One thermocouple controlled the heating block temperature, referred to the set temperature (maximum 550 °C). The other one was located inside the sampling capillary, with the tip aligned to the orifice, and thus in the center of the catalyst bed. In this way, temperature profiles were measured in the center of the catalyst bed. A sheath-thermocouple type K using Inconel as sheath material (OD 250 µm, TMH GmbH) was used.

In addition to the reactor oven, a sophisticated and easily to handle heating system up to 200 °C was implemented to prevent water condensation, ensure quick setup assembly, and enable the usage of other chemical systems with condensable compounds. The heating system included a heated reactor housing, transfer lines (heating pipes, Hillesheim GmbH), sampling needle valve (heating jacket, Horst GmbH), and analytical inlet systems.

Structural changes were measured by using catalyst characterization techniques (Figure 3.1, iv), in this work, by means of XAS and XRD. X-rays were directed onto the sample at the very same position as the sampling orifice and thermocouple tip. In this way, the probe volume, formed by the sampling orifices, thermocouple, and X-ray beam remained fixed in space while the reactor tube containing the catalyst bed was shifted laterally along this probe volume with micrometer resolution. The original CPR was designed for Raman-spectroscopy, allowing measurements in reflection mode by directing laser light through the reactor tube onto the sample and collecting the reflected signal on the same way back. In this work, the CPR was modified to enable synchrotron-based measurements in transmission mode.

The experimental setup (i – iv) can be fully automated due to the CPR control system (REACNOSTICS GmbH). For example, flow rates, gas compositions, including periodically modulated inlet concentrations, reactor positioning, temperatures, and heating rates can be controlled. Furthermore, external triggers can be used to start individual GC runs, or, during *operando* experiments, to trigger scattering or spectroscopic measurements at the beamline. A photograph of the control surface is displayed in Figure 3.4.

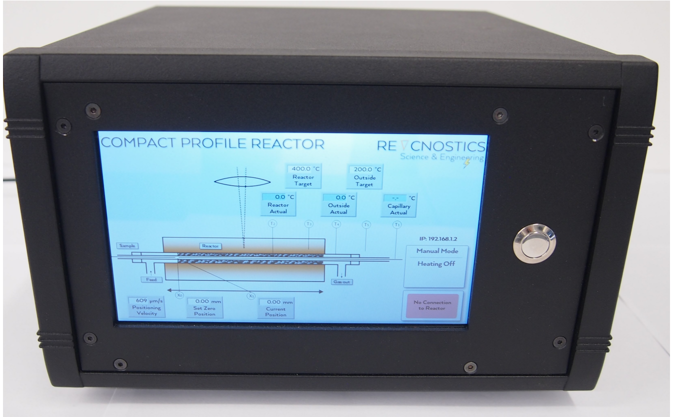

Figure 3.4: Photograph of the reactor control surface.

3.3 Catalyst Activity Investigation

The ODH test reaction system was explored in a systematic catalytic performance study through 38 concentration and temperature profiles measured under various reaction conditions. For this purpose, three experimental plans were designed, which are presented in this section. This part has been conducted by Diego Espinoza and was firstly published in his master thesis as well as in [126].

3.3.1 Experimental Design Plans

The catalyst performance study can be divided into two parts. The first part consists of one and the second part of two experimental design plans. The first part investigates the influence of the main reaction parameters e.g., the effect of feed concentrations (C_2H_6, O_2) and reaction temperature on catalytic performance. Key objectives were to test for catalyst stability and reproducibility of the sampling technique through the catalyst bed as well as to define scan ranges of the aforementioned parameters. Based on the previous tests, the second part includes two face-centered central composite design plans with each two factors. Both plans include the variation of O_2 feed concentration as a factor. The second factor is to test for variations in either C_2H_6 or C_2H_4 as feed component. Reactor temperatures were varied in five steps from 480 to 530 °C for each hydrocarbon, but were not included as a parameter in the measurement plan. The goal is to provide the experimental basis for reliable profile measurements and the development of a kinetic model (Section 3.4).

Before starting each profile run, the catalyst was pretreated to a reference state for one hour in a mixture of O_2:inert = 20:80 at 480 °C. After that, the reactant feed mixture was adjusted according to the experimental kinetic plan, and a time of 90 minutes was given to reach steady state. Reaction temperatures were measured in the reactor heating block and in the center of the catalyst bed. Measured temperatures in the catalyst bed are 10 – 15 K below the set temperatures depending on the level of conversion. Temperatures in the heating block were used as reference points in all measurement plans.

As described above, temperature and inlet compositions are variable parameters in the design plans. An overview of the experimental parameters, maintained constant throughout all profile runs per experimental design plan, are listed in Table 3.2, divided into the design plans from the first and second experimental part.

Table 3.2: Overview of the experimental parameters which are kept constant per design plan.

Design plans	1st part C_2H_6	2nd part C_2H_6	2nd part C_2H_4
reactor tube diameter [mm]	OD 6.0, ID 4.0	OD 6.0, ID 4.0	OD 6.0, ID 4.0
catalyst	30 wt% MoO_3	30 wt% MoO_3	30 wt% MoO_3
support	γ-Al_2O_3	γ-Al_2O_3	γ-Al_2O_3
catalyst particle size [μm]	200 – 400	300 – 400	300 – 400
catalyst bed length [mm]	30	32	32
total flow rate [ml/min]	30	30	40
pressure [bar]	1	1	1
maximum GHSV* [h^{-1}]	4714	4399	5944
* measured at reactor outlet			

Notably, due to a high C_2H_4 reactivity, the flow rate was increased from 30 to 40 ml/min in the second experimental part for the C_2H_4 measurement plan.

1st part: An overview of the experimental plan is shown in Figure 3.5. Ten profile runs were performed, including eight individual runs (P1 – 8) and two replicates (R1 + R8). Inlet concentrations of O_2 (factor 1) and C_2H_6 (factor 2) ranged from 7.5 to 12.5 % or 75 to 125 mbar, respectively. The temperature as the third factor was varied from 480 to 530 °C in two levels.

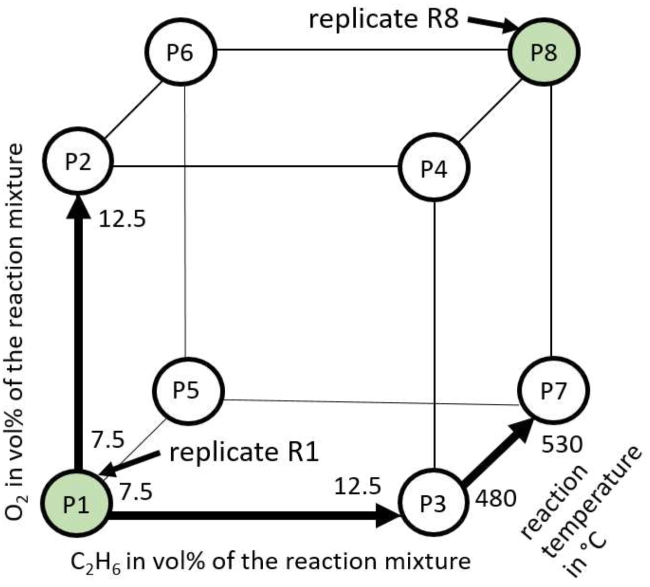

run	vol% of C_2H_6	vol% of O_2	T in °C
P1	7.5	7.5	480
P2	7.5	12.5	480
P3	12.5	7.5	480
P4	12.5	12.5	480
P5	7.5	7.5	530
P6	7.5	12.5	530
P7	12.5	7.5	530
P8	12.5	12.5	530
R1	7.5	7.5	480
R8	12.5	12.5	530

Figure 3.5: Schematic representation of the two-level, three-factor experimental design plan with $2^3 = 8$ spatial profile measurements. Factor 1: Vol% of O_2 in the reaction mixture from 7.5 – 12.5 %; Factor 2: Vol% of C_2H_6 in the reaction mixture from 7.5 – 12.5 %; Factor 3: Reactor target temperature from 480 – 530 °C. Reaction conditions: 1 bar, catalyst bed length 30 mm, 30 ml/min.

2nd part: An overview of all experiments performed in the second part is given in Figure 3.6. The left picture shows 13 profile runs (P5 – 13) that were performed to study the effect of O_2 and C_2H_6. The four profile runs at the cube corners (P5 – 8) were measured in the 1st part. To obtain the face-centered central composite design, all axial measurement points projected on the surfaces (P9 – P12) and the central point (P13) were measured in addition. Further, four replicates of the central point (R13a – d) were made. Replicates were uniformly distributed through the campaign to test for stable operation. The effect of C_2H_4 was studied within 13 profiles (P14 – 22) and again four replicates of the central point

(R18a – d). At the end of each measurement plan, four more runs were subsequently conducted at the central point at different temperatures 480, 500, 520, and 540 °C (T13a – d and T18a – d), respectively. Concentration profiles were measured at 19 positions along the catalytic bed, with steps of 3 mm between sampling points. A higher point density of 1 mm was used in the first 6 mm of the catalytic bed in order to properly measure the initial rate of consumption/production of relevant compounds.

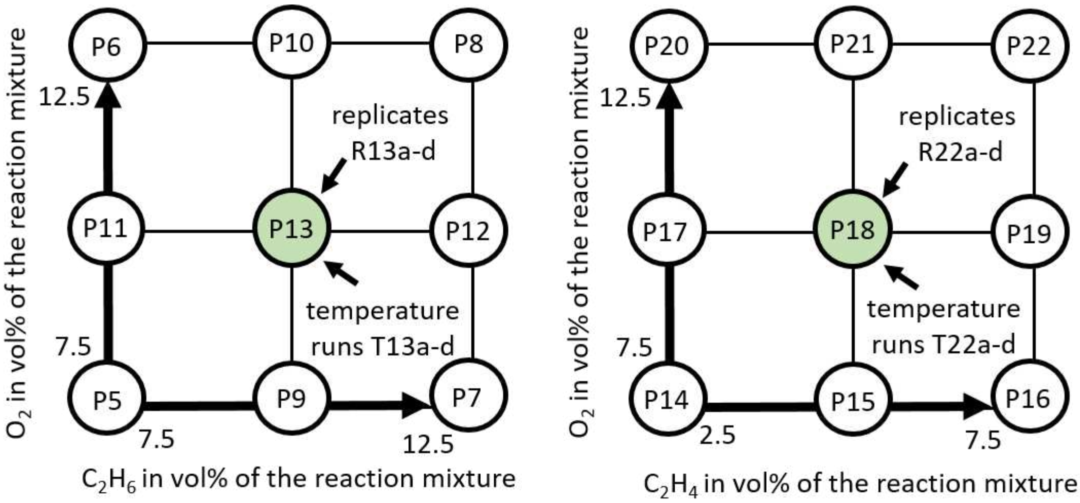

Figure 3.6: Schematic representation two three-level, two-factor experimental design plans with $3^2 = 9$ spatial profile measurements. Factor 1: Vol% of O_2 in the reaction mixture at 7.5, 10, 12.5 %; Factor 2: Vol% of C_2H_x in the reaction mixture from 7.5, 10, 12.5 % (left) and 2.5, 5, 7.5 % (right). Reaction conditions: 530 °C, 1 bar, catalyst bed length 32 mm, C_2H_6: 30 ml/min; C_2H_4: 40 ml/min.

3.3.2 Gas Analysis via MS

The gas phase composition of the sampled stream was analyzed using a Hiden HPR 20 MS, equipped with a heated capillary inlet to prevent water condensation. A Faraday detector, operating in Multiple Ion Detection (MID) mode, was used to monitor the mass-to-charge ratios m/z listed in Table 3.3.

Signal contributions from other reaction components to peaks 27 and 28 were corrected by subtracting the contributions of hydrocarbons and carbon dioxide to these signals. Gas quantification via MS is further described in detail in Section 3.7.

Table 3.3: Analyzed mass-to-charge ratios m/z used for gas analysis of the sampling stream.

Species	Analyzed m/z-ratios
C_2H_4	27
CO	28
C_2H_6	30
O_2	32
Ar	40
CO_2	44

3.4 Kinetic model

Profile experiments presented in the previous section were used for developing a kinetic model that predicts the species profiles in the oxidation zone of the reactor correctly. The kinetic model development, including the applied reactor model, the procedure of fitting complete reactor profiles, considered reactions, and assumption in the MVK mechanism are presented in the following section. The content of this section was also part of the master thesis by Diego Espinoza and published in [126].

3.4.1 Reactor Model

A 1D pseudo-homogeneous plug flow reactor with constant density, constant temperature and constant pressure was modeled in order to perform parameter estimation:

$$\frac{dC_i}{dz} = \frac{(R_{i,net} \cdot \rho_{bed})}{U_z} \tag{3.1}$$

Where C_i is the molar concentration of component i, $R_{i,net}$ is the weight base net rate of consumption / production of component i, ρ_{bed} is the bed bulk density, z is the axial position along the catalytic bed and U_z is the gas velocity in axial direction. Finally, the net rate of species i was determined by:

$$R_{i,net} = \sum_j v_{ij} \cdot r_j \tag{3.2}$$

Where v_{ij} is the stoichiometric coefficient of species i in reaction j, and r_j is their respective rate.

3.4.2 Profile Data Fitting

The general fitting problem consists of solving a set of Ordinary Differential Equations (ODEs) derived out of Eq. 3.1 for all components involved in the reaction system. Thus, in this work a Matlab script (Matlab®, v2019a) was developed to perform an integral data analysis of the concentration profile measurements presented in Section 3.3. The Matlab script solved a set of ODEs with molar concentrations as response variables by an already implemented solver ode23s. Once the ODEs were solved, the optimization algorithm lsqcurvefit was used to evaluate the difference between the experimental data and the currently predicted data. The optimization algorithm included a nonlinear fitting procedure according to Eq. 3.3 that calculated the difference between predicted molar concentration $F(p, pdata_i)$ and its experimental values *cdata* from the profile measurements. The goal was to find the kinetic parameter p that minimizes Eq. 3.3.

$$\min_p \|F(p, pdata) - cdata\|_2^2 = \min_p \sum_p \left(F\left(p, pdata_i\right) - cdata_i\right)^2 \tag{3.3}$$

Additionally, a constrained nonlinear optimization algorithm was applied in the program in order to ensure that estimated kinetic parameters were non-negative numbers. As soon as the algorithm found a reasonable solution, the optimization stopped and the final values of kinetic parameters (fitting parameters) as reaction order, pre-exponential factor and activation energies were obtained.

Initial guesses of pre-exponential factors and activation energies were important in the fitting procedure because they allowed to find the global minimum of the system instead of local minimum points. Activation energy guesses were obtained from Arrhenius plots by using concentration profiles obtained from the temperature runs P14 – 17 (C_2H_6) and P27 – 30 (C_2H_4) in the range of 480 – 540 °C. The experimental concentration profiles were fitted simultaneously as complete reactor profiles in the developed script. In simple terms, each species concentration profile included eleven data points measured through the catalyst bed (eleven distinguished conversion levels). The optimization algorithm minimized in an iterative process (predicted vs. experimental) the sum of squares of all data points within one species concentration profile for five different species (C_2H_6, C_2H_4, CO, CO_2 and O_2) at four temperatures together (in total 20 profiles). Hence, the profile data at 480 – 540 °C were not evaluated successively which as a result provided only one set of fitting parameters. In the present work, the set temperature was used for fitting the profiles but in principle it is possible to incorporate the temperature profile in the fitting. This will be subject of further work.

In order to avoid parameter correlation between the pre-exponential factor and activation energy of the Arrhenius equation, a reparametrized form of this equation was employed.

$$k = k_{ref} \exp\left[\frac{-E}{R}\left(\frac{1}{T} - \frac{1}{T_{ref}}\right)\right] \tag{3.4}$$

Where k_{ref} represents the specific reaction rate at the reference temperature T_{ref} which for this study is represented as the average temperature in the range of 480-540 °C.

$$k_{ref} = A_0 \exp\left[\frac{-E}{R \cdot T_{ref}}\right] \tag{3.5}$$

3.4.3 Mars-Van Krevelen Mechanism

In order to obtain a deeper physical insight into our reaction system, a MVK approach was followed. The kinetic model developed in this work considers a set of reactions presented in Table 3.4. The main reaction is the ODH of ethane to ethylene (Reaction step 1). Additionally, the network includes the partial and total combustion of ethane and ethylene to CO_x as shown in Reactions 2 – 5. Finally, the reoxidation of the catalyst by gas phase oxygen is taken into account and represented by Reaction step 6. Here, the reaction constant is represented by k_i, the molar fraction of component i in the gas phase by y_i and the fraction of oxidized catalyst sites by θ_{ox}. From a chemical point of view, the latter is defined in the way that $\theta_{ox} = 1$ represents the catalyst in its fully oxidized state und thus MoO_3. Inversely, if the catalyst is reduced, corresponding to MoO_2. Further, each reaction has two fitting parameters (A_0 and E_a). In addition, Reaction 6 contains the reaction order n as fitting parameter, describing how sensitively the reoxidation depends on the partial pressure of oxygen.

Table 3.4: Considered reaction steps in the MVK model for ODH of ethane.

Step	Reaction equation	Rate expression
1	$C_2H_6 + O_l \xrightarrow{k_1} C_2H_4 + H_2O + l$	$r_1 = k_1 y_{C_2H_6} \theta_{ox}$
2	$C_2H_6 + 5\,O_l \xrightarrow{k_2} 2\,CO + 3\,H_2O + 5\,l$	$r_2 = k_2 y_{C_2H_6} \theta_{ox}$
3	$C_2H_6 + 7\,O_l \xrightarrow{k_3} 2\,CO_2 + 3\,H_2O + 7\,l$	$r_3 = k_3 y_{C_2H_6} \theta_{ox}$
4	$C_2H_4 + 4\,O_l \xrightarrow{k_4} 2\,CO + 2\,H_2O + 4\,l$	$r_4 = k_4 y_{C_2H_4} \theta_{ox}$
5	$C_2H_4 + 6\,O_l \xrightarrow{k_5} 2\,CO_2 + 2\,H_2O + 6\,l$	$r_5 = k_5 y_{C_2H_4} \theta_{ox}$
6	$l + 0.5\,O_{2(g)} \xrightarrow{kox} O_l$	$r_{ox} = k_{ox} y_{O_2}^{n} \theta_{red}$

To derive the modeling equations for each one of the fitted components in Eq. 3.1, the following assumptions were made in the MVK approach:

1. Only one active lattice oxygen species exists.

$$1 = \theta_{ox} + \theta_{red} \tag{3.6}$$

2. The catalyst is in steady state, meaning that the rate of catalyst oxidation equals the rate of catalyst reduction. This can expressed by the following equation:

$$R_{ox} = R_{Red} \tag{3.7}$$

By considering the aforementioned assumptions and the site balance equation, the following equation for the determination of the oxidized sites coverage was derived.

$$\theta_{ox} = \frac{k_{ox} \cdot y_{O_2}^{n}}{k_{ox} \cdot y_{O_2}^{n} + (k_1 + 5k_2 + 7k_3)\, y_{C_2H_6} + (4k_4 + 6k_5)\, y_{C_2H_4}} \tag{3.8}$$

3.5 *Operando* Profiling using X-Ray Absorption

The focal point of this work is the development of new *operando* profile methodologies that allow us to measure simultaneously local gas compositions, temperatures, and structural information of the catalyst. One of the developed measurement concepts focuses on coupling spatial profiling with XAS. For this, experiments were carried out at PETRA III, DESY using the photon beamline P64. This section describes briefly the methodological approach (Subsection 3.6.1), setup integration at P64 (Subsection 3.5.2), experimental details on the conducted profile measurements (Subsection 3.6.3), gas analysis via micro GC (Subsection 3.5.4), as well as XRD data reduction and analysis (Subsection 3.5.5).

3.5.1 Methodological Approach

This subsection aims to provide a brief overview of the methodological approach for *operando* profile experiments using XAS. In contrast to catalyst activity investigation experiments (see Section 3.3), *operando* experiments were performed until full conversion of gas phase oxygen. As in detail described in Section 3.2, the setup comprised (i) gas dosing system; (ii) spatial profile reactor; (iii) gas analytic; and (iv) characterization technique. More specifically with respect to the performed experiment at P64, (i) three MFCs; (ii) synchrotron CPR-XAS; (iii) micro GC; and (iv) XAS instrument with ionization chambers as detectors (Figure 3.7).

The CPR was modified to enable XAS measurements in transmission mode (iv). For technical details on the reactor modification, the reader is referred to Subsection 5.1.1. The XAS measurements were carried at the Mo K-edge around 20 keV during ethane ODH conditions and within one beamtime, allocated at P64, PETRA III in October 2019 (Proposal No. I-20190246). One of the main challenges in absorption experiments was to measure a sufficient number of photons downstream of the sample, and thus to ensure that enough photons transmitted through the rather thick CPR reactor tubes. In order to fulfill this condition, the weight loading of Mo on the catalyst as well as the wall thickness of the fused silica reactor tube were optimized, having both strong influence on photon absorption. A detailed description of requirements, considerations, and limitations for *operando* XAS experiments with the CPR-XAS is presented in Subsection 5.1.2. For gas quantification a micro GC was used (Subsection 3.5.4).

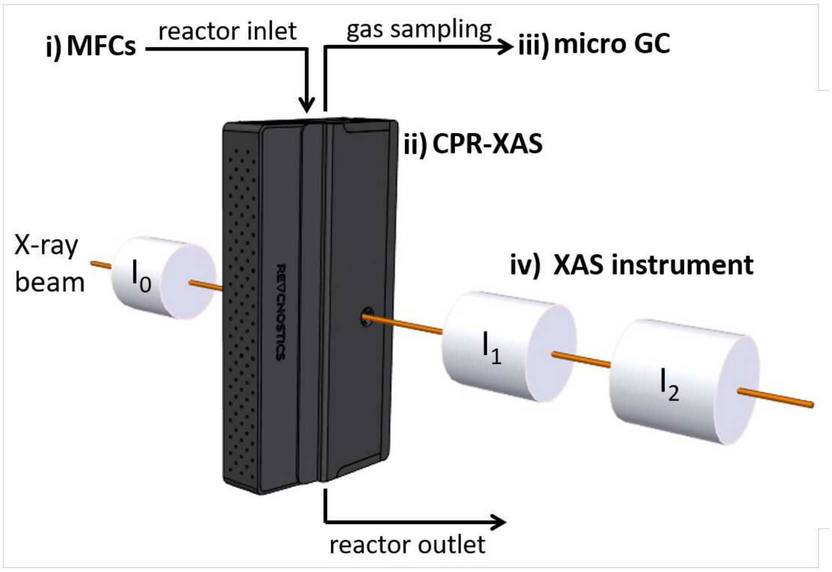

Figure 3.7: Schematic of the experimental setup used to measure temperature, concentration and XAS profiles in transmission geometry by means of the modified CPR-XAS system.

3.5.2 Reactor Setup Integration at Beamline P64

XAS spectroscopy has developed hand in hand with synchrotron radiation facilities, resulting in commonly established beamlines dedicated to XAS experiments. However, many material studies are carried out ex-situ or in much smaller setups compared to the introduced catalytic profile reactor setup. Since beamlines have usually limited space for the accommodation of large setups and a restricted number of gases simultaneously usable, technical compatibility of the CPR-XAS setup and involved gases must be taken into consideration during the planning phase. Beamline P64 enables EXAFS and QEXAFS experiments in the energy range of 4 – 44 keV and offers space and infrastructure to integrate the CPR setup. A picture of the experiment is shown in Figure 3.8.

The beam height is fixed in space with 383 mm above the experimental table or 285 ± 25 mm above a breadboard with an X95rail. The reactor was positioned on the provided X95 rail with a specifically developed adapter system, tailored to easily mount and align the reactor window with the beam position (Figure 3.9).

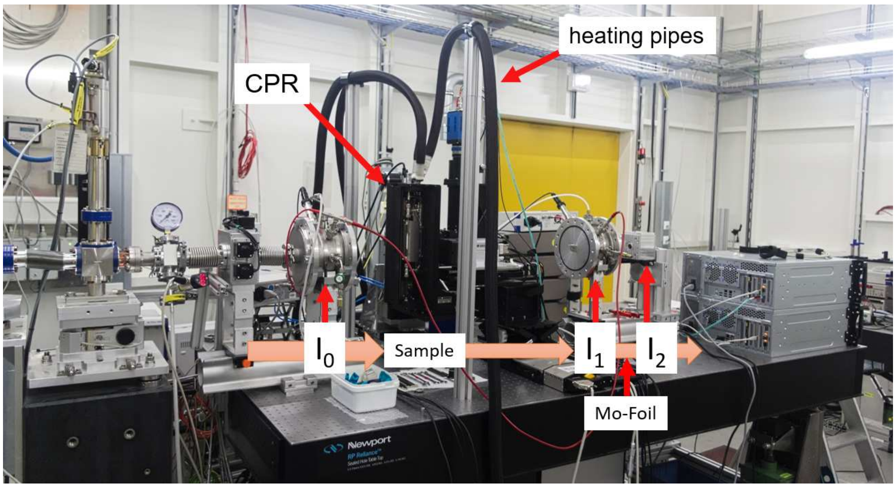

Figure 3.8: Photograph of the experimental setup installed at beamline P64, PETRA III.

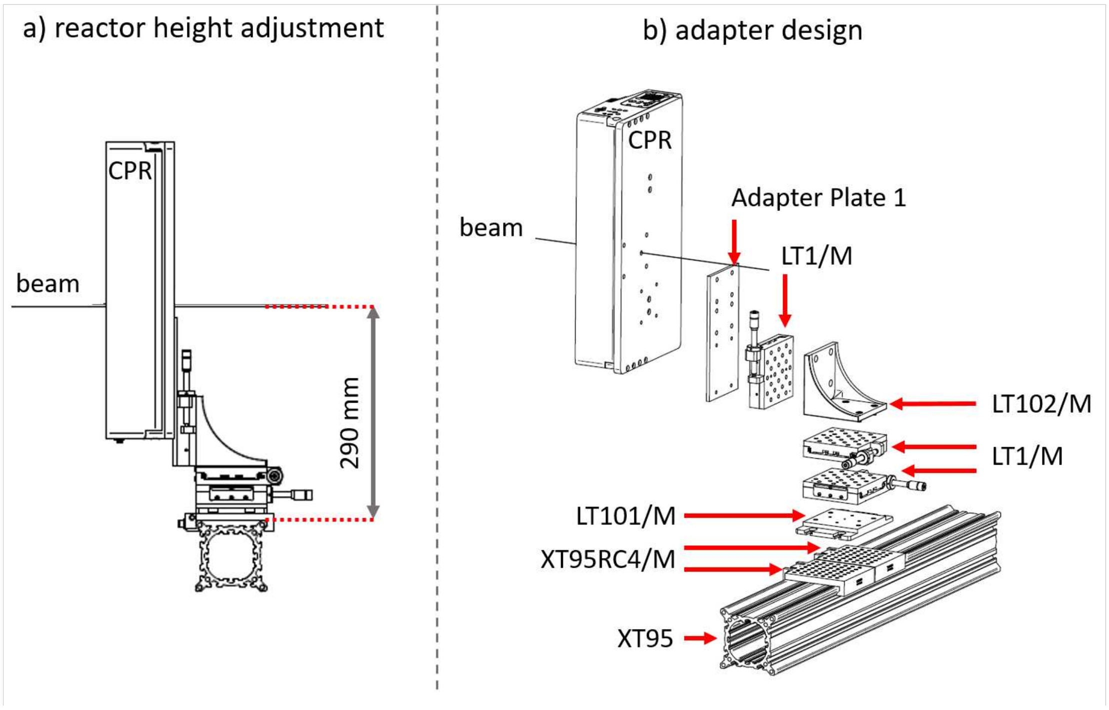

Figure 3.9: Adapter system used to mount and align the reactor at beamline P64. (a) Adjustment of the reactor window in height with the fixed position of the X-ray beam. (b) Overview of adapter design components. Figure 3.9b is included in an article submitted to [125].

The adapter design comprised in total ten parts, one specifically designed adapter plate built by the workshop of the TUHH, as well as nine parts purchased from Thorlabs GmbH. The adapter plate had the function to adjust the reactor to the proper beam height (Adapter Plate 1, Figure A.1. The Thorlabs parts were compatible with the X95 rail and with the Adapter Plate 1. The Thorlabs parts included three single-axis translation stages that each provided a travel distance of 50 mm on the respective axis with high precision. In this way, a more flexible reactor positioning was given at different beamlines and precise vertical positioning between the reactor sample window and the beam could be enabled by laser alignment.

Noteworthy, the cooling plate of the reactor was mounted with a slight offset on the reactor to match the openings in the cooling plate, reactor housing, and heating block for X-ray transmission, illustrated in Figure 3.10. Since the adapter design was mounted to the cooling plate, the sample position in the horizontal direction shifted slightly by 10 mm.

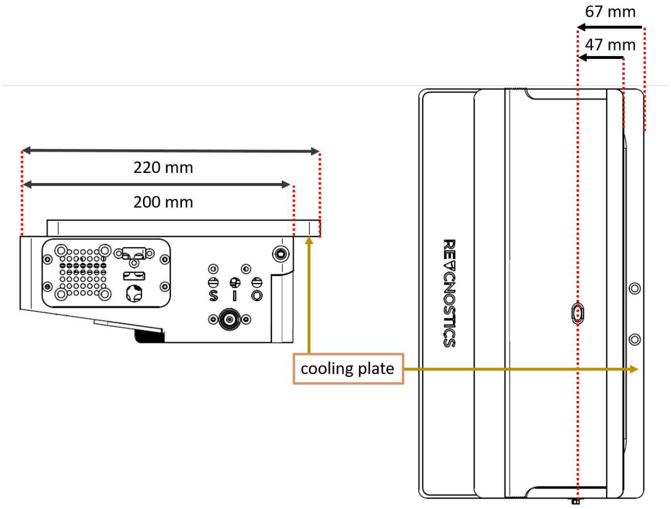

Figure 3.10: New position of the reactor window in horizontal direction by mounting the cooling plate on the reactor with a horizontal shift of 20 mm.

As denoted in Figure 3.8, P64 provides three ionization chambers, enabling measurements of the sample and the reference spectra simultaneously. The reactor was positioned between the first and second ion chamber and a reference sample between the second and third.

Gas infrastructure was available for flammable, toxic, oxygen, and inert gases with stainless steel lines (OD 6 mm) and quick-connection valves from Swagelok (product series QC4). Pressurized air was supplied with 6 bar by flexible tubing and fitting connections from Festo. Cooling water supply at low pressures was offered by a Julabo Chiller with quick-connectors (coupling series male-female, type: NS4D22006). All connections, required to integrate the setup with existing quick-connectors, were provided by the users. Furthermore, for experiments involving gases, high safety standards (gas detectors, high air exchange in the hutch, effluent gas) were ensured, as well as a gas dosing system, and gas analysis via MS was provided upon request. To conclude, P64 is an adequate beamline for complex *operando* experiments in the field of heterogeneous catalysis.

For further information on general specifications, optics (monochromators, mirrors), and the end station (detectors, measurement modes, control and data analysis) is referred to the webpage of P64, DESY [127].

3.5.3 Experimental Details

During the beamtime at P64, one profile run was conducted with the simultaneous measurement of spatially-resolved gas compositions, temperatures, and XAS spectra.

The profile experiment was carried out with a 10 wt% MoO_3/γ-Al_2O_3 catalyst and a particle size of 200 – 400 µm. In contrast, a 30 wt% MoO_3/γ-Al_2O_3 catalyst was applied throughout all profile measurements in this work. Additionally, the catalyst was packed in a reactor tube with an ID of 4.8 mm. The wall thickness was reduced from 1000 μm, applied in the catalyst performance studies, to 600 μm. Both parameters, weight loading of Mo and reactor tube wall thickness, were chosen according to the results obtained from optimizing photon absorption (Subsection 5.1.2).

Prior to recording the profile, several alignment steps were conducted. First, the thermocouple tip was aligned with the sampling orifice. Second, alignment of the X-ray beam and the sampling orifice in the sampling capillary was ensured by laser alignment in combination with micrometer precision stages. Finally, the X-ray beam was positioned next to the capillary by moving the reactor in horizontal direction. Next, it was verified that the X-ray beam did not hit the stainless steel sampling capillary at any sampling position throughout the entire catalyst bed by evaluating the absorption behavior. At the same time, the start and end position of the catalyst bed were determined.

Due to the particular importance for sophisticated method development of achieving 100 % gas phase oxygen conversion, reaction conditions were chosen accordingly, aiming to find optimal values for total flow rates, gas compositions, and reaction temperatures. The reaction was performed under steady state conditions at a constant inlet feed, consisting of ethane, oxygen and as diluent a mixture of 8 % helium in argon with gas compositions of C_2H_6/O_2/inert:10/10/80. The reaction conditions were 515 °C, ambient pressure, and a total flow rate of 20 ml/min corresponding to a Gas Hourly Space Velocity (GHSV) of 1646 h^{-1}. Notably, in the standard CPR a set temperature of 515 °C equals the temperature measured in the center of the catalyst bed. The synchrotron CPR-XAS has additional openings that required to set higher temperatures in the heating block (530 °C) to reach similar temperatures (515 °C). Prior to recording the profile run, the reaction was running for 90 min to reach steady state.

XAS measurements were carried out in transmission geometry around the Mo K-edge (20 keV) with three ionization chambers in series. The incident beam energy was selected by a Si(111) double crystal monochromator and higher harmonics were rejected by a pair of Rh-coated mirrors. Spectra were recorded in continuous mode (1300 eV in 300 s). The beam size was approx. 0.5 mm^2. Spectra of a Mo foil placed between the second and third ionization chamber (reference channel) were measured simultaneously with *operando* sample spectra for energy calibration.

An overview of the corresponding experimental parameters is listed in Table 3.5 below, divided in reactor specifications, operation conditions, and XAS.

3.5.4 Gas Analysis via Micro-GC

The gas phase composition of the sampling flow was determined using a micro GC from Agilent GmbH, providing the advantages of a fast gas analysis and a compact design compared to traditional GCs. The micro GC was equipped with four gas channels. Three channels utilized helium as carrier gas and one argon. Helium

Table 3.5: Overview experimental parameters used for *operando* profile measurements at P64.

Experimental parameters	Beamline P64 October 2019
Reactor tube diameter [mm]	OD 6.0, ID 4.8
Sampling capillary [μm]	OD 700, ID 520
Sampling orifices [μm]	4 x 100
Catalyst	10 wt% $MoO_3/\gamma\text{-}Al_2O_3$
Catalyst bed length [mm]	35
Catalyst particle size [μm]	200 – 400
Flow rate [ml/min]	20
Temperatures [°C]	515 (capillary), 530 (set)
Pressure [bar]	1
GHSV [h^{-1}]	1646
Inlet composition C_2H_6/O_2/inert [vol%]	10/10/80
Beam size [mm]	0.5 x 0.5
Energy [eV]	19700 - 21000

was used as internal standard, evaluating the helium signal on the argon channel. In order to obtain comparable signals in magnitude between the internal standard and the reaction mixture, a bottle containing 8 vol.% helium in argon was used. A MolSieve column was used to separate the permanent gases He, H_2, O_2, CO and a Plot Q column to separate C_2H_6, C_2H_4 and CO_2. A TCD measured the separated components eluted off the columns. Water and CO were calculated with the atom species balance of the reaction mixture. The procedure for gas quantification is described in detail in Section 3.7.

3.5.5 XAS Data Analysis

XAS measurements were carried out with three ionization chambers in series, providing signal outcomes in current I. All three signal measurements were combined to obtain two pairs of transmission data. The first transmission data pair was from the sample, measured between I_0 and I_1, while the second pair was from the corresponding reference, measured between I_1 and I_2. By using Beer's law (see Eq. 2.14), the raw data were converted to $\mu(E) \cdot x$ as a function of energy. Prior to detailed analysis, several data processing steps were performed, known as data reduction steps. An overview of this procedure is illustrated in Figure 3.11, including three steps: calibration and alignment (1^{st} step), choosing E_0 (2^{nd} step), and normalization (3^{rd} step).

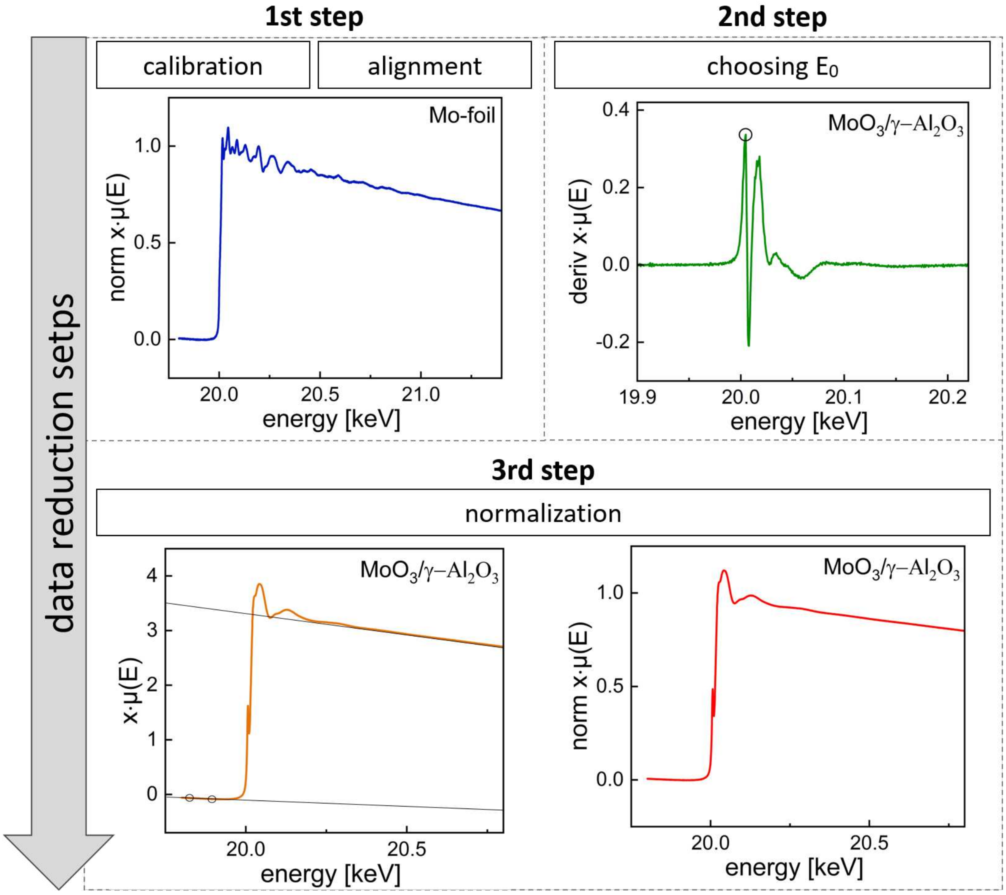

Figure 3.11: Overview of data reduction steps for processing XAS data prior to analysis.

The 1^{st} step involved choosing and calibrating a standard, in this case, a Mo foil. The calibration was performed by selecting the E_0 position, i.e., commonly the first inflection point in the spectrum, and setting this position to a tabulated value for the Mo K-edge energy (19.9995 keV). The Mo foil was further used as reference material, together measured with each sample spectrum. This measurement configuration has the advantage that instrument-related effects such as an unstable behavior from the monochromator can be canceled out from each spectrum. Each reference measurement was aligned to the standard by shifting the spectrum in energy. The same shift in energy, required for each reference scan, was applied to the corresponding sample scan, which was simultaneously measured.

In the 2^{nd} step, the E_0 value for the sample measurements was chosen, again by taking the maximum of the first peak of the first derivative.

The 3^{rd} and last step aims to put the spectra in a standard and normalized form in order to make the spectra independent of other sample or setup-related factors, e.g., sample thickness, gains on amplifiers, type of gas filled within the ionization chamber, and thus comparable quantitatively within one profile run or to other references standards. The normalization performed is known as edge-jump normalization. The spectrum was divided by its edge jump, resulting in $\Delta\mu(\mathrm{E}) = 1$, and shifted for obtaining a rising edge from 0 to 1.

The normalized spectra allowed more detailed analysis as performed in this work by Linear Combination Analysis (LCA).

LCA of the XAS profile was performed in the range of 19,980 to 20,030 eV using as internal references spectra measured at the beginning (2 mm) and end (34 mm) of the catalyst bed.

$$w \;\cdot\; Pos\ 2\ (E) + (1-w)Pos\ 34\ (E), w \in [0,1] \tag{3.9}$$

Error bars from the fits with internal references were within ±0.4%. Athena software was used for calibrating and normalizing all spectra as well as for performing LCA [128].

3.6 *Operando* Profiling using X-Ray Diffraction

The second focal point of this work is to extend the previously developed *operando* profile methodology by means of XAS to XRD. For this purpose, experiments were carried out at PETRA III, DESY using the photon beamlines P07 and P21.1 with one beamtime allocated respectively. In this section, details on the methodological approach, setup installation at both beamlines, conducted profile measurements, as well as gas and XRD analysis are given.

3.6.1 Methodological Approach

As an amendment to Section 3.2, the experimental setup used for spatially-resolved *operando* XRD measurements consisted of (i) three MFCs; (ii) synchrotron CPR-XRD; (iii) GC or MS; and (iv) XRD instrument with an area detector (Fig. 3.12). For meaningful method development, it was again important to achieve full gas phase oxygen conversion during ethane ODH and to choose reaction conditions accordingly (see next Subsection 3.6.3).

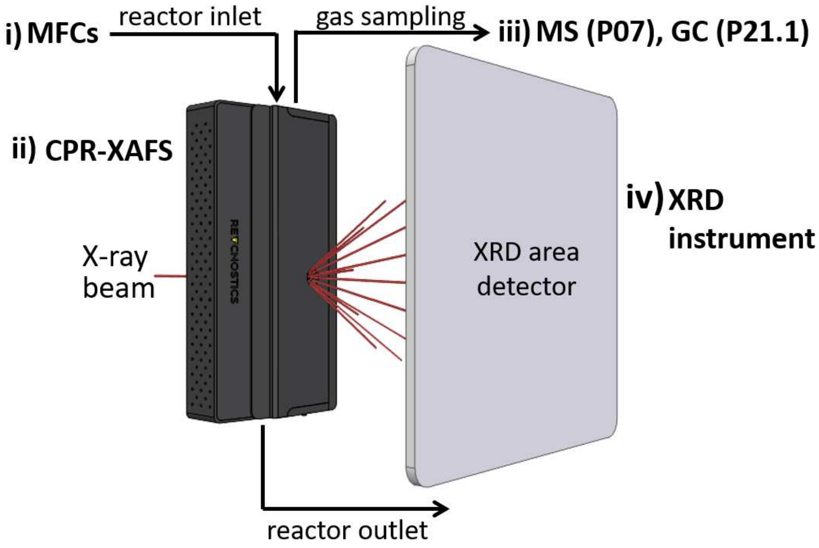

Figure 3.12: Schematic of the experimental setup used to measure temperature, concentration, and XRD profiles in Debye-Scherrer geometry by means of the modified CPR-XRD reactor system.

The CPR-XAS was further modified to the CPR-XRD (ii), capable of performing XRD measurements in transmission geometry (iv). In contrast to the CPR-XAS, stronger reactor modifications were required to collect scattered X-ray signals over a defined angular range (see Subsection 6.1.1). Method development was addressed in two beamtimes. First, an in-house beamtime at P07 in March 2021 was used to test technical feasibility with the modified CPR-XRD coupled to the XRD instrument (Proposal No. I-20010075). Furthermore, the in-house beamtime was used to implement a link between the reactor and beamline control systems for running the entire experiment fully-automized by starting the XRD measurements from the reactor control unit via an external trigger. For fast gas analysis at P07 a MS, the same one as for the catalytic performance studies (Subsection 3.3.2), was used. Fast analysis was important to focus on method feasibility, including to identify potential sources of errors and improvements, in the given time of two to three days, and further, to follow transient reaction conditions.

In the second beamtime, a similar experiment to P07 was conducted at beamline P21.1 in August 2021 to gain experience with the combined techniques and to test for applicability of the *operando* profile reactor setup with other beamlines (Proposal No. I-20210520). For gas quantification at P21.1 a GC was used (see Subsection 3.6.4). More details on the procedure followed for method development are given in Section 6.1.

3.6.2 Reactor Setup Integration at Beamlines P07 and P21.1

Beamlines for high-energy XRD experiments are commonly established at synchrotron radiation facilities. Examples are the beamlines P07 and P21.1 (PETRA III, DESY), which are optimized for high-energy material science. While P21.1 is specialized for XRD and TS, offering various 2D area detectors, P07 satisfies scattering and imagining techniques, providing a wider range of detection modes, detector types, as well as smaller beam sizes.

The experimental hutches from P07 and P21.1 were very similar and well-designed for *operando* catalysis measurements. For example, both beamlines offered space and infrastructure to integrate the CPR-XRD setup, flexible reactor installation and positioning, a large number and type of gas connections (flammable, toxic, oxygen, and inert), pressurized air, water cooling via a Julabo Chiller, high safety standards (gas detectors, high air exchange in the hutch, effluent gas), as well as gas analysis via MS upon request. Line connections were designed with 6 mm and festo. A photograph of the installed setup at P07 with different views is shown in Figure 3.13 (representing P21.1).

The beam positions at P07/P21.1 were fixed in space to the same beam height of 3155 mm above the sample stages. Sample stages were installed as standard equipment for high-load capacities and multi-axis motions with high accuracy. In addition, the sample stages were equipped with a uniform hole pattern that

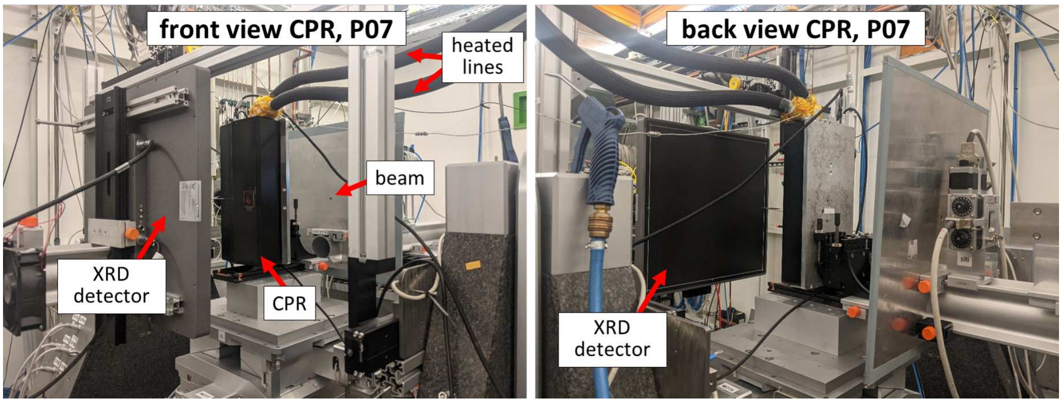

Figure 3.13: Photograph of the experimental setup installed at beamline P07, PETRA III. The same experimental setup was used for measurements at beamline P21.1.

enabled identical reactor installation at P07/P21.1. For positioning the reactor window in the horizontal and vertical directions according to the respective beam position, the adapter design introduced for P64 (Subsection 3.5.2) was used as a basis. Figure 3.14a shows the slightly modified adapter design.

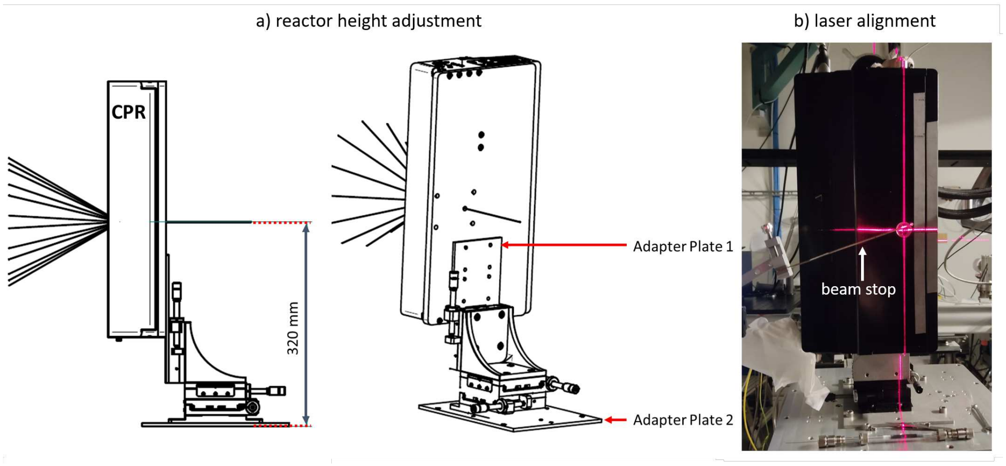

Figure 3.14: (a) Lateral and back view of the assembled adapter system used to mount the reactor and align the reactor window in horizontal and vertical directions according to the fixed position of the beam in space. (b) Photograph showing the reactor front and the laser light used for alignment.

The Adapter Plate 1 (see Subsection 3.5.2, Fig. A.1) was designed with several hole patterns to match beam positions at different beamlines, including P07/P21.1.

The main difference, compared to the reactor installation at P64, was the installation of the reactor on the beamline sample stage at P07/P21.1. For this purpose, Adapter Plate 2 was designed and built by the workshop of the TUHH (Fig. A.2). The Adapter Plate 2 had the function to mount the reactor centered on the beamline sample stage, considering the different position of the reactor opening imposed by the shifted cooling plate. The Thorlabs assembly provided again a flexible positioning in x-y-z directions, and thus precise vertical alignment of the reactor window and the beam stop to the beam, illustrated in Figure 3.14b.

For further information about the beamlines, the reader is referred to the webpage of P07 [129] or P21.1 [130].

3.6.3 Experimental Details

In the following subsection details on the *operando* XRD experiments carried out at beamline P07 in March 2021 and P21.1 in August 2021 are presented.

A packed reactor tube after running the reaction is shown in Figure 3.15, exemplary for experiments at P07 and P21.1.

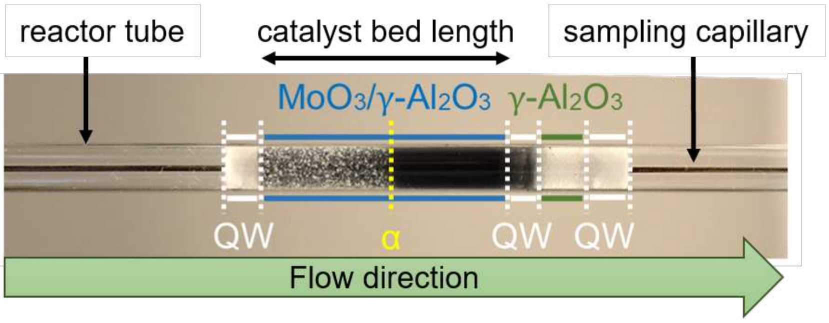

Figure 3.15: Reactor tube loaded with catalyst (MoO_3/γ-Al_2O_3), support material (γ-Al_2O_3), sampling capillary, as well as Quartz Wool (QW) to hold the packing in place. α (yellow dotted line) marks a change in color of the catalyst, referred to as the Color Inflection Point (IP).

The reactor tube was loaded with a 30 wt % MoO_3/γ-Al_2O_3 catalyst, γ-Al_2O_3 (support material), sampling capillary, as well as quartz wool (QW) to hold the packing in place. Since each diffractogram from the catalyst sample had signal contributions from the reactor tube (fused silica) and support material (γ-Al_2O_3), XRD measurements of the individual materials allowed precise signal assignment.

α (yellow dotted line) marks the IP. Corresponding information on the reactor tube dimensions, sampling capillary, catalyst, and catalyst bed length are given in Table 3.6.

Table 3.6: Reactor specifications applied during experiments at P07 and P21.1.

Experimental parameter Reactor specifications	Beamline P07 March 2021	Beamline P21.1 August 2021
Reactor tube diameter [mm]	OD 6.0, ID 5.6	OD 6.0, ID 5.0
Sampling capillary [μm]	OD 700, ID 520	OD 700, ID 520
Sampling orifices [μm]	4 x 50	4 x 50
Catalyst	30 wt% MoO_3/γ-Al_2O_3	30 wt% MoO_3/γ-Al_2O_3
Catalyst bed length [mm]	38	30
Catalyst particle size [μm]	300 – 400	300 – 400
Position α [mm]	18	18

The main difference between the two experiments was the applied wall thickness of the reactor tube (P07: 200 μm; P21.1: 500 μm). A thinner wall is preferable in terms of lower signal contributions from fused silica, and improving particle statistics by having more catalyst particles probed at constant reactor ODs. However, reactor tubes with a lower walls thickness are more fragile and only compatible with lower reactor pressures. In order to provide the basis for more complex, high-pressure reaction systems a thicker reaction tube was utilized in the second beamtime at P21.1.

Prior to measuring the first profile, a similar alignment procedure as described for *operando* XAS at P64 (Subsection 3.6.3) was followed at P21.1. Here, the beginning and end of the catalyst bed was determined by evaluating the Debye-Scherrer rings obtained from the different materials (QW, support, catalyst bed). In contrast, P07 had the technical possibility to use the X-ray eye that enabled to track the sampling orifice position and thermocouple tip by recording images. In this way, the difference in position between the thermocouple and sampling orifice was precisely determined, resulting in deviations of 1.6 mm at reaction conditions. Furthermore, the X-ray beam was aligned exactly to the target position.

Further experimental parameters providing information on operation conditions are listed in Table 3.7.

Table 3.7: Reaction conditions applied during experiments at P07 and P21.1.

Experimental parameter Reaction conditions	Beamline P07 March 2021	Beamline P21.1 August 2021
Flow rate [ml/min]	15	12
Temperature [°C]	515	5151
Pressure [bar]	1	1
GHSV [h^{-1}]	978	1248
Inlet composition C_2H_6/O_2/inert [vol%]	10/10/80	10/10/80

The reactions were operated under steady-state conditions at a constant inlet feed of C_2H_6/O_2/inert:10/10/80 and a reaction temperature of 515 °C. The reaction was hold 90 min time on stream before measurements were begun, ensuring constant catalytic performance. Notably, the stronger reactor modification for the CPR-XRD (see Subsecion 6.1.1), compared to the CPR-Raman or CPR-XAS, required a higher set temperature in the heating block (550 °C) to reach similar inlet temperatures (515 °C) measured in the center and upstream of the catalyst bed. Overall, during *operando* XRD experiments at P07 one individual profile run(1_SS) with one additional replicate profile run (2_SSR) were conducted, while at P21.1 only one profile was measured. The gas analysis differed in both experiments, using an MS at P07 and a GC at P21.1. Details on gas analysis are provided in Subsection 3.6.4.

Table 3.8 and Table 3.9 show an overview of the XRD settings in the experiment at P07 and P21.1.

XRD measurements were performed in transmission mode. The energies of the incident X-rays were chosen by Si(111) single-bounce monochromators with fixed angles corresponding to 101.6 keV, $\lambda = 0.1220$ Å (P21.1) and 103.6 keV, $\lambda = 0.1199$ Å (P07). The beam sizes were reduced and square-shaped by slits to 0.8×0.8 mm^2 (P21.1) and 0.5×0.5 mm^2 (P07) to prevent hitting the stainless steel capillary during translation of the reactor bed. XRD patterns were recorded in transmission mode over a 2θ range from 1.3 to 11° using a 2D 410×410 mm^2 Perkin Elmer XRD1621 detector with a pixel size of 200×200 μm^2 (P21.1) and a 2D 432×432 mm^2 Varex Imaging XRD 4343RF detector with a pixel size of

Table 3.8: Experimental parameters concerning XRD at P07.

Experimental parameter XRD settings	Beamline P07 March 2021
Beam shape by soller slits	0.5 x 0.5
Energy [keV]	101.6
Wavelength [Å]	0.1220
Monochromator	Si(111)
XRD detector[mm^2]	2D 432 x 432 Varex Imaging XRD 4343RF detector
Pixel size [μm]	150 x 150
Calibrant	CeO_2
Sample to detector distance [mm]	1170

150×150 m^2. The large area detectors accessed a large q-space at once and have a large sensitive area of millions of pixels with high spatial resolution. Process automation for running the entire experiment fully automized was successfully implemented, utilizing the reactor control system to trigger an automated XRD measurement script, in which recording dark and sample images, exposure times, and repetitions were defined. In this way, at each sample position within the catalyst bed, first, a dark image was recorded, and afterward 15 sample images with an exposure time of 60 s each. The 15 sample images were averaged for further analysis. The calibration of the sample to detector distances was performed using LaB_6 (P21.1) and CeO_2 (P07) as standards, giving 1255 mm (P21.1) and 1170 mm (P07). XRD data evaluation is described in Subsection 3.6.5.

Furthermore, in addition to the profile runs obtained at P07 in steady-state (1_SS, 2-SSR), two individual profiles (3_PP, 5_PP) and one replicate profile each (2_SSR, 4_PPR, 6_PPR) were measured at periodic reactor operation, using a sinusoidal inlet feed of either oxygen or ethane. The numbers in the profile run from 1 to 6 denote the sequence in which the profiles were recorded within the total measurement time of 28 h. In order to analyze periodic reactor operation in terms of catalyst performance and structure, fast data acquisition was required. Thus, time-resolved XRD analysis was used, recording 180 diffractograms with a short exposure time of 1 s each. The time-resolved XRD patterns measured in periodic reactor operation were averaged for each position. In this work, the

Table 3.9: Experimental parameters concerning XRD at P21.1.

Experimental parameter XRD settings	Beamline P21.1 August 2021
Beam shape by soller slits	0.8 x 0.8
Energy [keV]	103.6
Wavelength [Å]	0.1199
Monochromator	Si(111)
XRD detector [mm^2]	2D 410 x 410 Perkin Elmer XRD 1621 detector
Pixel size [μm]	200 x 200
Calibrant	LaB$_6$
Sample to detector distance [mm]	1255

focus is on steady state reaction conditions. Hence, no further information on periodic experiments are provided and for more details, the reader is referred to [131]. However, to verify beamline stability and reproducibility of the profile methodology, as well as catalyst structure with long times on stream, patterns measured at positions -10, -2, 0 and 16 mm are compared in the Subsection 6.2.1.

3.6.4 Gas Analysis via MS and GC

P07 profile measurements were conducted in two reactor operation modes, steady state and periodic, during a two days in-house beamtime. In order to analyze gaseous species in both reactor operation modes, as well as to focus on coupling the CPR with XRD in the given time, fast data acquisition was required. Goal of the gas analysis during this beamtime was to ensure overall catalytic performance as expected, as well as to correlate the IP with the onset of structural changes in the catalyst. For this purpose, only qualitative MS gas analysis was carried out, utilizing the same Hiden HPR 20 MS and masses scanned as for the catalytic performance study (Subsection 3.3.2).

Quantitative gas analysis using a GC (Agilent 7890B) was performed in the second beamtime at P21.1 with the goal to correlate precisely local gas compositions with the catalyst structure along the entire catalyst bed. The GC used in this study was equipped with two columns for compound separation. The first column was a Plot Q column with a bonded divinylbenzene stationary phase, applied for separating hydrocarbons, carbon oxides, air and water. The second column was a zeolite molecular sieve column called Molsieve that allowed to separate air in nitrogen and oxygen. For species detection a TCD connected in series with a FID were utilized. A corresponding valve system diagram is attached (Fig. A.3). Nitrogen was used as internal standard. Since the reaction mixture was composed of 80 vol.% nitrogen, the accuracy by evaluating peak areas of known gas mixtures referenced to nitrogen was verified in preliminary tests. Other internal standards were not suitable in the installed GC configuration, as helium was used as carrier gas and argon had the same retention time as oxygen (peak overlap). Since hydrogen has a very similar thermal conductivity as helium, it could not be detected and was calculated from the H-atom species balance of the reaction mixture. Water was calibrated using a one-point calibration obtained from the O-atom species balance. By using this methodology, the carbon balance was closed with average deviations of 2 % under oxidative and of 5 % under non-oxidative conditions. The quantification of gaseous species is described in Section 3.7.

3.6.5 XRD Data Analysis

XRD data were acquired with large 2D area detectors, which enabled to record Debye-Scherrer rings in the q range of 1.3 – 11 Å^{-1} at once within exposure times of seconds. In the used automated XRD measurement scripts, first, a dark image was recorded, and afterward a defined number of sample images (Subsection 3.6.3). After dark-current subtraction and flat-field correction, the obtained XRD images were transformed in XRD curves using pyFai [132]. An overview of the data processing steps in pyFai is illustrated in Figure 3.16.

As a first step a .mask and Point Of Normal Incidence (.poni) files were created via pyfai-calib2, implemented as calibration tool in pyFAI (Figure 3.16a). In the mask file outlier pixels, e.g., resulting from dead pixels or non-sample related scattering such as the beam stop shadow, were defined. The .poni file contained the geometry of the experimental setup, including six refinement parameters (dist, Poni 1, Poni 2, rot1, rot2, rot3), as well as specifications on the applied detector and energy. The refinement parameters describe the position in space of the area-

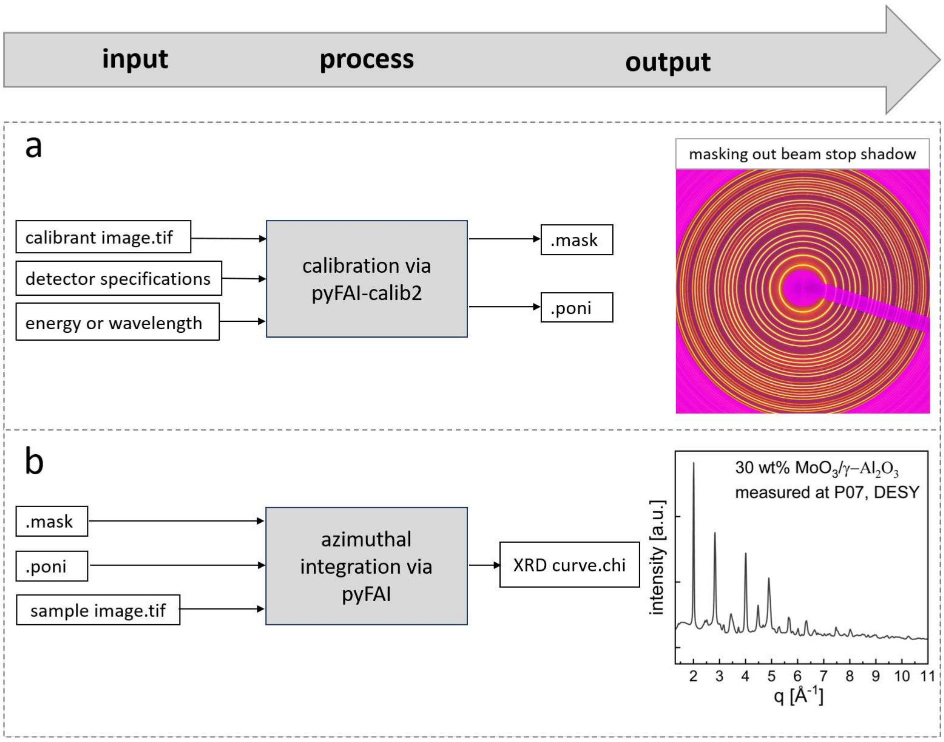

Figure 3.16: Overview of XRD data processing steps in pyFai prior to phase composition analysis.

detector through the defined positions of the sample and the incident X-ray beam. In transmission mode, the incident beam should be orthogonal to the surface of the detector, which is the case if all rotations are zero. For this purpose, the diffraction setup geometry was calibrated using the Debye-Scherrer rings of LaB_6 (P21.1) or CeO_2 (P07) as standards. Notably, standard materials were filled in equal reactor tubes as in the respective profile measurement and measured in the same setup configuration. Next, in order to convert the XRD images, azimuthal integration was performed in pyFAI (Figure 3.16b). Here, X-ray intensities along each Debye-Scherrer ring were averaged. The .mask and .poni file were applied consistently across all images. An overview of the input and output information, according to the description in Figure 3.16, is given in Table 3.10.

For qualitative phase analysis HighScore Plus software [133] and the ICDD database were used.

Table 3.10: Input and output information using pyFAI for XRD data processing.

Experimental parameter	Beamline P07 March 2021	Beamline P21.1 August 2021
Detector type	Varex Imaging XRD 434RF	2D Perkin Elmer XRD1621
Array size	150 x 150 μm^2	200 x 200 μm^2
Pixel size	2048 x 2048	2048 x 2048
Energy [keV]	103.6	101.6
Wavelength [Å]	0.1199	0.1220
Calibrant	CeO_2	LaB_6
Poni 1	0.2252	0.2097
Poni 2	0.2190	0.1901
Rot 1	-0.0037	-0.0121
Rot 2	-0.0034	-0.0035
Rot 3	0	0
Distance [mm]	1170	1255

An example of structure refinement was performed for patterns recorded in the absence of gas phase oxygen using the FullProf software based on the MoO_2 oxide structure (ICSD collection code 23722) [134]. It should be clarified that the refinement was performed by Ida Nielsen at DESY.

3.7 Target Variables from Gas Analysis

The purpose of gas analysis, whether using MS or GC, was to determine gas compositions qualitatively and, if necessary, quantitatively. From quantitative gas analysis, catalyst performance was evaluated in terms of conversion and selectivity (target variables), which is described in this section. In order to achieve the target variables, measured peak signals were first clearly assigned to a certain component (qualitative gas analysis) and subsequently calibrated (quantitative gas analysis). In GC measurements, components are identified based on peak retention times, while in MS measurements peaks of the target components are obtained at their corresponding m/z ratios. Noteworthy, since most components have a characteristic fragmentation pattern in a MS spectrum, i.e., signals occur at several masses, non-overlapping, intense signals with respect to other components in the reaction mixture were the preferred choice for easy quantification and required for the internal standard. The same applies for GC analysis, but was considered during GC method development, where retention times of all components were adjusted (mainly by varying column temperatures) to have no peak overlap. Peak analysis for quantification differed slightly for MS and GC, whereas the actual calibration procedure, following the internal standard method, was very similar. Peak areas were evaluated in GC chromatograms and peak heights in MS spectra. Based on peak areas or peak intensities, a known gas mixture, consisting of an inert (internal standard) and a species (calibrant), was dosed to the device. Subsequently, the signals were measured and area (GC) or intensity (MS) ratios were calculated. In this way, volumetric flow rates were obtained for GC:

$$\frac{A_c}{A_{IS}} = \frac{a_c \cdot \dot{V}_c}{\dot{V}_{IS}} \tag{3.10}$$

and for MS:

$$\frac{I_c}{I_{IS}} = \frac{a_c \cdot \dot{V}_c}{\dot{V}_{IS}} \tag{3.11}$$

Where A_c represents the peak area of the component c and A_{IS} of the internal standard, a_c is the calibration slope, $\dot{V}_c$ and $\dot{V}_{IS}$ are the volumetric flow rates of component c and internal standard, respectively. Analogous to this, I_c represents the signal intensity of the component c and so on. By alternating the calibrant concentration (minimum of seven concentrations) a calibration curve was recorded. This procedure was repeated for all species of interest in the reaction mixture. From the obtained slopes unknown concentrations in a sample stream were determined. By using the ideal gas law volumetric flow rates were converted into molar flow rates.

In order to evaluate overlapping peak heights of involved components in the reaction mixture via MS, caused by the above-mentioned fragmentation pattern of each component, one additional step (signal correction) was required in comparison to GC analysis. For this, first, the signal contribution of the fragment at the analyzed m/z ratio $\mathrm{I}_{c,m/z}$ was calculated according to:

$$I_{c,m/z} = \frac{a^c_{m/z}}{a^c_{main}} I^c_{main} \tag{3.12}$$

Where $a^c_{m/z}$ gives the slope of the calibration curve of the fragment, a^c_{main} is the slope of the calibration curve at the main peak of the component, and I^c_{main} is the pure signal intensity of the component *c* at the components main peak. Subsequently, the contribution of all fragments $I_{c,m/z}$ was substracted from the measured total signal intensity $I_{m/z}$ to yield the corrected signal intensity of the target component.

Components that could not be measured with a certain gas analytic, e.g., water, CO (micro-GC) or H_2 (GC 7890B), were calculated from the atomic species balance (H, C, O) of the reaction mixture according to Eq. 3.13, where $\dot{n}_{A,in}$ is the inlet molecular flow and $\dot{n}_A$ is the molecular flow at the actual bed position of atoms *A* (C_2H_6; O_2).

$$\sum \dot{n}_{A,in} - \sum \dot{n}_A = 0 \tag{3.13}$$

In the same way, atom balance closures were checked for all profile runs, having average deviations in the range of 5 -10 %.

Finally, based on the previous steps, the target variables were calculated from molecular flow rates. Conversion was determined of the feed components *i* (C_2H_6; O_2) between the molar flow rate $\dot{n}_{i,in}$ entering the reactor bed and at the actual bed position $\dot{n}_i$ according to Eq. 3.14.

$$X_i(\%) = \frac{\dot{n}_{i,in} - \dot{n}_i}{\dot{n}_{i,in}} \cdot 100 \tag{3.14}$$

Selectivities of by-products *P* (C_2H_4; CO; CO_2, CH_4) were determined using Eq. 3.15.

$$S_P(\%) = \frac{\dot{n}_P - \dot{n}_{P,in} \cdot |v_i|}{\dot{n}_{i,in} - \dot{n}_i \cdot v_k} \cdot 100 \tag{3.15}$$

4 Species Concentration and Temperature Profiles

The aim of this thesis is the development of new *operando* profile measurement concepts to study structure-activity relationships of various catalytic reaction systems under realistic operation conditions. For this purpose, a rather simple reaction system, namely ethane ODH over a 30 wt% $MoO_3/\gamma\text{-}Al_2O_3$ catalyst, was intentionally chosen as a test system for systematic method development. In a first step toward this goal of operating reliably new *operando* profile experiments, a set of concentration and temperature profiles was performed, decoupled from the catalyst characterization technique. This approach reduces experimental complexity at the beginning. In this way it is possible to ensure reliable operation of the profile measurement technique and reactor system as well as to gain experience with the reaction system. Results obtained from these concentration and temperature profiles experiments are presented in this chapter. Firstly, a brief overview of the ODH reaction system, involving a qualitative description of ongoing gas phase reactions in the presence and absence of gas phase oxygen is given. This section is part of an article submitted to the Journal of Synchrotron Radiation [125]. Secondly, effects of feed and temperature variations on catalyst performance are analyzed, considering catalyst behavior in the presence of gas phase oxygen. The obtained species and temperature profiles were used to significantly speed up the development and accuracy of kinetic models required for any reactor design by fitting complete reactor profiles, which is the content of the last section. These last two parts, Section 4.2 and Section 4.3, have been conducted by Diego Espinoza and firstly published in his master thesis [135], as well as in [126].

4.1 Overview Ethane ODH Reaction System

Figure 4.1 shows a picture of the catalyst bed (top) with the inlet flow ($F_{i,in}$) from left to right, as well as an overview of the activity profiles obtained within one profile run during ethane ODH over a 30 wt% MoO_3/γ-Al_2O_3 catalyst.

The profile measurement effectively allows for discrimination between the different gaseous reactants and products and their concentrations at each internal position of the catalyst bed. Species concentration profiles of C_2H_6, O_2, CO, H_2O (Fig. 4.1a), C_2H_4, H_2, CO_2 and CH_4 (Fig. 4.1b) are shown in molar flow rates, and corresponding conversion (Fig. 4.1e), and selectivity (Fig. 4.1f) profiles in percent. Enlarged views of H_2O, CO (Fig. 4.1c), CO_2 and CH_4 (Fig. 4.1d) profiles are illustrated to emphasize characteristic profile shapes before and after the point of full gas phase oxygen conversion. The latter matches with the position of the IP (α, 18 mm), and is further referred to as well. The catalyst bed begins at position 0 and ends at position 30 mm, marked with black lines and illustrated by the corresponding pictures of the catalyst bed. Notably, precise calibration of the reaction system is observable in Fig. 4.1a by almost equimolar inlet compositions (C_2H_6:O_2 = 1:1). In the regions upstream (-7 – -5 mm) and downstream (31 – 34 mm) of the catalyst bed only minor changes in educt consumption or product formation (Fig. 4.1a,b) are visible (flat profiles), while steep gradients are evident along the catalyst bed (1 – 30 mm), confirming that ethane ODH only occurs in the presence of the catalyst at the chosen reaction conditions. Close to position 0 mm (-4, -3, -2, -1), small changes are observable due to a mixed zone between QW and catalyst, resulting from bed packing (likewise at 30 mm), as well as diffusional effects. The latter has a stronger influence on profile shapes of lighter molecules as H_2, which is discussed in more detail later in this section.

Measurements performed behind the catalyst bed (positions > 30 mm) are equivalent to the information obtained by conventional integral reactor analysis (reactor outlet measurements). However, gas concentration and temperature information within the reaction zone (0 – 30 mm) are not accessible using integral reactor analysis. In contrast, by using the demonstrated capillary sampling technique, differential gas and temperature measurements through the catalyst bed (within the range of the black lines) could be acquired. This allows following a broad con-

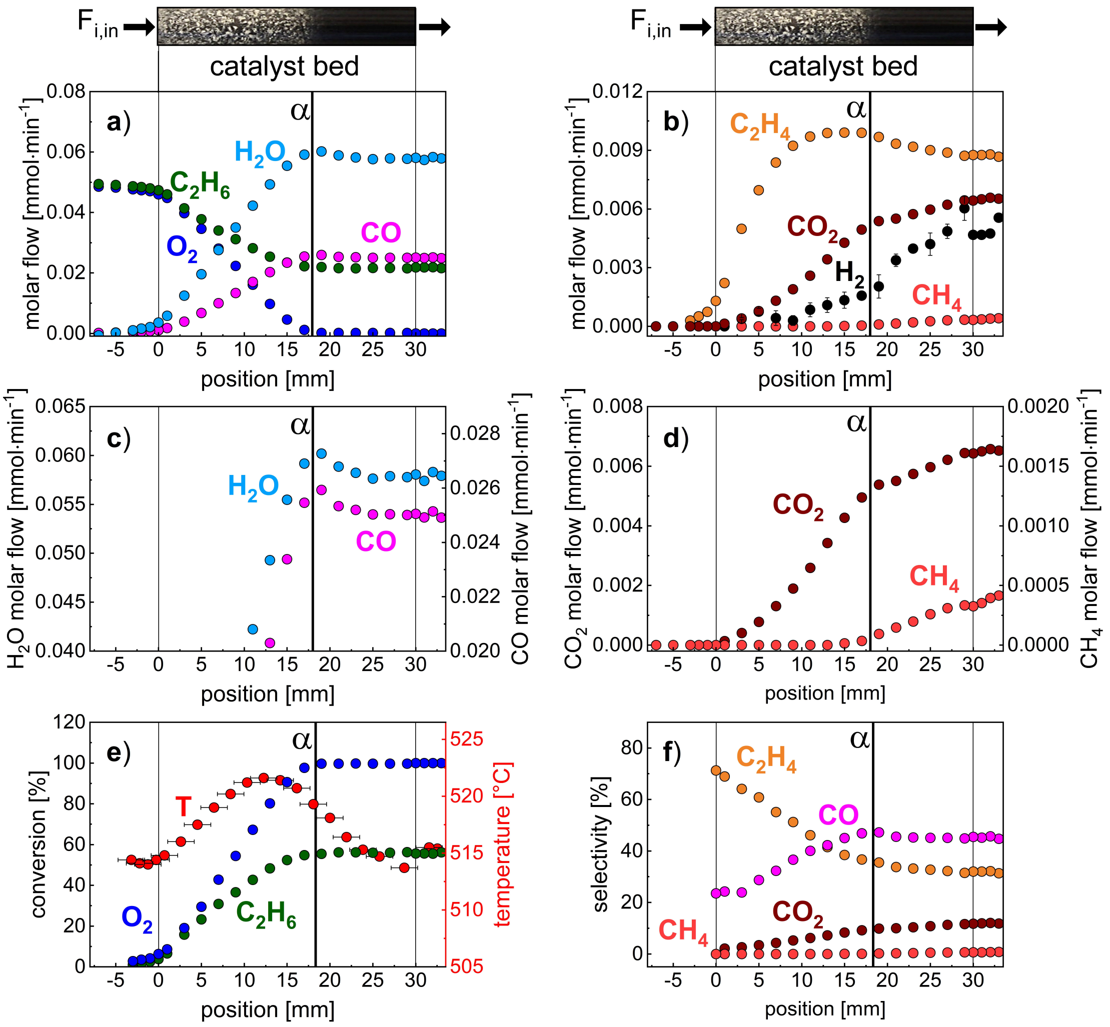

Figure 4.1: A picture of the catalyst bed (top) with the inlet molar flow rate of each species ($F_{i,in}$) and corresponding catalyst activity profiles (a – f). Species concentration profiles of C_2H_6, O_2 (a), H_2O, CO (a, c), C_2H_4, H_2 (b) CO_2, CH_4 (b, d); conversion profiles of C_2H_6 and O_2 (e); selectivity profiles of C_2H_4, CO, CH_4, CO_2 (f); and the temperature profile measured in the center of the catalyst bed (e). α (black line, 18 mm) marks the position of full gas phase oxygen conversion with different catalyst performance before and after. Reaction conditions: $C_2H_6/O_2/N_2$:10/10/80, 515 °C, 1 bar, OD 6 mm/ID 5.0 mm, 30 mm catalyst bed, 12 ml/min, 30 wt% $MoO_3/\gamma\text{-}Al_2O_3$. The catalyst activity profiles were simultaneously measured with XRD (see Chapter 6).

version range of C_2H_6 (0 – 50%) and O_2 (0 – 100%) within one profile measurement (Fig. 4.1a). A combination of local sampling and reactor outlet measurements (differential and integral analysis) is particularly favorable during long profile runs to ensure an overall stable catalytic performance (e.g., catalyst deactivation) of less well-known reaction systems.

By evaluating the course of entire species profiles within the reaction zone, rapid identification of ongoing reactions and pathways can be obtained. As an example, the used catalyst system can be distinguished in two reaction regimes, before and after position 18 mm, illustrated with a black line and denoted as α. The latter corresponds to the point of full gas phase oxygen conversion (Fig 4.1e) and IP from grey to dark blue/black of the catalyst (picture of the catalyst bed, Fig. 4.1, top). In the presence of gas phase oxygen (0 – 18 mm) ODH (Eq. 4.1) and oxidation reactions (Eq. 4.2 – 4.5) are predominant. O_2 and C_2H_6 are readily consumed (Fig. 4.1a,e), while mainly CO and H_2O (Fig. 4.1a), as well as small amounts of C_2H_4 and CO_2 (Fig. 4.1b), are formed.

$$C_2H_6 + 0.5\,O_2 \longleftrightarrow C_2H_4 + H_2O \qquad \Delta H^0_{298\text{ K}} = -105\ \frac{\text{kJ}}{\text{mol}} \tag{4.1}$$

$$C_2H_6 + 5\,O_2 \longleftrightarrow 3\,CO + 2\,H_2O \qquad \Delta H^0_{298\text{ K}} = -731\ \frac{\text{kJ}}{\text{mol}} \tag{4.2}$$

$$C_2H_6 + 7\,O_2 \longleftrightarrow 2\,CO_2 + 3\,H_2O \qquad \Delta H^0_{298\text{ K}} = -1428\ \frac{\text{kJ}}{\text{mol}} \tag{4.3}$$

$$C_2H_4 + 4\,O_2 \longleftrightarrow 2\,CO + 2\,H_2O \qquad \Delta H^0_{298\text{ K}} = -757\ \frac{\text{kJ}}{\text{mol}} \tag{4.4}$$

$$C_2H_4 + 6\,O_2 \longleftrightarrow 2\,CO_2 + 2\,H_2O \qquad \Delta H^0_{298\text{ K}} = -1323\ \frac{\text{kJ}}{\text{mol}} \tag{4.5}$$

The product selectivity profile of ethylene (Fig. 4.1f) decreases with an increase in ethane conversion (along the catalyst bed, (Fig. 4.1e)) while selectivity towards the undesired carbon oxides CO and CO_2 increases. These profile shapes are as expected since the direct oxidation of ethane or further oxidation of ethylene is likely to occur, both reducing ethylene selectivity at higher ethane conversion levels.

By evaluating initial formation rates (initial profile slopes $\mathrm{m_{IPS}}$) of C_2H_4, CO and CO_2 at the very beginning of the catalyst bed from -3 to 1 mm, information of primary (C_2H_4, $\mathrm{COm_{IPS}} > 0$) and secondary ($\mathrm{CO_2{,}m_{IPS}} \approx 0$) products are obtained.

In addition to C_2H_4 and CO_2, hydrogen occurs in minor quantities in the oxidation zone (Fig. 4.1b), viz. upstream of point α, where gas phase oxygen is still present. As discussed below, H_2 is chemically produced downstream of α and diffuses rapidly against the flow direction. H_2 is a lightweight molecule and because the diffusion coefficient of a molecule scales with the square root of one over the molecular weight, hydrogen diffuses more than three times faster than all other components present in the reaction mixture. At the applied low total flow rate inside the catalyst bed, the reactor Péclet number of H_2 is as low as about ten, taking the bed length as a characteristic dimension. In fixed bed reactors, a low reactor Péclet number indicates that axial dispersion cannot be neglected compared to convection resulting in considerable back mixing. Even though the H_2 concentration profile shown in Fig. 4.1b was calculated from the H-atom species balance and sums up measurement errors from all other species, the effect that hydrogen diffuses upstream of the point α was also confirmed experimentally, shown later in this work (see Subsection 5.2.1). In agreement with the calculated profile in Fig. 4.1b, the measured profiles show an increase in H_2 flow rate way upstream the point of complete O_2 conversion and a distinct increase in slope beyond that point. Close inspection of the photograph of the catalyst bed displayed on top of each flow rate panel in Fig. 4.1 shows a faint darkening of the catalyst bed from the point where H_2 is first detected in the catalyst bed until the IP α where the catalyst turns dark violet, almost black. In this second reaction zone (18 – 30 mm, downstream of α) the overall reaction mechanism changes. In the absence of gas phase oxygen ODH and oxidation reactions stop. As seen by the formation of a new species CH_4 (Fig. 4.1b,d), an increasing slope of the H_2 profile (Fig. 4.1b), continued CO_2 formation (Fig. 4.1b, d) and the occurrence of maxima in the profiles of C_2H_4 (Fig. 4.1b), H_2O and CO (Fig. 4.1c), the chemistry in the oxygen-free zone of the catalyst bed is entirely different from the zone in which gas phase oxygen was present. The fact that C_2H_4, H_2O and CO pass each through a maximum close to point α is because these species are formed upstream of α and consumed downstream of α. The species profile shapes are the result of several, overlapping reactions that, in combination, can explain the observed trends. The profiles provide evidence that Water-Gas Shift Reaction (WGSR) (Eq. 4.6) occurs.

$$CO + H_2O \longleftrightarrow CO_2 + H_2 \quad \Delta H^0_{298\ K} = -41\ \frac{kJ}{mol} \tag{4.6}$$

CO_2 is the only carbon species increasing towards the end of the catalyst bed (Fig. 4.1b, d) with a smaller formation rate in comparison to the first reaction zone, further indicating a different formation reaction. In addition, H_2 is formed (Fig. 4.1b) while CO and H_2O are decreasing with a sharp onset at 18 mm (Fig. 4.1c).

Another reaction taking place in the oxygen-free zone of the catalyst bed is most likely ethylene steam reforming, indicated by the decreasing C_2H_4 molar flow rate combined with profile shapes of H_2O, H_2 and CO (Eq. 4.7).

$$2\,H_2O + C_2H_4 \longleftrightarrow 4\,H_2 + 2\,CO \quad \Delta H^0_{298\ K} = 210\ \frac{kJ}{mol} \tag{4.7}$$

Finally, at position α methane production is observable, which suggests that CO or CO_2 methanation (Eq. 4.8 – 4.9) start as soon as H_2 is formed.

$$CO + 3\,H_2 \longleftrightarrow CH_4 + H_2O \qquad \Delta H^0_{298\ K} = -206\ \frac{kJ}{mol} \tag{4.8}$$

$$CO_2 + 4\,H_2 \longleftrightarrow CH_4 + 2\,H_2O \qquad \Delta H^0_{298\ K} = -165\ \frac{kJ}{mol} \tag{4.9}$$

The spatially-resolved carbon balance closure evaluated over the entire reaction zone (0 – 30 mm) demonstrates an upward trend from 0 to 6 %, indicating the occurrence of additional minor side reactions, resulting in unidentified gas species or C deposits. The latter might originate from CO (Boudouard reaction) (Eq. 4.10) or C_2H_4 (Eq. 4.11).

$$2\,CO \longrightarrow C + CO_2 \qquad \Delta H^0_{298\ K} = -173\ \frac{kJ}{mol} \tag{4.10}$$

$$C_2H_4 \longrightarrow 2\,H_2 + 2\,C \qquad \Delta H^0_{298\ K} = -52\ \frac{kJ}{mol} \tag{4.11}$$

With regard to the temperature profile (Fig. 4.1e), the profile measurement was conducted at 515 °C, which corresponds to the temperature measured in the center and upstream of the catalyst bed. The temperature rises slightly within the catalyst bed with a maximum value of 522 °C around , confirming exothermic oxidation reactions taking place (Eq. 4.1 – 4.5).

In conclusion, measurements performed under ethane ODH conditions over MoO_3/γ-Al_2O_3 have common characteristics and compare well with all spatial concentration profiles performed in this work as well as with a spatial profile study described in literature [22]. The combined local temperature and gas phase analysis demonstrate their potential through a high information content over a wide conversion range within one single profile run. The spatial profile results reveal a change in catalyst activity at the point of full gas phase oxygen conversion (α) from reactions involving gas phase oxygen to steam reforming and WGS. The results allowed to propose a first reaction mechanism, considering the change in catalyst activity at α, based on identified species as well as on respective consumption and formation rates. However, one experimental profile provides only a superficial understanding of the reaction network. To illustrate this point, it cannot be concluded if either C_2H_6 or C_2H_4 is the main contributor toward the undesired CO_x production, or if CO_2 is produced in a consecutive reaction from CO. In order to gain a deeper understanding of the reaction system, additional concentration and temperature profile measurements were performed under various reaction conditions, which are the focus of the next Section. Furthermore, the change in catalyst performance is in line with the change in color that indicates the reduction of MoO_3 to MoO_2, which in turn creates a different phase composition with different catalytic properties. As example, MoO_2 has metallic properties. According to literature, MoO_2 is suitable to catalyze steam reforming [136] and WGSR [137]. This is in agreement to our species profile observations described above. *Operando* measurements are required to unravel structural changes around α, which is the focus of Chapter 5 and Chapter 6.

4.2 Catalyst Activity Investigation

This section presents the results obtained from the catalyst activity tests (Section 3.3). First, stable catalytic performance as well as stable and reproducible operation of the profile reactor and the profile measurement technique are addressed by comparing original and corresponding replicate profiles from the experimental design plans. In the next two subsections, the influence of reactant concentration as well as reaction temperature on catalyst performance are analyzed. Notably, the profile measurements presented in this section are performed with maximum oxygen conversion levels of 60 %.

4.2.1 Stability and Reproducibility Tests

In all experimental design plans replicate runs were evenly distributed throughout the measurement plan. The first experimental design plan comprises eight profiles (P1 – P8) and two replicates (R1, R8). In between the original profile and its replicate was approximately a measurement time of 40 h. The second experimental part consists of two experimental design plans, one feeding ethane and the other one ethylene, with four replicates each. Both design plans were consecutively performed with in total 26 profiles over a measurement time of ten days. Results across all design plans compare well with each other in terms of catalyst stability and reproducibility, which is the focus in this subsection. Thus, results obtained from the replicate runs in the first design plan are presented exemplary, while results from the replicate profile runs in the second experimental part are shown in the supplementary material (Figure A.4, Figure A.5).

The profile (P8) and its replicate (R8) at 530 °C are displayed for all components in Figure 4.2.

The catalyst bed position is illustrated with black lines (0 – 30 mm). The feed components C_2H_6 and O_2 (Fig. 4.2a), the main products ethylene and water (Fig. 4.2b), as well as the undesired carbon oxides CO (Fig. 4.2c) and CO_2 (Fig. 4.2d) show a good match between replicates and original data. Minor deviations are observable in CO that contains mass contributions from C_2H_6, C_2H_4 and CO_2 in quantification with MS. H_2O was the only species calculated from mass balance. The replicate experiments allow to deduce stable catalyst performance through various reaction conditions in the measurement campaign. Additionally, they demonstrate stable and reproducible operation of the spatial profile reactor (precise positioning, heating) and of the profile measurement technique. Thus, strong impacts on catalytic performance by strongly varying sampling flow rates

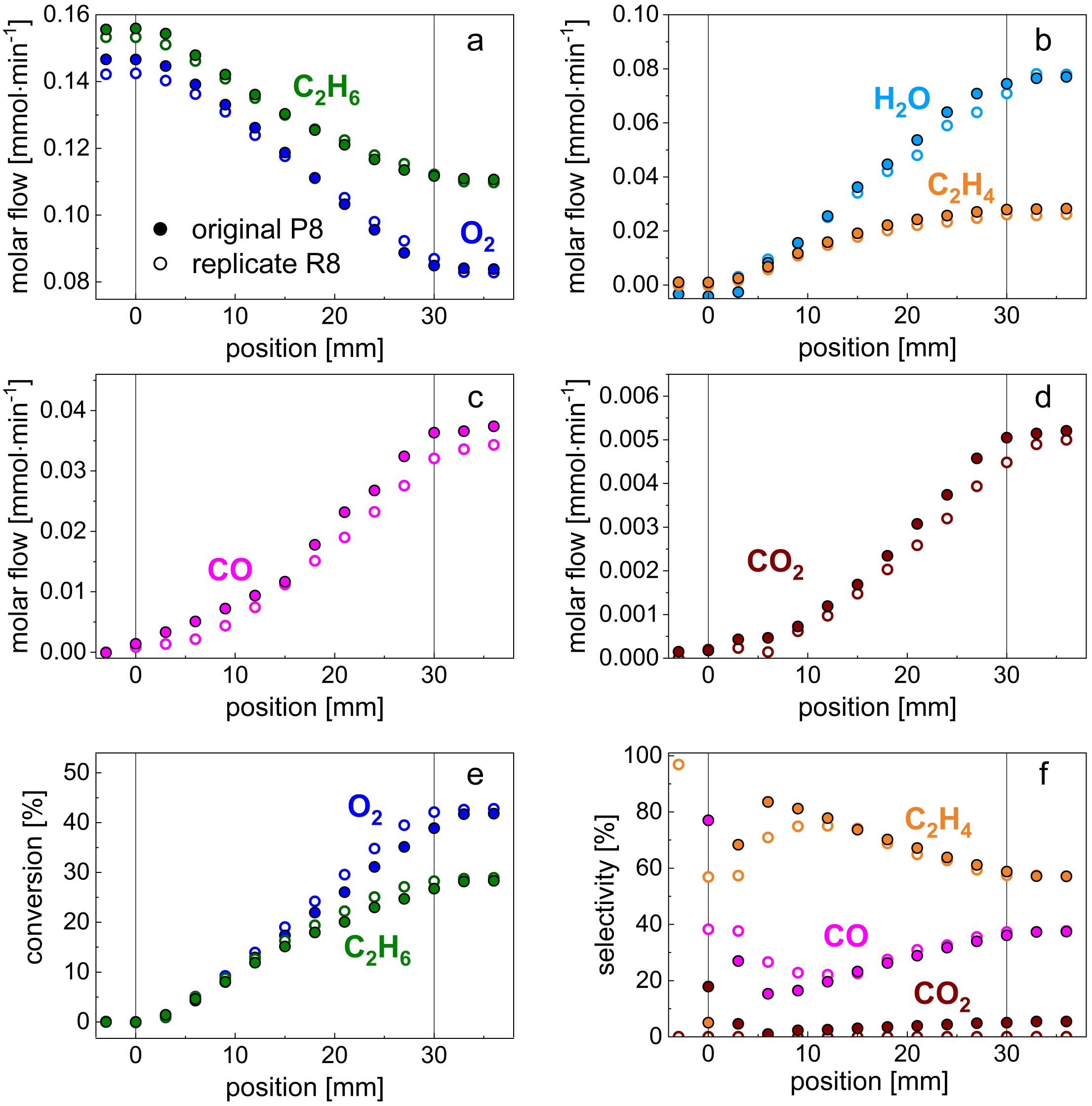

Figure 4.2: Profile runs measured in the 1st measurement design plan are shown of the original profile (P8) and its replicate (R8) measured at the central point. a-d) Profiles of all species in molar flow rates; e) Conversion profiles of C_2H_6 and O_2; e) Selectivity profiles of C_2H_4 and CO_x. Reaction conditions: C_2H_6:O_2=12.5:12.5, 530 °C, 1 bar, 30 mm catalyst bed, 30 ml/min, 30 wt% $MoO_3/\gamma\text{-}Al_2O_3$.

or on the catalyst bed by repetitive moving of the sampling capillary through the catalyst bed can be excluded. For example, the latter could have led to changes in the catalyst particle size by crushing catalyst particles. As a result smaller particles could block the sampling orifice resulting in variations of sampled gas amounts which in turn disturb hydrodynamic conditions of the reactor. Further, smaller particles compact the bed leading to different catalyst mass per sample position. The aforementioned effects have strong impacts on profile shape and would be clearly observable if they had occurred.

MS analytical deviations at low conversion levels ($< 5\%$) disturb the shape of the selectivity profiles in the very beginning of the catalyst Fig. (4.2f). For example, the ethylene profile shows a maximum at position 6 mm, which is an analytical artifact. At early bed positions, the molecular flow of reactants tends to zero, therefore minor deviations of these values lead to a large impact on selectivity. In the same way, selectivity profiles of CO and CO_2 are affected. The parameter field of C_2H_6 and O_2 inlet concentrations with 7.5 and 12.5 %, respectively, were in a good range to separate conversion profiles clearly from each other. Temperature studies revealed that further tests should not be performed below 480 °C since conversion levels of C_2H_6 and O_2 less than 10% were obtained. The results of P1 and its replicate R1 at 480 °C are shown in supplementary information (Figure A.6). In addition, precise calibration of the reaction system is observable by almost equimolar inlet compositions.

The impact of conversion on temperature is well seen by comparing temperature profiles measured upon feeding ethane or ethylene. Therefore, temperature profiles obtained in the two design plans of the second experimental part are shown in Figure 4.3. The corresponding replicate runs are indicated by error bars.

Temperature replicates show a good match with minor deviations in the range of 1 °C indicated by error bars. The experimental set temperature assigned to both experiments was 530 °C. The measured temperature in the capillary in the center of the catalyst bed is about 10 °C lower (0 mm) than the set temperature. Depending on the degree of conversion and involved reactions, the temperature raises slightly within the catalyst bed. Temperature raises are below 5 °C feeding C_2H_6 or below 10 °C feeding C_2H_4 and hence, fair isothermality is observed. Temperature profiles obtained at different temperature levels are presented in Subsection 4.2.3.

Overall, profile results demonstrate that the profile reactor setup and the profile measurement technique is capable of producing meaningful results. Furthermore, stable catalytic performance over rather long time periods was ensured, which is

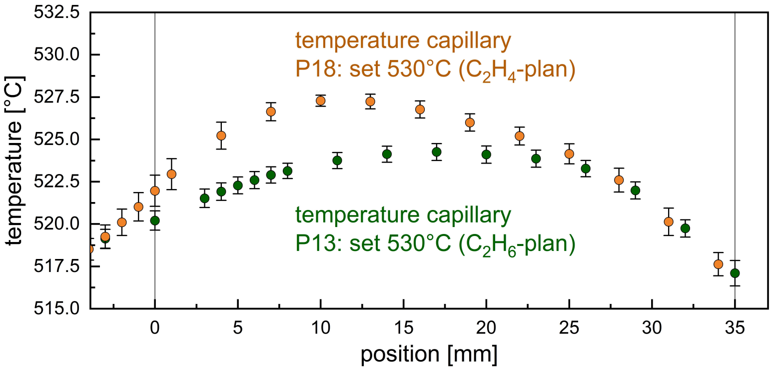

Figure 4.3: (a) Averaged temperature profiles of the central point for the C_2H_6 (P13) and C_2H_4 (P18) measurement plan. Error bars are derived from the replicates by calculating the standard error. Reaction conditions: 530 °C, C_2H_6/O_2/inert:10/10/80; C_2H_4/O_2:5/10, 1 bar, 32 mm catalyst bed, 30 ml/min (C_2H_6-plan), 40 ml/min (C_2H_4-plan), 30 wt% $MoO_3/\gamma\text{-}Al_2O_3$.

essential for spatial profiling in general, and the basis for all experiments in this work.

4.2.2 Variation in Feed Concentrations

In order to test for feed effects ethane, ethylene and oxygen were varied in the second experimental part on three concentration levels using two face centered central composite design plans, one for each hydrocarbon (Section 3.3). Each concentration level represents one individual profile run.

Figure 4.4 shows an overview of the profile runs in the second measurement plan performed with variation in O_2 (1^{st} row) and C_2H_6 (2^{nd} row) from 7.5 to 12.5 % for each species.

Apparently, no effect of O_2 feed variations on C_2H_6 consumption (a) or C_2H_4 production (c) are observable. These observations indicate that C_2H_6 consumption rate has a low reaction order with respect to O_2 concentration. Thus, processes related to oxygen can be considered as fast. When looking at species concentration profiles performed with different C_2H_6 feed compositions (Fig. 4.4, 2^{nd} row), a clear impact on O_2 and C_2H_4 are observed. An increasing C_2H_6 concentration enhances O_2 consumption (e) and olefin formation (f) along the catalytic bed. The increase

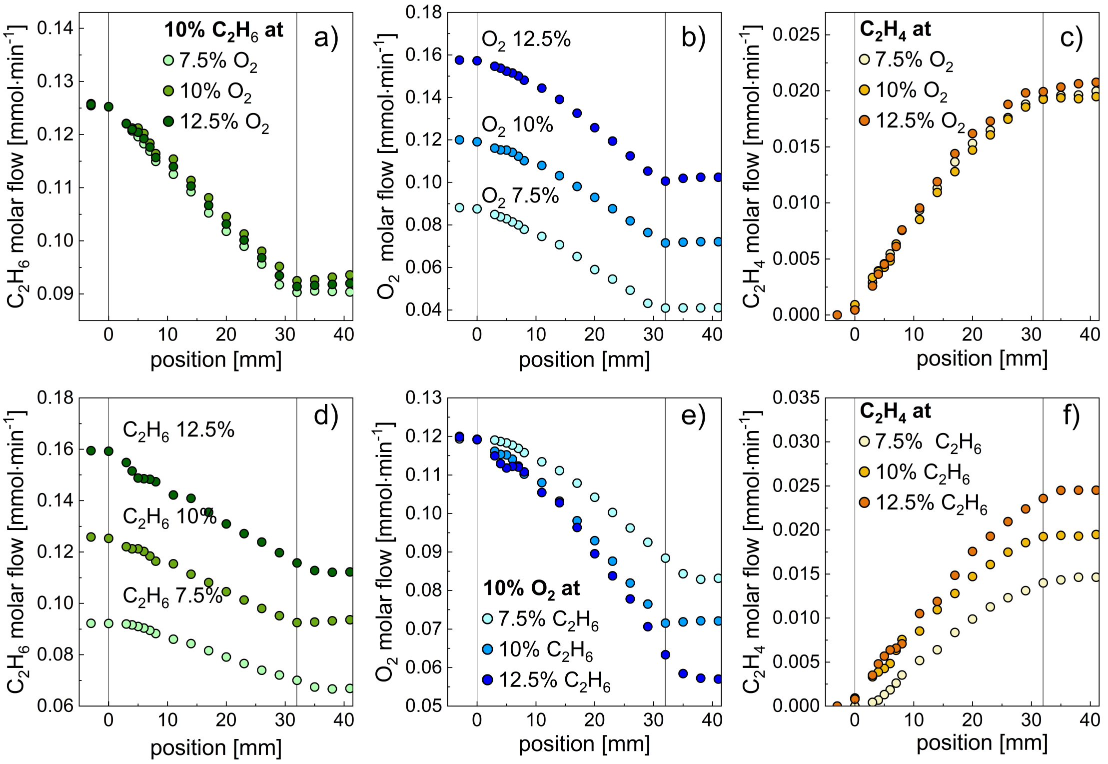

Figure 4.4: Feed variations of O_2 (1^{st} row) and C_2H_6 (2nd row) at reactant concentrations of 7.5, 10 and 12.5 % (P9 – 13). All percentage values are in a molar base. (a,d) C_2H_6; (b,e) O_2; (c,f) C_2H_6 concentration profiles. Reaction conditions: 530 °C, 1 bar, 32 mm catalyst bed, 30 ml/min, 30 wt% $MoO_3/\gamma\text{-}Al_2O_3$.

in O_2 consumption slows down with increasing C_2H_6 concentration as seen by comparing the 7.5, 10 and 12.5 % C_2H_6 profiles in Fig. 4.4e.

Figure 4.5 shows an overview of C_2H_6 (a, d) and O_2 (b, e) conversion profiles as well as C_2H_4, CO, CO_2 selectivity profile runs with variation in O_2 (1^{st} row) and C_2H_6 (2^{nd} row) from 7.5 to 12.5 % for each species. As expected, product selectivity of C_2H_4 within one profile decreases with an increase in ethane consumption (along the catalyst bed), while selectivity towards the undesired carbon oxides CO and CO_2 increases. In response to the applied feed variations, no clear change on selectivity in between the different profile runs is observable.

Similar observations are made varying C_2H_4 and O_2 feed compositions. Changes in oxygen feed composition from 7.5 up to 12.5 % showed no effect over ethylene and CO_x concentration profiles stating that C_2H_4 consumption rate is of low reac-

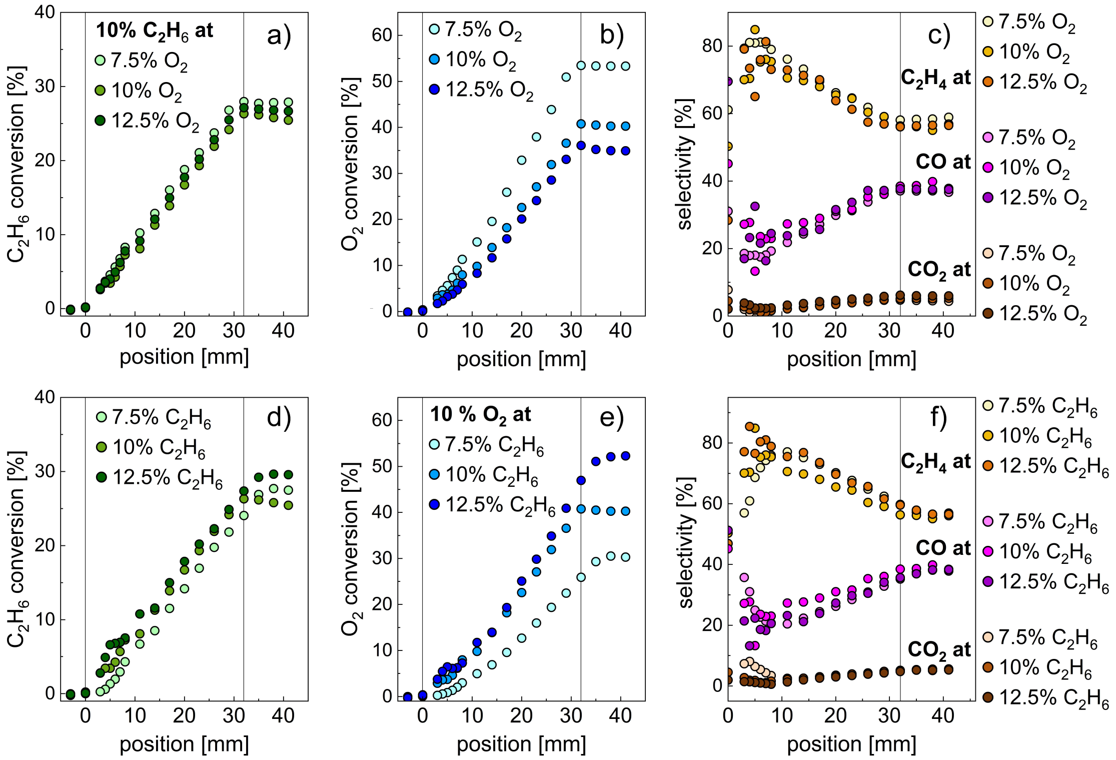

Figure 4.5: Feed variations of O_2 (1^{st} row) and C_2H_6 (2_{nd} row) at reactant concentrations of 7.5, 10 and 12.5 % (P9 – P13). All percentage values are in a molar base. (a,d) C_2H_6; (b,e) O_2 conversion profiles. (c,f) C_2H_4, CO, CO_2 selectivity profiles. 530 °C, 1 bar, 32 mm catalyst bed, 30 ml/min, 30 wt% MoO_3/γ-Al_2O_3.

tion order with respect to O_2 concentration. This result points out to the fact that C_2H_4 side reactions involve a similar mechanism as in the case of ODH of ethane. Whereas an increase in feed C_2H_4 from 2.5 to 7.5 % leads to an increase on its rate of consumption from 34.5 to 45.3 % and oxygen conversion levels from 19.8 to 73.1 %. Ethylene is rapidly and mainly converted to CO resulting in almost unchanged selectivity profiles above 85 %. Again, in response to the applied feed variations of C_2H_4 and O_2, no change on selectivity in between the different profile runs is observable. The previous described results of the C_2H_4 measurement design are shown in supplementary material in Figure A.7 and A.8.

To summarize, spatially-resolved ethane and ethylene concentration profiles reveal a low order kinetic behavior in oxygen, suggesting a similar rate determining step related to ethane or ethylene activation. Furthermore, profile measurements feeding different ethylene concentrations suggest ethylene as main contributor toward carbon oxides production.

4.2.3 Variation in Temperature

In the end of the two measurement campaigns presented in the previous subsection, additionally four profile runs (C_2H_6:O_2 = 10:10) at 480, 500, 520 and 540 °C were performed. In this way, initial values for the activation energy required in kinetic modeling (see Section 4.3) was obtained.

Figure 4.6 and 4.7 present the effect of an increasing reaction temperature on reactant consumption and (by)-product formation. Spatial profiling demonstrates well the expected impact of this variable over the rate of consumption/production of all species. Figure 4.6 shows in molar flow rates, that higher reaction temperatures enhance reactant consumption of C_2H_6 (a) and O_2 (b), while increasing the production of the target compound C_2H_4 (c) as well as side (d) and undesired (e, f) products.

In addition, Figure 4.7 shows the corresponding conversion profiles of C_2H_6 (a) and O_2 (b) as well as selectivity profiles of C_2H_4 (c), CO (d) and CO_2 (e). Selectivity profiles reveal clearly the effect of reaction temperature on product selectivity. Ethylene selectivities decrease strongly with higher temperatures (c), while selectivities of CO_x increase (d, e). As already discussed in Subsection 4.2.1, the shape of selectivity profiles is disturbed in the beginning of the catalyst bed due to an analytical artifact. A linear regression analysis at positions above 10 mm allows to estimate the expected selectivity at zero contact time. By using this methodology, product selectivities of CO, CO_2 and C_2H_4 add up to approximately 100 % at the inlet of the catalyst bed. Furthermore, Figure 4.6f shows the corresponding temperature profiles from 480 – 540 °C.

Similar observations are made in feeding C_2H_4 and varying reaction temperatures (Figure A.9). As described previously in Subsection 4.2.2, CO is produced with selectivities higher than 85 %. Reaction temperature shows only minor effect on changing reaction rates towards CO_2 (Figure A.10).

In conclusion, 26 profiles were measured under well-defined and various reaction conditions within two weeks, demonstrating the strength of the profile method-

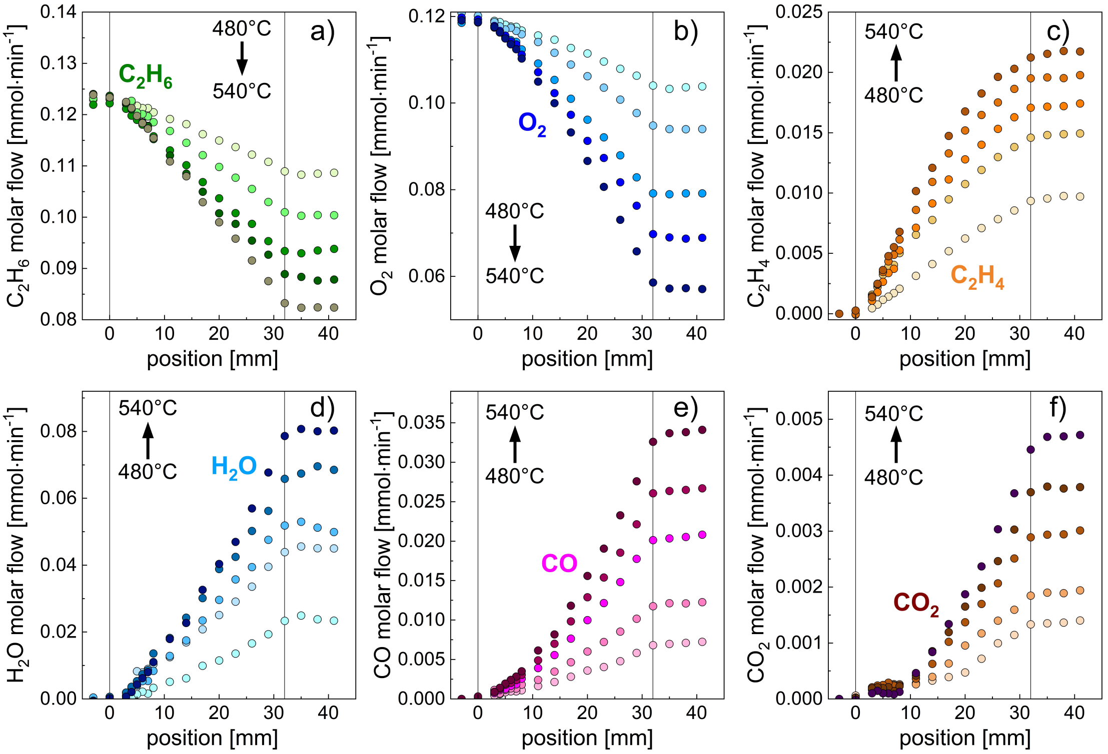

Figure 4.6: Species concentration profiles for all components measured at 480 (T13a), 500 (T13b), 520 (T13c), 530 (P13) and 540 °C (T13d) obtained in the C_2H_6 measurement plan. Reaction conditions: C_2H_6/O_2:10:10, 1 bar, 32 mm catalyst bed, 30 ml/min, 30 wt% MoO_3/γ-Al_2O_3.

ology in reducing the experimental workload required for the same information, as compared to the traditional end-of pipe analysis. Such data sets are highly beneficial for developing kinetic models, which is the content of the next section.

4.3 Kinetic Model Development

Since it is well established in research of ODH that reactions over transition metal oxides proceed usually by the MVK mechanism, it is used to macroscopically model the chemical system under investigation. The experimental data obtained in the catalyst activity studies (see Section 4.2) served as basis to develop the kinetic model. Experiments were performed solely in the presence of gas phase oxygen up to 60 % oxygen conversion. Therefore, the kinetic model includes only reactions

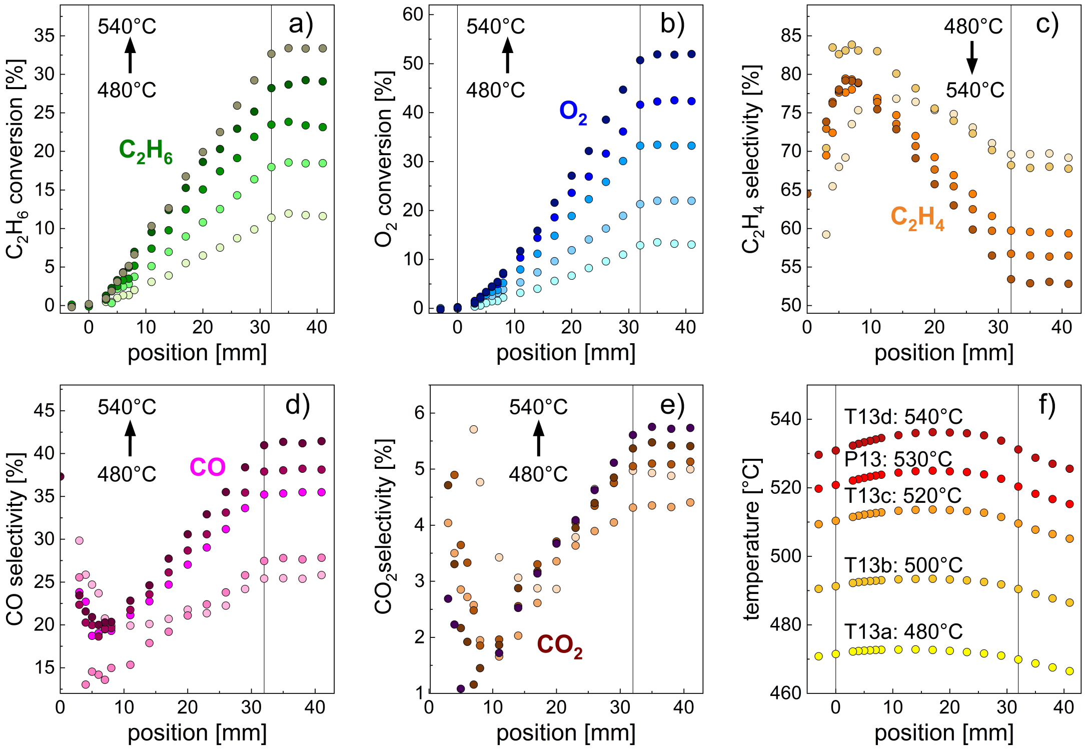

Figure 4.7: C_2H_6 (a), O_2 (b) conversion profiles and C_2H_4 (c), CO (d), CO_2 (e) selectivity profiles measured at 480 (T13a), 500 (T13b), 520 (T13c), 530 (P13) and 540 °C (T13d) (f) obtained in the C_2H_6 measurement plan. Reaction conditions: C_2H_6/O_2:10:10, 1 bar, 32 mm catalyst bed, 30 ml/min, 30 wt% $MoO_3/\gamma\text{-}Al_2O_3$.

with gas phase oxygen (Section 4.1). Furthermore, the goal is to derive a rate law that describes the observed data as simple as possible. For this, it is of central importance that the reactor is in steady state, because then all reaction steps have to be in steady state. Stable and reproducible operation within the time of the measurement campaign was observed (Subsection 4.2.1). Figure 4.8a-c) shows the modeled and the measured concentration profiles (P13) for all species at 530 °C and C_2H_6/O_2/inert:10/10/80.

Visual inspection of the results suggests that the fitting procedure was successful throughout all species except of CO_2. An evaluation of the goodness of fit was addressed by parity plots and calculating the Mean Absolute Percentage Error (MAPE). Results are shown in supplementary material (Figure A.11).

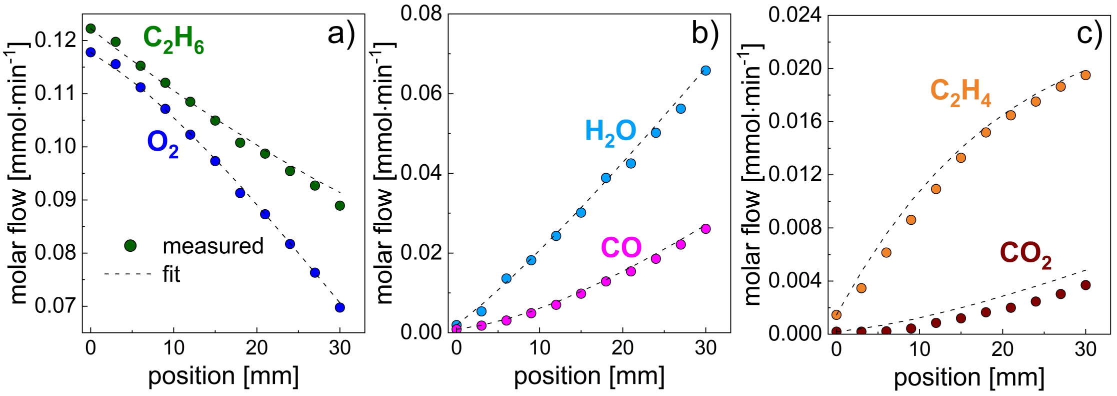

Figure 4.8: Measured species profiles of all components (P13) and the corresponding modeling results are shown. Reaction conditions: C_2H_6/O_2/inert:10/10/80, 530 °C, 1 bar, 32 mm catalyst bed, 30 ml/min, 30 wt% MoO_3/γ-Al_2O_3.

Table 4.1 shows the results of the kinetic model parameters obtained from the fitting process.

Table 4.1: Considered reaction steps in the MVK model for ODH of ethane. The reaction order of oxygen involved in the reoxidation of the catalyst is 0.3 ± 0.04 (Reaction Step 6).

Reaction	E_A [kJ/mol]	A_0 [mol/(kg s)]
$C_2H_6 + O_l \xrightarrow{k_1} C_2H_4 + H_2O + l$	102 ± 3	15.4 E-03 ± 0.53 E-03
$C_2H_6 + 5\,O_l \xrightarrow{k_2} 2\,CO + 3\,H_2O + 5\,l$	118 ± 6	0.96 E-03 ± 0.50 E-03
$C_2H_6 + 7\,O_l \xrightarrow{k_3} 2\,CO_2 + 3\,H_2O + 7\,l$	123 ± 6	0.31 E-03 ± 0.34 E-03
$C_2H_4 + 4\,O_l \xrightarrow{k_4} 2\,CO + 2\,H_2O + 4\,l$	54 ± 2	50.9 E-03 ± 5.66 E-03
$C_2H_4 + 6\,O_l \xrightarrow{k_5} 2\,CO_2 + 2\,H_2O + 6\,l$	89 ± 4	7.03 E-03 ± 3.60 E-03
$l + 0.5\,O_{2(g)} \xrightarrow{k_{ox}} O_l$	69 ± 3	248.0 E-03± 40.50 E-03

The main reaction of ethane ODH shows an apparent activation energy of $102.4\ \mathrm{kJ \cdot mol^{-1}}$. The partial and total combustion of C_2H_6 towards CO and CO_2 show high activation energies of $117.9\ \mathrm{kJ \cdot mol^{-1}}$ and $123.3\ \mathrm{kJ \cdot mol^{-1}}$. Lower activation energies of the entire reaction network are related to ethylene side reactions and the reoxidation of the catalyst. The relative low energy barrier determined for the reoxidation step of the catalyst structure suggests that this step is not rate determining, indicating that the structure is able to rapidly provide and incorporate oxygen. An analysis of the magnitude of reaction rates involved in the process indicates that indeed the reoxidation of the catalyst (r6) is the fastest process in the whole proposed reaction scheme (4.9a).

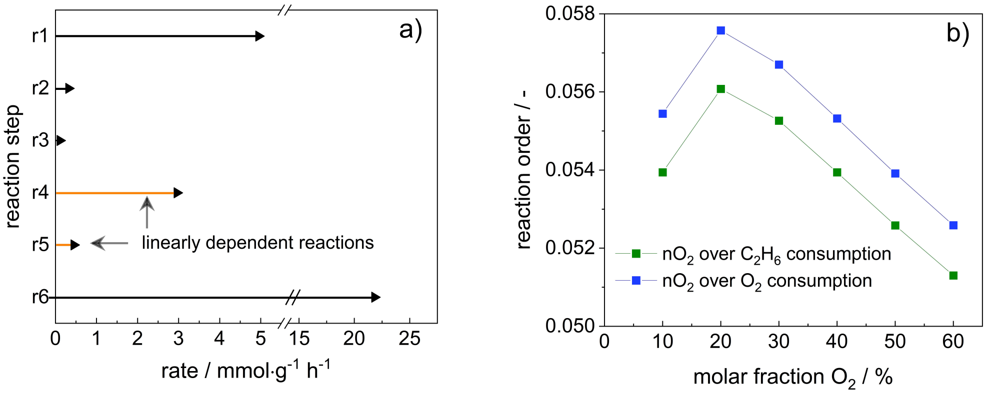

Figure 4.9: Evaluation of the rate determining step in the proposed MVK reaction scheme (a) and oxygen reaction order over ethane and oxygen consumption rate (b).

Previous results supporting this idea have been reported as it is in the case of Ressler et al. [138] who determined that reduction and reoxidation of MoO_x proceeds rapidly, i.e., solid state reaction is in the same order as gas phase reactions, at temperatures in the range of 773 K. With regard to side reactions, the partial oxidation of ethylene requires $53.6\ \mathrm{kJ \cdot mol^{-1}}$ while the energy required for total combustion is $88.8\ \mathrm{kJ \cdot mol^{-1}}$. These estimated values seem to be in agreement with profile observations shown in the previous Section 4.2. A comparison of activation energies and reparametrized exponential factors of individual reaction pathways that produce CO_x from hydrocarbons suggests that ethylene is the main contributor towards carbon monoxide in the range of operation conditions evaluated. This observation is congruent with results of previous studies where only minor parallel formation of carbon oxides coming from ethane was reported [22, 139].

Finally, in relation to the reaction order of oxygen involved in the reoxidation of the catalyst, a value of 0.3 was obtained. Hence, in this model the amount of oxygen in the gas phase has indeed a minor effect on the rate of reoxidation of the catalyst. A closer look at the magnitude of the kinetic parameters involved in this reaction step indicates that the process of providing oxygen through the catalyst is fast in comparison to other steps in the reaction mechanism.

The observations suggest that C_2H_6 consumption rate has a low reaction order with respect to O_2 concentration. An evaluation of the reaction order of O_2 as a function of its molar fraction, by using Eq. 4.12, is presented in Figure 4.9b.

$$n_{O_2} = y_{O_2} \frac{\partial \ln r_{net,C_2H_6}}{\partial y_{O_2}} \tag{4.12}$$

Spatially resolved measurement data provide insights into the reaction mechanism immediately upon application as shown in the example above. Initial consumption/production rates can be easily obtained from a simple linear regression analysis of the profiles at zero contact time. In combination with a reliable gas analytic system, this feature can be easily used to obtain experimental estimations of apparent activation energies as well as primary and secondary product formations. In a typical kinetic study setup under differential conditions, eleven parallel reactors would be needed in order to be able to reproduce one of the profiles obtained using the spatial profile measurement technique with the CPR. This advantage makes it possible to propose a kinetic model in a relatively short time interval (two weeks) and to reduce the required amount of experimental work heavily.

The results presented so far are only derived from gas phase analysis. Thus, information obtained are limited to a macroscopic understanding of the catalytic system under steady-state conditions. Further knowledge about the catalyst itself, apart from the theoretical parameter θ_{ox} that describes the percentage of oxidized sites, remains unknown. However, the observed changes in the reaction mechanism and in the color of the catalyst are inseparably linked to the structural changes in the catalyst. To unravel this interrelation of the reaction network and changes in the catalyst, both aspects are studied simultaneously in *operando* studies, representing the main focus of this thesis and the following chapters.

5 Spatially-Resolved *Operando* X-Ray Absorption Spectroscopy

In spatially-resolved *operando* XAS experiments local gas compositions, temperatures, and structural information along the catalyst bed are simultaneously measured. Structural information obtained from XAS add an additional information domain and allow us to unravel the changes in the catalyst structure along the catalyst bed and, in particular, around the IP (α) (see Section 4.1). In the first part of this chapter important considerations for method development are explained. After the relevant aspects for method development were provided, the second part examines the reactor profiles measured at P64, PETRA III. While this chapter provides a detailed explanation of the method development, the results shown in Section 5.2 have been previously published in [126]. The project was a collaboration between the groups of Raimund Horn (TUHH, Reacnostics GmbH), Michael Schmidt (Reacnostics GmbH), Thomas Sheppard (DESY, KIT), Dmitry Doronkin/Jan-Dierk Grunwaldt (KIT), and Christian Schroer (DESY, UHH).

5.1 Method Development

In the following section actions are described to adapt the CPR for enabling measurements in transmission mode (Subsection 5.1.1) as well as to optimize transmission values through the rather thick CPR reactor tube (Subsection 5.1.2).

5.1.1 Synchrotron CPR-XAS

Originally, the CPR was designed for spatially-resolved *operando* measurements using Raman spectroscopy [38]. For this methodology, only one optical access is needed, allowing to direct the laser light on the sample and to collect the reflected Raman signal on the same way back. Hence, only parts on the front of the CPR were designed with an opening, including three parts in total, namely: (1) lid CPR housing; (2) lid heating block (Fig. 5.1, left); (3) lid reactor tube. The latter encloses the reactor tube inside the heating block. These three parts remain unchanged for the CPR-XAS compared to the original CPR.

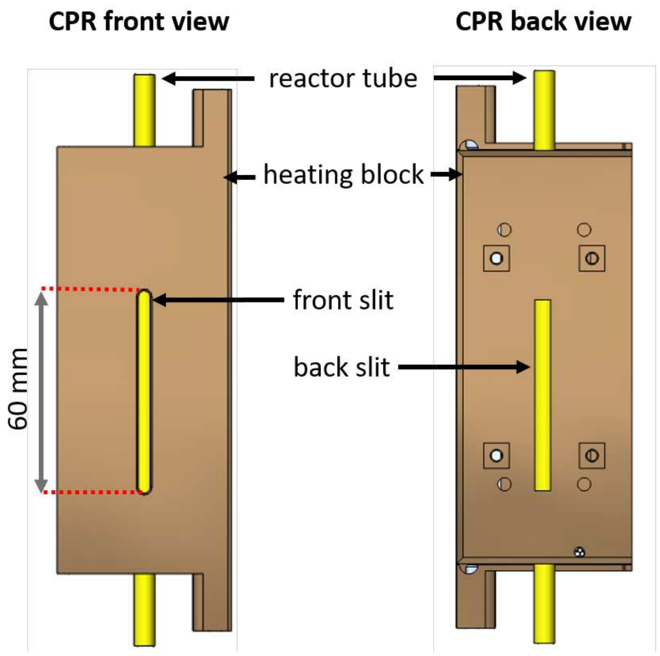

Figure 5.1: Schematic of the sample heating block in the CPR-XAS version showing the standard opening on the front (left) and the new slit on the back (right) to allow X-rays passing through the reactor tube. This figure is included in an article submitted to [125].

Method extension to XAS requires to collect X-rays downstream of the sample (transmission mode) or perpendicular to the incident beam (fluorescence mode) and thus, two optical accesses, one for the incident and one for the exiting X-rays. An opening perpendicular to the incident beam is not compatible with the integrated electronics of the CPR. Therefore, the CPR was modified to enable XAS measurements in transmission configuration. In this experimental geometry, signals are measured at the same position up- and downstream of the sample (0° between incident and exiting X-ray photons). For this purpose, parts on the reactor back were technically modified, including vertical slits (60 mm long) in the heating block parts (Fig. 5.1, right), and two more spherical openings (4 mm in diameter) in the lid of the reactor housing as well as in the cooling plate.

Since the reactor tube and the heating block are moved, while the capillary and the beam remain fixed in position, the heating block parts downstream of the sample were cut slit-shaped in order to provide access along the entire reactor bed. The openings were tested by moving the empty heating block, i.e., without a reactor tube installed, and monitoring transmission of the X-ray beam. This evaluation shows an actual measurement length of 55 mm instead of 60 mm, which is important to consider for packing a suitable catalyst bed length and to position the bed inside the reactor tube.

5.1.2 Sample Preparation

For the preparation of the rather thick reactor tube filled with catalyst (OD 6 mm, ID 4 mm) as XAS sample, it is essential to consider the total absorption just above the Mo K-edge energy (20.05 keV), the edge jump ($\Delta\mu\cdot$ x), as well as sample uniformity. The total absorption is the sum of absorption contributions from each material present, and crucial to take into account for estimating photon transmission. In case of the CPR reactor tube, the total absorption is determined by the wall thickness of the fused silica reactor tube, the MoO_3 weight loading on the catalyst support, the γ-Al_2O_3 support, and the catalyst bed porosity, illustrated in Figure 5.2.

Equation 5.1 was used to approximate transmission values (I_x/I_0) through the CPR tube according to Beer's law.

$$\frac{I_x}{I_0} = \exp\left(-\rho_{tot,SiO_2}\cdot x_{SiO_2}\cdot\sum\Phi_{i,SiO_2}\cdot\mu(E)_{m,i} - \rho_{tot,bed}\cdot x_{bed}\cdot\sum\Phi_{i,bed}\cdot\mu(E)_{m,i}\right) \tag{5.1}$$

Here, the first part of the exponential term describes absorption by the fused silica tube and the second by the catalyst particles within the reactor tube. In each term, the density of the sample material (ρ_{tot}), the mass fraction of each element i (ϕ_i) in the material, as well as the corresponding $\mu(E)_{m,i}$ value for the specific

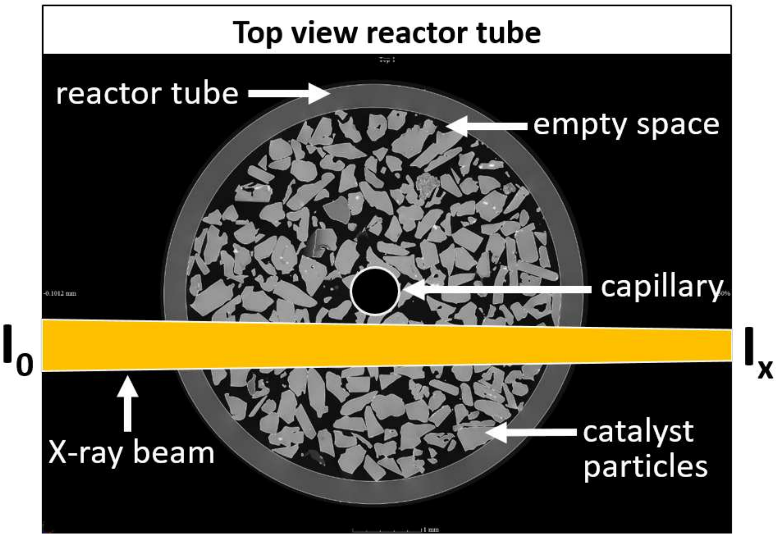

Figure 5.2: Illustration of the beam pathway passing through a CPR reactor tube filled with catalyst particles and a stainless steel capillary placed in the center.

energy above the edge energy, in our case around 20.05 keV, must be known. An example is given later in this subsection.

By using the same reaction conditions, i.e., reactor tube wall thickness 1 mm, 30 wt% MoO_3/γ-Al_2O_3, as applied in the catalyst activity investigation study (Section 4.2), basically none of the X-ray photons will get through the reactor tube. Therefore, the reactor sample had to be adjusted to allow XAS measurements at the Mo K-edge. Parameters to optimize are the MoO_3 weight loading (number of absorbing Mo atoms present), particle size (smaller particles result in a more densely packed catalyst bed), as well as the wall thickness of the reactor tube. With regard to the reactor tube, the OD of the reactor tube is fixed (6 mm) since it ensures direct contact with the heating block and thereby appropriate sample heating. In case of an empty reactor tube with a reactor tube wall thickness of 1 mm and a density of 2.2 g/cm^3 the X-ray intensity is attenuated to $\approx$ 33 %. Notably, this value corresponds to the transmitted fraction when the beam passes two times 1 mm as the beam enters and leaves the reactor tube. Thus, as a first step the reactor tube diameter was reduced to 600 μm resulting in approx. 51 % photon transmittance. The utilization of a thinner reactor tube wall results in a larger ID of 4.8 mm, filled with catalyst, which is preferable in terms of sample uniformity. To illustrate this point, it is key that the sample is as uniform as possible over the beam size as a result of the log dependency according to Beer's law. To take the log of sums, as it should be the case for XAS experiments to obtain meaningful spectra, is not the same as the sum of logs. Supported catalyst samples tend to be heterogeneous by nature. In our case, having different particle shapes caused by grinding and sizes due to the sieve fraction between 200 and 400 μm (Fig. 5.2), as well as most likely a non-uniform impregnation. Furthermore, the packed bed has irregular air spaces between the particles and the sampling capillary methodology requires to choose a measurement point (beam position) next to the capillary, which in combination with the circular reactor tubes contributes to uneven sampling. Therefore, larger inner reactor diameters allow to measure more particles at once, preventing spectra distortions as consequence of an uneven sample. As a counter effect, an increased number of Mo atoms at a given weight loading is present, which was addressed in the next step.

By using Eq. 5.1, the transmitted fraction through the CPR tube with a fixed wall thickness of 600 μm was estimated for different MoO_3 weight loadings in the range from 1 – 30 wt%. An overview of the used parameters and corresponding values, exemplified for a weight loading of 5 wt% MoO_3, is given in Table 5.1.

Table 5.1: Parameters used to caclulate transmission percent through the CPR tube, exemplified for 5 wt% MoO_3.

	Reactor tube	Catalyst
Component	SiO_2	MoO_3/γ-Al_2O_3
Beam pathway [mm]	1.2	4.8
Density [g/cm^3]	2.2	≈ 1
Element mass ratio [%]	Si: 46.74 O: 53.26	Mo: 3.33 Al: 50.28 O: 46.39
μ(20.05 keV) [cm^2/g]	Si: 4.431 O: 0.86	Mo: 79.046 Al: 3.417 O: 0.86

In Figure 5.3 photon transmission through the CPR tube as a function of MoO_3 weight loading is shown. The curve progression reveals that already at low MoO_3 weight loadings only a few percent of the incident photons transmit, pointing out the central question of how many photons are required for measuring meaningful spectra.

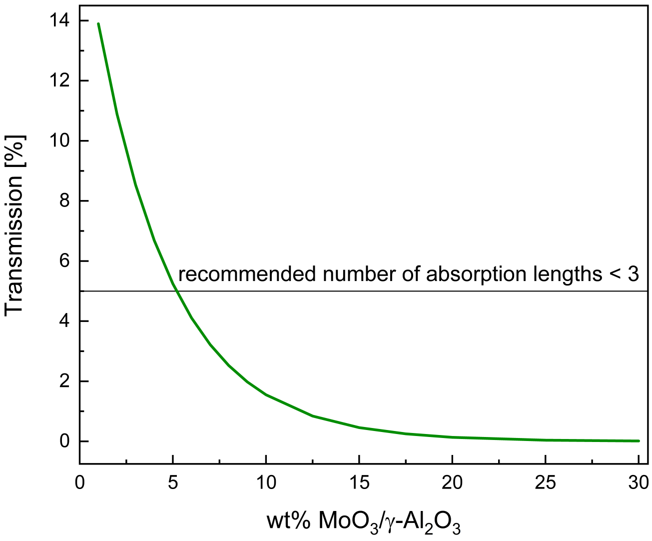

Figure 5.3: Photon percent transmittance through the CPR tube as function of MoO_3 weight loading.

As a simple rule of thumb, XAS community refers to ideal transmission values in terms of absorption lengths (μ·x). The recommended range is between one and three absorption lengths which corresponds to 37 – 5 % of photon transmittance. In Figure 5.3, the value of three absorption lengths is marked with the horizontal line in black at 5 % transmission, revealing that MoO_3 weight loadings below 6 % are required to fulfill the absorption length criterion. At these low transmission values, spectra distortions resulting from a weak sample signal, i.e., very few desired photons left downstream of the sample due to high total absorption values, might occur. Therefore, preliminary, ex-situ tests were performed to examine spectra quality of six catalysts with different MoO_3 weight loadings (2.5, 5, 7.5, 10, 15, 20). The catalyst samples were run under ODH operation conditions for several hours until full oxygen conversion. In this way, spectra quality in both regions (up- and downstream of position α) could be evaluated. The tests demonstrate applicability of catalysts up to 10 wt% MoO_3. Since from reaction point of view

MoO_3 weight loadings above 5 % are preferred to ensure that MoO_3 covers the support, which is not inert, the 10 wt% MoO_3 catalyst was chosen for the *operando* XAS experiments.

In summary, transmission could be optimized by tuning the wall thickness of the fused silica reactor tube as well as the MoO_3 weight loading on the catalyst support. However, thin wall thicknesses make the reactor tube rather fragile which restricts operation pressures to a lower value ($\approx < 5$ bar), while optimizing the weight loading is solely feasible with supported catalysts, if at all. Bulk catalysts can be mixed with inert materials, which requires careful examination of other parameters. For example, by mixing the catalyst with inert particles the contact time is reduced (lower GHSV) resulting in lower conversion values at the same total flow rate. The reduction of the total flow rate, to test a relevant range of reaction conditions or to reach a sufficiently high conversion level at all, requires careful evaluation of transport limitation as well as sampling flow rates through the orifice. To conclude, applicability of XAS with the CPR for a certain reaction system must be individually and carefully examined and will be restricted to edge energies above 15 keV. In the future, another opportunity is the usage of reactor tubes made of glassy carbon, making the absorption by the reactor tube material basically neglectable and thereby broaden flexibility of the catalyst material in the sample. A major drawback is that the tubes are very costly with ≈ 1000 € per tube.

5.2 Spatial Profile Results

After careful optimization of the reactor sample for spatially-resolved *operando* XAS measurements with the CPR-XAS system, profile experiments were carried out using a 10 wt% $MoO_3/\gamma\text{-}Al_2O_3$ catalyst. In the following section the concentration profiles and the simultaneously measured XANES profile are shown.

5.2.1 Species Concentration Profiles

In Figure 5.6 species concentration profiles of the feed components C_2H_6 and O_2, the main products C_2H_4 and H_2O as well as the undesired carbon oxides CO and CO_2 are presented.

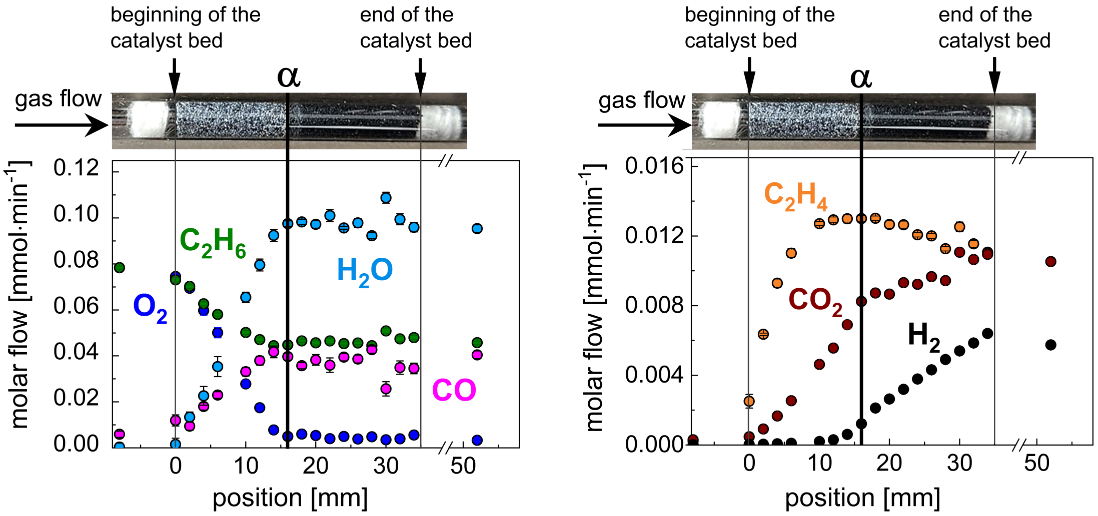

Figure 5.4: Species concentration profiles measured simultaneously with the XAS profile. Reaction conditions: C_2H_6/O_2/inert:10/10/80, 530 °C, 1 bar, 35 mm catalyst bed, 20 ml/min, 10 wt% $MoO_3/\gamma\text{-}Al_2O_3$. The sample is mounted vertically during the measurements.

The measurement compare well with the species concentration profiles presented thoroughly in Section 4.1 as well as reported in literature [22], having common characteristics, e.g., profile shapes, species present, α. For a detailed description of the concentration profiles, the reader is referred to Chapter 4. With regard to this measurement, CO and H_2O concentration profiles are calculated from species balance and sum up measurement errors contributing from all other species. Therefore, very small changes in H_2O and CO are difficult to evaluate. The hydrogen concentration profile presented in Figure 5.6 is measured, confirming experimentally that hydrogen diffuses upstream point α, which was observed in the calculated hydrogen profile 4.1.

Furthermore, due to the particular relevance of the bed position α for the method development in this entire work as well as with respect to the XAS profile results in the next subsection, it is noteworthy that the position of α is at 16 mm. Distinct changes in the color and performance of the catalyst are likewise observed around α as described previously in Section 4.1.

5.2.2 XAS Profiles

Seventeen XAS spectra at the Mo K-edge were recorded under ODH reaction conditions through a 35 mm long and 4.8 mm thick catalyst bed. The spectra were taken at the same positions as the sampling points of the species concentration profiles discussed in the previous Subsection 5.2.1. Figure 5.5 shows the normalized Mo K-edge XAS spectra (XANES region) measured as a function of position (Fig. 5.5, left) and LCA reveals the bulk Mo average oxidation state (Fig. 5.5, right). Noticeable is the sharp decrease in the average Mo oxidation state at position 16 mm (α), whereas the spectra before and after this position are almost constant.

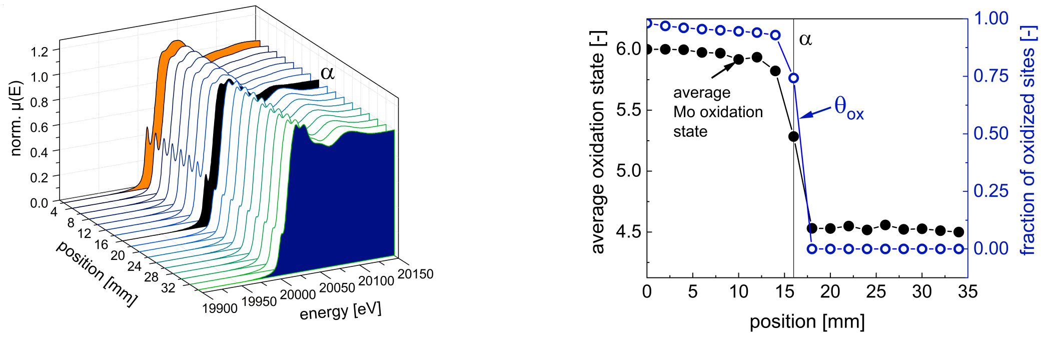

Figure 5.5: *operando* XANES measurement atthe MoK-edge. Normalized XANES spectra as a function of the catalyst bed position (left); Linear combination analysis using spectra at the beginning (2 mm) and end (34 mm) of the catalyst bed as internal references and fraction of oxidized sites over catalyst surface obtained from the kinetic model (right). Reaction conditions: C_2H_6/O_2/inert:10/10/80, 530 °C, 1 bar, 35 mm catalyst bed, 20 ml/min, 10 wt% $MoO_3/\gamma\text{-}Al_2O_3$.

To evaluate average oxidation states from the measured XAS profile, orthorhombic MoO_3 and monoclinic MoO_2 corresponding to Mo(VI) and Mo(IV) were used as references. In Figure 5.6a, the sample spectra at position 2 mm and position 34 mm as well as the bulk MoO_3 and MoO_2 reference spectra are shown.

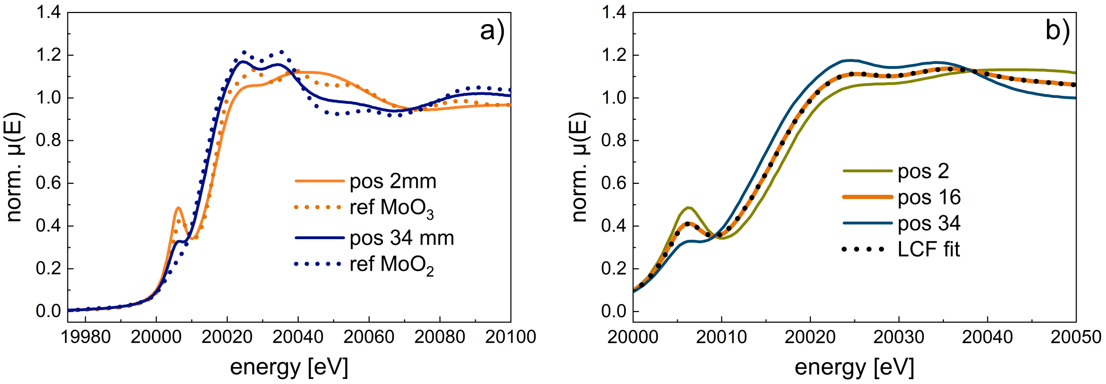

Figure 5.6: Normalized XANES spectra measured *operando* atMoK-edge at the beginning (2 mm) and end (34 mm) of the catalyst bed. a) Reference spectra of orthorhombic MoO_3 and monoclinic MoO_2 corresponding to Mo(VI) and Mo(IV) illustrated by dotted lines. b) Linear combination analysis of the spectrum at position 16 mm (position α, full oxygen conversion) between the spectra at position 2 and 34 mm.

The discrepancy between the reference spectra and sample spectra reveals a different structure of the supported MoO_x species relative to the bulk reference compounds. The spectrum measured at 2 mm is identical to the one of the calcined catalyst (not shown) and shows the same features and the same energy position E_0, allowing an assignment to Mo(VI) oxidation state. The spectrum at position 34 mm reveals the rising edge position and the white line shape (strongly absorbing feature(s) just above the rising edge) similar to the MoO_2 reference spectrum, however with a small contribution of an edge feature at 20006 eV as in the Mo(VI) spectra. To determine the exact oxidation state of this internal reference state the spectrum was fitted in the rising edge region (20008 - 20030 eV) to a linear combination of 2 mm (best available Mo(VI) reference) and the MoO_2 reference spectrum. This resulted in an average oxidation state of +4.5 at the end of the catalyst bed.

Transition metal oxide catalysts, as MoO_3, are able to exchange readily lattice with gas phase oxygen and provide lattice oxygen for ODH reactions, as in more detail described in the theory part (Subsection 2.1.1). This is observed by a quick change in color from yellow to gray of the calcined MoO_3 catalyst at the very beginning of the catalyst bed upon reaction since optical properties of the catalyst are interrelated to its structure. Optical properties of molybdenum oxides change strongly as a function of the oxygen vacancy concentration, indicating that the gray color results from induced oxygen defects in the catalyst material. The oxygen vacancy concentration is thermodynamically determined by the oxygen partial pressure and increases with decreasing oxygen partial pressure. Thus, the MoO_3 catalyst is reduced to a certain degree in response to the local gas phase composition and temperature. Although the oxygen partial pressure declines rapidly until position 16 mm (α), the average bulk oxidation state of Mo remains almost unchanged, showing only a minor gradual decrease until α. This indicates that only a low concentration of oxygen vacancies is formed in the deep bulk. Reduction and reoxidation are obviously restricted to a near-surface region. Another possible explanation, reported in literature, is that the increasing oxygen vacancy concentration in steady-state at each position with the declining gas phase oxygen concentration could have lead to the formation of different suboxides like $Mo_{18}O_{52}$, Mo_8O_{23}, Mo_5O_{14} and Mo_4O_{11}, that have average oxidation states around 5.6 – 5.8 [140]. The formation of only near-stoichiometric MoO_{3-x} (x close to 0) compounds are able to compensate for oxygen vacancies in the bulk without that the average Mo oxidation state changes. It is further speculated in literature that one of the well-defined molybdenum suboxides constitutes the active phase in ODH [141]. The gradual reduction of such a molybdenum suboxide phase could explain the slight decrease in the average Mo oxidation state upstream of position α.

Below a certain oxygen partial pressure, the structure cannot compensate for oxygen vacancies anymore and structural changes are induced rapidly, occurring between positions 14 and 18 mm. Linear combinations of spectra at the beginning (2 mm) and end of the catalyst bed (34 mm) show that the spectrum at position 16 mm can be created by mixing of the two. Therefore, position 16 mm is a weighted average of the two. Consequently, two isosbestic points arise, illustrated in Figure 5.6b. This shows that no stable or new intermediate phase can be detected with XAS. This observation is in line with studies performed by Ressler et al. [140], who showed that reaction temperatures above 700 K make a fast and complete transition of MoO_3 into MoO_2 feasible through the participation of a considerable amount of lattice oxygen in combination with a rapid formation and growth of MoO_2 nuclei.

Beyond α, the catalyst possesses a dark blue color, characteristic for MoO_2, that turned even darker towards the end of the bed. The average Mo oxidation state stabilizes close to Mo(IV).

In summary, obtained information agree with catalytic performance studies (Chapter 4) as well as with the kinetic model (Section 4.3) and complements it with a mechanistic understanding of underlying physico-chemical phenomena. This chemical understanding can be used to derive and tune models more efficiently, and also to validate them. While data quality is strongly determined by the reactor system, among others, the type of structural information is deduced and thus determined by the applied catalyst characterization technique. Hence, a considerable motivation exists to expand the characterization portfolio for *operando* spatial profiling methodologies, which is presented in the next chapter.

6 Spatially-Resolved *Operando* X-Ray Diffraction

XRD represents a commonly established catalyst characterization technique for crystalline phase composition analysis, applied in various catalysis studies whether at laboratory or synchrotron radiation facilities. Therefore, the *operando* profiling methodology using XAS (Chapter 5) was extended to spatially-resolved high-energy XRD, which is the subject of this chapter. The goal is to measure spatially-resolved *operando* XRD data that allow deducing how the catalyst adapted in its crystalline phases along the catalytic bed in response to the strongly changing reaction environment. Essential considerations for method development are described first. After establishing the basic requirements of this methodology, experimental *operando* profile results are presented. The results shown in Subsection 6.2.1 have been previously published in [131] and the results in Subsection 6.2.2 in [125]. Further, the Rietveld fit shown in Subsection 6.2.2 has been conducted by Ida Nielsen, who belongs to the DESY cooperation group. The project was a collaboration between the groups of Raimund Horn (TUHH, Reacnostics GmbH), Michael Schmidt (Reacnostics GmbH), Thomas Sheppard (DESY, KIT), and Ann-Christin Dippel, Marina Sturm, Olof Gutowski, Ida Nielsen from P07/P21.1 (DESY).

6.1 Method Development

In this section technical modifications of the CPR-XAS to obtain the modified CPR-XRD version are described. Crucial for the CPR-XRD design was to adapt the size of the reactor window for enabling measurements of scattered X-rays in transmission mode, and at the same time to keep the reactor window size as small as possible in order to ensure uniform reaction temperatures, which is explained subsequently.

6.1.1 Synchrotron CPR-XRD

Reactor modifications required for the CPR-XAS (Subsection 5.1.1) focused on enabling the beam to pass through the reactor without hitting another reactor part except of the CPR reactor tube filled with catalyst particles. Since the signal in XAS measurements is collected at the same position downstream and upstream of the sample, experiments can be conducted from both directions of the reactor. Furthermore, the measurement position (beam position) can be chosen on the right or the left side of the capillary, as long as the beam does not hit the stainless steel capillary. In contrast, XRD measurements with the CPR-XRD are direction and beam position dependent. Since a scattered X-ray signal is collected downstream of the sample over a defined angular cone, corresponding reactor modifications are not symmetric. The incident X-ray beam is directed from the back of the CPR on the sample (Fig. 6.1a) and, with a view in beam direction, positioned on the right side of the capillary (Fig. 6.1b).

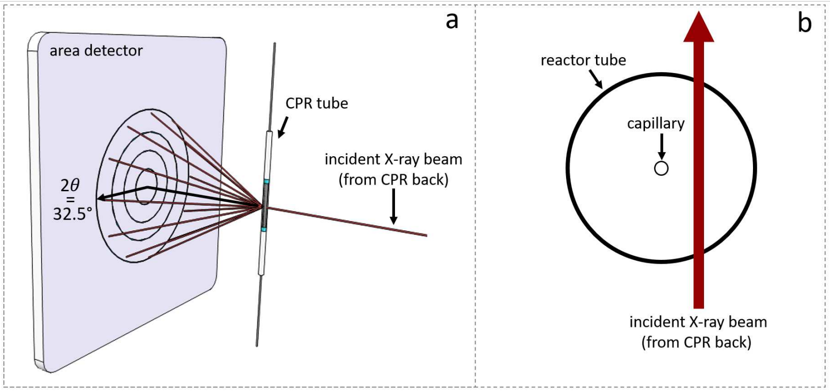

Figure 6.1: Schematic of the X-ray beam pathway through the reactor tube. (a) The X-ray beam passes the reactor tube from the back of the CPR and the scattered signal is collected on the front. (b) The X-ray beam is positioned next to the capillary.

Compared to XAS, the X-ray signal differs only downstream of the sample. Hence, solely the parts on the reactor front (downstream of the sample) were cut to allow measurements of scattered X-rays in transmission mode with a maximum solid angle of 2θ up to 32°. The modifications include the reactor cover (Fig. 6.2, A) as well as two covers of the heating block (Fig. 6.2 B, C).

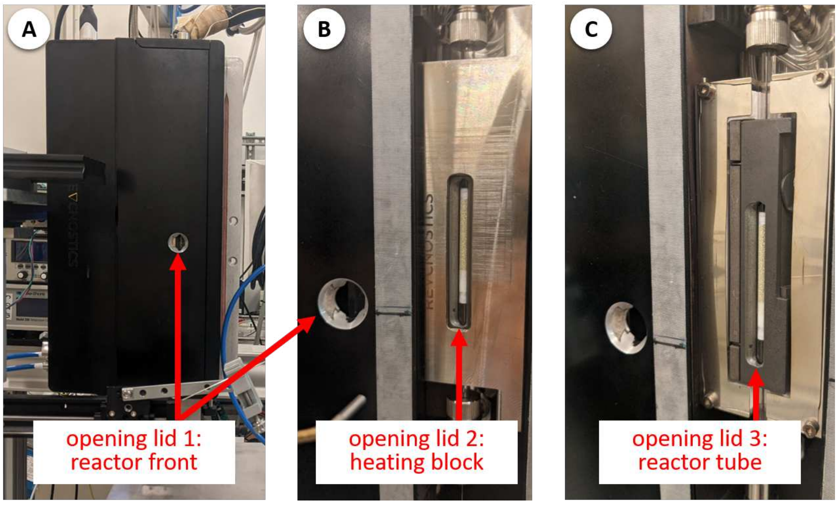

Figure 6.2: Enlarged openings in the parts of the reactor front for the development of the CPR-XRD version to allow measurements of scattered X-rays in transmission mode with a maximum solid angle of 2θ up to 32°.

The correct position of the openings next to the capillary was verified by moving the reactor relative to the X-ray beam in the horizontal direction, as shown in Figure 6.3. The measurement position, marked in red, was chosen at the signal intensity plateau between 136.75 – 135.75 mm, originating from the sample. The three higher intensity peaks correspond to metal signals from the heating block or sampling capillary.

6.1.2 Sizing the CPR Reactor Window

Spatially-resolved powder diffraction analysis of the catalyst during the reaction requires to pass through the CPR reactor tube (OD 6.0 mm, ID 4 – 5.6 mm) with a sufficient number of photons scattered from the catalyst sample, and at the same time to record the transmitted, scattered X-ray photons over an opening angle large enough to measure relevant structural information from most catalytic materials. In this regard, the usage of high photon energies is very beneficial because it strongly reduces beam attenuation as the X-ray beam traverses sample

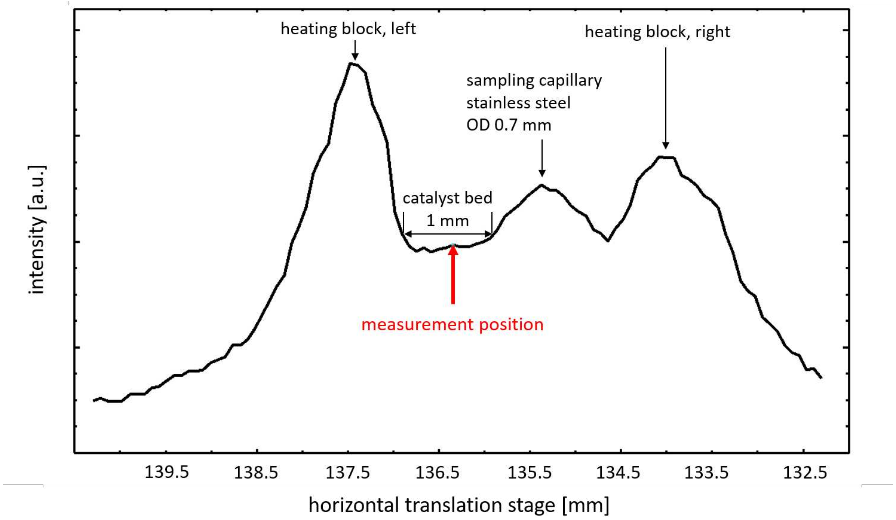

Figure 6.3: X-ray intensity monitored through the CPR in measurement configuration, while the CPR is moved horizontally using the beamline sample stage.

materials, and thus facilitates transmission experiments on thicker samples. In lab-based X-ray systems the highest penetration depths of X-rays into or through sample materials are obtained by utilizing anode materials such as Ag or Mo that generate X-rays with photon energies of 17.5 keV and 22.2 keV. However, in this photon energy range beam attenuation is still significantly high resulting in similar optimization problems as described for XAS in Subsection 5.1.2. In addition, the flux provided by lab-based X-ray systems is too low in order to achieve diffraction signals from the catalyst sample distinguishable from noise, whether XRD experiments are carried out on the CPR tubes in reflection or transmission. Alongside these reasons, the usage of photon energies above 50 keV is practical for conducting XRD experiments on the CPR since divergence of the exit beam is minimized and a wider d-value range within a fixed (small) angular cone can be measured. Thereby, a smaller sample window size in the reactor is required for obtaining the same information in XRD experiments carried out with high energies compared to low energies. To illustrate this point, a full pattern with a 2θ range of 140° at 8.05 keV (Cu radiation) is equivalent to approximately 15° at 103 keV (Fig. 6.4a).

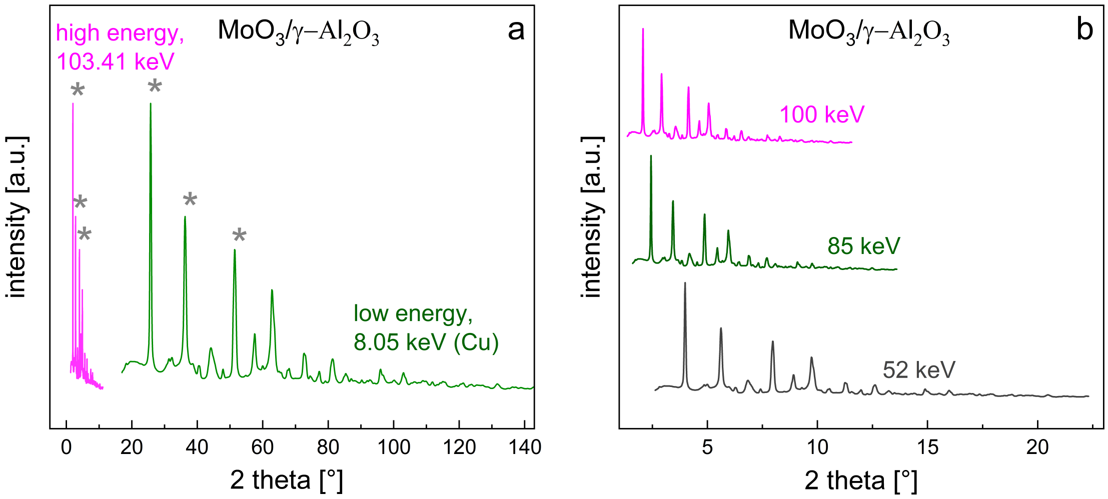

Figure 6.4: Diffraction pattern illustrated at different energies. (a) Pattern at high-energy (pink) and low-energy (green). (b) Pattern at energies available at beamline P21.1.

Small opening angles are crucial since optical access for the exiting, scattered X-rays must be technically realized by cutting the covers of the sample oven (Subsection 6.1.1), which as a consequence affects sample heating, reaction temperatures, and potentially isothermicity in the radial and axial direction of the catalyst bed. To conclude, in order to perform *operando* XRD measurements through the CPR reactor tube require X-rays with high-energies (> 50 keV) and high flux, as available at dedicated beamlines at synchrotron radiation facilities. For sizing the reactor window, relevant 2θ ranges determined by catalyst samples as well as commonly available photon energy ranges at several beamlines were considered. The beamlines P07 and P21.1 provide X-rays with tunable energies in the range of 30 to 200 keV (P07) or fixed energies at 52, 85, 100 keV (P21.1). Important details on setup integration at both beamlines are given in Subsection 3.6.2. Figure 6.4b shows the same pattern as in Figure 6.4a at the three different energies feasible at P21.1. As a result, already small reactor windows with a solid angle of $10 - 20°$ are suitable for most catalyst materials. In order to test the feasibility of total scattering techniques (PDF analysis), a slightly larger 2θ range of approximately $30 - 35°$ was cut, although $10 - 20°$ are preferable in terms of uniform reaction temperatures.

Prior to modifying the CPR, data quality was tested and verified via ex-situ measurements for different reactor IDs (4.0, 4.8, 5.2, 5.6 mm), particle sizes (50 – 100, 100 – 200, 200 – 400 µm) and catalyst materials (10 - 30 wt% $MoO_3/\gamma\text{-}Al_2O_3$, M1 (MoVTeNb oxide). Patterns measured through a CMR tube (OD 1 mm / ID 0.98 mm) and the CPR tube (OD 6 mm / ID 5.6 mm), one each, are shown in Figure 6.5. The signal at 3.5° was used for intensity normalization. The patterns are very similar in terms of the main reflections and demonstrate that no significant peak broadening occurs by measuring through the larger CPR reactor diameters.

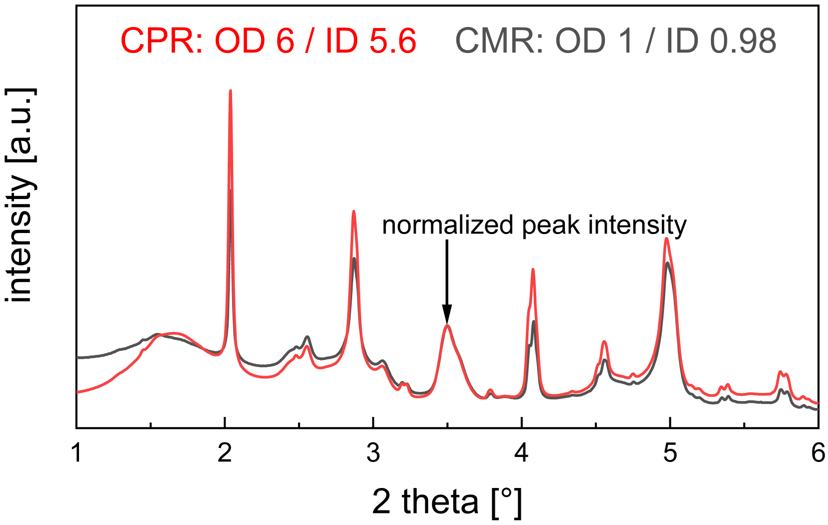

Figure 6.5: Patterns acquired in two different reactor systems. The pattern in red was measured in the rather large reactor tube diameter of the CPR and the pattern in black in a small reactor tube diameter of a CMR.

In summary, the reactor was successfully modified to enable XRD measurements in transmission mode, and ex-situ measurements verified feasibility of the new measurement concept. XRD results obtained with the CPR-XRD *operando* are the content of the following section.

6.2 Spatial Profile Results

Profile experiments were carried out at beamlines P07 and P21.1 (PETRA III, DESY) using a 30 wt% $MoO_3/\gamma\text{-}Al_2O_3$ catalyst. XRD results from both beamlines compare well with each other in terms of the main features. Therefore, the following chapter will only focus on the XRD data obtained at P07. Results from P21.1 are shown in supplementary material (Fig. A.12 – A.14). Subsection 4.2.1 demonstrates long-term catalyst stability under operating conditions as well as reliable operation of the profiling methodology with the CPR setup by comparing concentration and temperature profiles between original and replicate runs. Following the same procedure, the observations can be complemented with structural data from XRD, presented in the first Subsection 6.2.1. In the subsequent section, spatially-resolved XRD data from one profile run are analyzed in detail.

Simultaneously measured gas compositions are not presented in this chapter. Corresponding results at P07 (MS) are shown in the supplementary material (Fig. A.15). Results obtained at P21.1 (GC) were shown previously in Section 4.1 to introduce the general basics of the reaction system in the presence and absence of gas phase oxygen. All species concentration profiles measured in this work compare well in terms of the main features with each other P21.1 vs. P07 as well as with *operando* profiles with XAS at P64 (Subsection 5.2.1). The profiles at P21.1 served as example for profiles conducted until full gas phase oxygen conversion since other profiles have a lower data quality in comparison. In particular, gas analysis via MS for ethane ODH is difficult, because many masses are overlapping in this reaction system. Further, reliable species quantification by MS is restricted to oxygen conversion levels up to 60 % because at higher oxygen conversion levels instabilities of the MS (e.g., signal response behavior) occur that result from a corresponding change in the oxidative properties of the reaction mixture.

6.2.1 Stability and Reproducibility

Six *operando* XRD profile runs were carried out at beamline P07, comprising three original and three replicate runs. Each profile run contains background features (e.g., the fused silica reactor) which should remain unchanged throughout all profiles conducted within the same reactor tube. Comparing the same measurement positions between different profile runs allows us to evaluate the operation stability of the beamline and reactor. Figure 6.6 shows normalized patterns of all profiles acquired of the empty reactor tube (Fig. 6.6a, -10 mm, OD 6.0 mm/ID 5.6 mm), close to the catalyst bed (Fig. 6.6b, -2 mm), and at the start of the bed (Fig. 6.6c, 0 mm). The fused silica reactor tube shows characteristic signal contributions with a broad signal in the q range of 1.2 – 2 Å^{-1} (Fig. 6.6a). A good match between all patterns at this position is observed, confirming stable beamline operation over the whole measurement time of 28 h. QW plugs were used to fix the catalyst bed in position, resulting in a short zone where mixing between QW and catalyst particles is observed. By shaping the beam size to 0.5 × 0.5 mm^2 on the sample, minor reflections from the catalyst, therefore, appeared at -2 mm in all profile runs (Fig. 6.6b). This information should be considered when evaluating initial slopes of species concentration profiles. Diffractograms obtained at position 0 mm (Fig. 6.6c) show pronounced catalyst signals compared to positions before, indicating that the beam is fully positioned within the catalyst bed. Therefore, this position is assigned to the beginning of the catalyst bed. Notably, the patterns recorded at the same position (-2 or 0 mm) show significant changes in total intensities (e.g., 1.64 Å^{-1}, 1.92 Å^{-1}) and signal to background ratios, which is related to changes of the catalyst structure with time, not further discussed in this work.

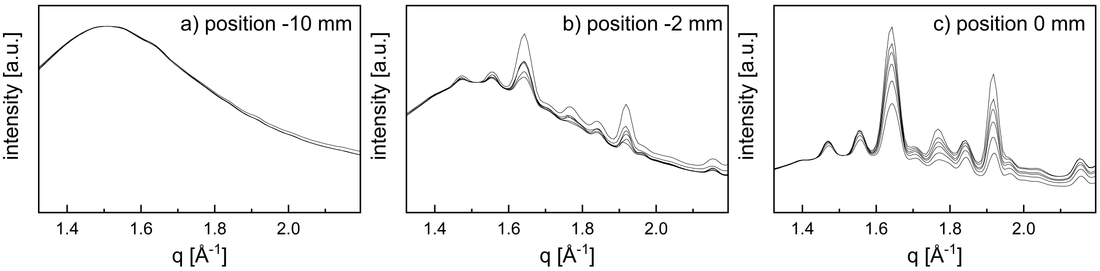

Figure 6.6: XRD patterns of all profile runs at three different positions measured *operando* at beamline P07, PETRA III (Hamburg, Germany) over 28 h. a) Empty reactor tube (position -10 mm); b) Mixture of catalyst particles and QW close to the beginning of the catalyst bed (position -2 mm); c) Beginning of the catalyst bed (position 0 mm). Diffractograms are normalized to the maximum of the fused silica signal at 1.5 Å^{-1}.

However, the pronounced change between patterns acquired at the transition zone (Fig. 6.6b) and the beginning of the bed (Fig. 6.6c) is reproducible between all profiles, confirming that the same sample volume was probed in each profile. This demonstrates precise and stable motor positioning of the spatial profile reactor, as well as negligible impact of the spatial profiling methodology caused by repetitive moving of the sampling capillary through the center of the catalyst bed. For example, the latter could have led to particle attrition and densification of the bed, which would have shifted the start position of the catalyst bed down in the vertically positioned tube. This should be considered with care when using capillary sampling in catalyst materials, which may have low mechanical stability. A densification of the catalyst bed could result in different catalyst mass per sample position with strong impact on species concentration profile measurements and hence, on catalytic performance observations and deduced kinetic parameters.

Overall, the XRD results complement observations made in Subsection 4.2.1, demonstrating long-term stability and reproducibility of the profile measurement technique with the CPR and the used reaction system.

6.2.2 XRD Profiles

An overview of the obtained XRD patterns simultaneously measured with local catalyst activities is presented in Figure 6.7. Here, twenty-seven diffractograms were recorded at the same positions as the sampling points of the species concentration profiles, which form the corresponding XRD profile through the 38 mm long catalyst bed. The catalyst bed can be separated into three zones (0 – 18 mm, β: 18 – 24 mm, 24 – 38 mm) based on structural similarities. XRD patterns before (0 – 18 mm) and after (24 – 38 mm) β are very similar with respect to the occurring reflections, whereby the first bed zone shows changes in the signal-to-background ratio and peak intensities and the third zone varying peak intensities, which will be discussed later in this subsection. In the second bed zone, denoted as β, XRD reveals a pronounced phase transformation, which starts at the point of full gas phase oxygen conversion (α, 18 mm) obtained by the species concentration profiles (Fig. A.15a, d).

An overview of the phase transformation is illustrated in Figure 6.8. The diffractograms measured before and after position β are represented by the patterns at position 2 mm and 36 mm, respectively, which are shown in a 2θ range of 1.3 – 6° on the left (Fig. 6.8a, b), and with a smaller angular region of 1.5 – 3° on the right (Fig. 6.8c, g). Further, patterns acquired inside the transition zone β at 19 mm (Fig. 6.8d), 20 mm (Fig. 6.8e), and 21 mm (Fig. 6.8f) are shown in the stack plot

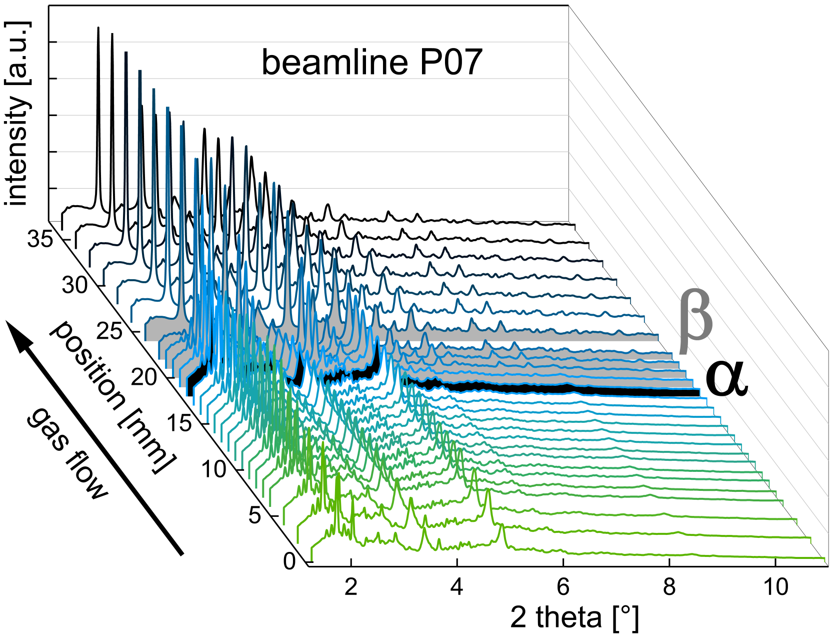

Figure 6.7: *operando* XRD profile simultaneously measured with temperature and gas concentration profiles at beamline P07, PETRA III (Hamburg, Germany) during ethane ODH. α (black colored pattern, 18 mm) marks the position of full gas phase oxygen conversion with different catalyst performances before and after. β (grey-colored patterns, 18 – 24 mm) marks the catalyst bed range where the catalyst undergoes distinct phase transformations. Reaction conditions: $C_2H_6/O_2/N_2$:10/10/80, 515 °C, 1 bar, OD 6 mm/ID 5.6 mm, 38 mm catalyst bed, 15 ml/min, 30 wt% MoO_3/γ-Al_2O_3, beam size 0.5 × 0.5 mm^2 (h × v), 103.4 keV (λ = 0.1199 Å).

(right). Each diffractogram has signal contributions from the reaction tube (fused silica) and support material (γ-Al_2O_3). A corresponding pattern of the reactor tube filled with pure support material is shown in Fig. 6.8a and b, illustrated in green. Fused silica shows a characteristic broad shoulder in the 2θ range of 1.4 – 2°, while the strongest reflections from γ-Al_2O_3 occur at 3.5° 004 and 4.9° 044 [ICDD 98-003-0267]. The as-prepared calcined sample exhibits a yellow color at 515 °C in O_2/N_2:20/80. Upon reaction, the catalyst changed color quickly from yellow to gray at the beginning of the catalyst bed. The corresponding sample diffraction patterns measured at 2 mm (Fig. 6.8a) cannot be assigned either to the previous MoO_3 phase or another obvious phase mixture.

Molybdenum oxides are known to form numerous intermediate oxides, such as Mo_5O_{14} [ICDD No-. 98-007-2639], $Mo_{18}O_{52}$ [ICDD No-. 98-002-7510], $Mo_{17}O_{47}$

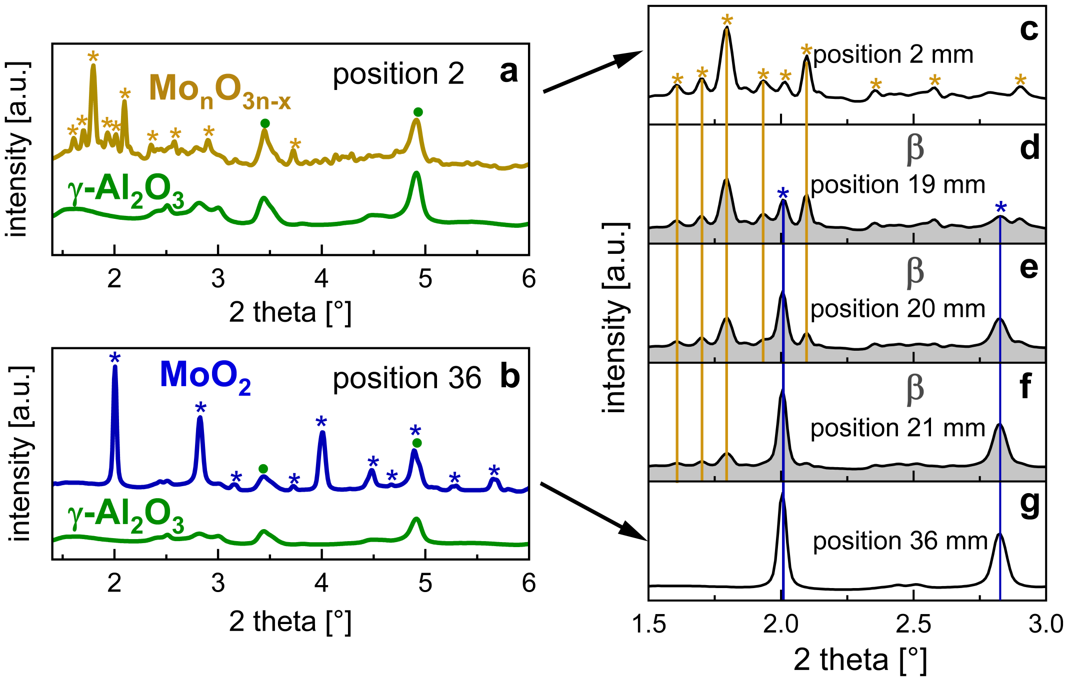

Figure 6.8: XRD patterns measured *operando* at beamline P07, PETRA III (Hamburg, Germany). a, c) Diffractogram at the beginning of the catalyst bed (yellow, 2 mm, before) in the presence of gas phase oxygen; b, g) Diffractogram at the end of the catalyst bed (blue, 36 mm, beyond) in the absence of gas phase oxygen. a, b) Each pattern contains signal contributions from fused silica and alumina. A corresponding pattern is shown in green. d – f): XRD patterns measured at the catalyst bed position (18 – 24 mm). Reaction conditions: Reaction conditions: $C_2H_6/O_2/N_2$:10/10/80, 515 °C, 1 bar, OD 6 mm/ID 5.6 mm, 38 mm catalyst bed, 15 ml/min, 30 wt% MoO_3/γ-Al_2O_3, beam size 0.5×0.5 mm^2 (h × v), 103.4 keV (λ = 0.1199 Å).

[ICDD No-.98-002-8333], Mo_9O_{26} [ICDD No-. 98-003-8014], Mo_8O_{23} [ICDD No-. 98-020-2203], Mo_4O_{11} [ICDD No-. 98-002-4033] [140–142]. Main reflections originating from the aforementioned phases occur in a low 2θ range of 1.6 – 2.2° or show very low intensities. The ability of molybdenum oxides to rapidly exchange gaseous oxygen leads to the formation of various suboxides, small crystallite sizes, and an oxygen defective structure, whose extent is thermodynamically determined by temperature and the local oxygen partial pressure. Oxygen defects cause peak broadening as well as small crystallites, which decrease the resolution and might have led to overlapped or hidden reflections, making phase identification challenging. While the XRD patterns show a stable phase mixture over the measurement time at one bed position, the patterns between the sampling positions in the first reaction zone show a varying signal-to-background ratio and peak intensities. Here, the strongly decreasing oxygen concentration results in a varying phase composition along the catalyst bed, consisting of a mixture of molybdenum (sub)oxides with a changing crystallite size and number, including the formation of XRD amorphous phases.

The XRD patterns obtained beyond β (36 mm, Fig. 6.8b) show crystalline MoO_2 with a monoclinic crystal structure ([ICDD No-. 98-015-2316) as the only crystalline phase related to molybdenum oxide. The onset of reduction of Mo_nO_{3n-x} to MoO_2 is seen at position 19 mm (Fig. 6.8d) through the appearance of MoO_2 reflections and at the same time decreasing Mo_nO_{3n-x} signals. At 24 mm no reflections corresponding to non-stoichiometric oxides are detected anymore.

The course of the phase transformation is further addressed by the evaluation of peak areas at 2θ of 1.80° and 4.01°, showing no overlap and strong reflections corresponding to Mo_nO_{3n-x} and MoO_2, respectively (Fig. 6.9).

Noticeable is a sharp decrease in Mo_nO_{3n-x} and an increase in MoO_2 from 18 – 24 mm, which complements previous observations of catalyst reduction. The oscillation in the signals upstream and downstream of this region are observed similarly in the XRD profile measured at P21.1, without showing the same oscillatory trends, indicating a random variation. For both measurements 15 images were recorded at each position, showing no significant deviations. Hence, XRD measurements were reproducible and showed a negligible statistical error. A possible explanation for the observed variations along the bed could be related to insufficient particle statistics in the XRD measurements, compared to optimal powder XRD analysis. With respect to the setup, the sample cannot be rotated. In addition, a compromise had to be found to fulfill the requirements of reaction engineering and XRD analysis, leading to the usage of rather big catalyst particles (300 – 400 µm). Therefore, effects resulting from crystal orientation, e.g., directional crystal growth at high temperatures, might be seen in the XRD profiles. Also minor effects like variations in the local Mo loading and in the bed density might contribute to the observed deviations. Lastly, it might also be that the oscillations originate from actual changes in the phases, since the catalyst is exposed to strongly varying gas

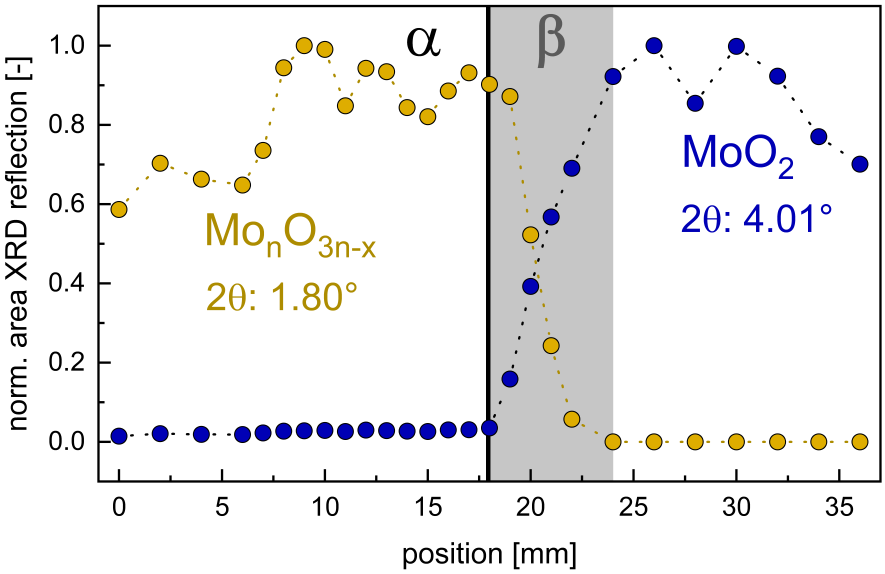

Figure 6.9: Area evaluation of reflections at 1.80° (corresponding to Mo_nO_{3n-x}), as well as at 4.01° (corresponding to MoO_2). The areas were normalized to the maximum area obtained at the respective reflections. α (black line, 18 mm) marks the position of full gas phase oxygen conversion with different catalyst performance before and after. β (grey area, 18 – 24 mm) marks the catalyst bed range where the catalyst undergoes distinct phase transformations. Reaction conditions: $C_2H_6/O_2/N_2$:10/10/80, 515 °C, 1 bar, OD 6 mm/ID 5.6 mm, 38 mm catalyst bed, 15 ml/min, 30 wt% MoO_3/γ-Al_2O_3, beam size 0.5 × 0.5 mm^2 (h × v), 103.4 keV (λ = 0.1199 Å).

compositions along the catalyst bed. For example, in the first bed zone a growth in crystal numbers of a respective Mo_nO_{3n-x} phase could result in changing XRD patterns, while at the end of the bed, beyond position 30 mm, the decreasing trend of the MoO_2 phase could indicate a further reduction of MoO_2.

To illustrate the quality of the obtained data, Rietveld refinement was performed for the XRD pattern at position 26 mm using the monoclinic structure of MoO_2 [ICSD collection code 23722].

A good match is achieved between experimental and calculated patterns (Fig. 6.10), demonstrating high data quality enabling a thorough structure analysis, which is planned for future works.

In summary, *operando* XRD reveals a distinct phase transformation from a mixture of various Mo_nO_{3n-x} phases towards a highly crystalline monoclinic MoO_2

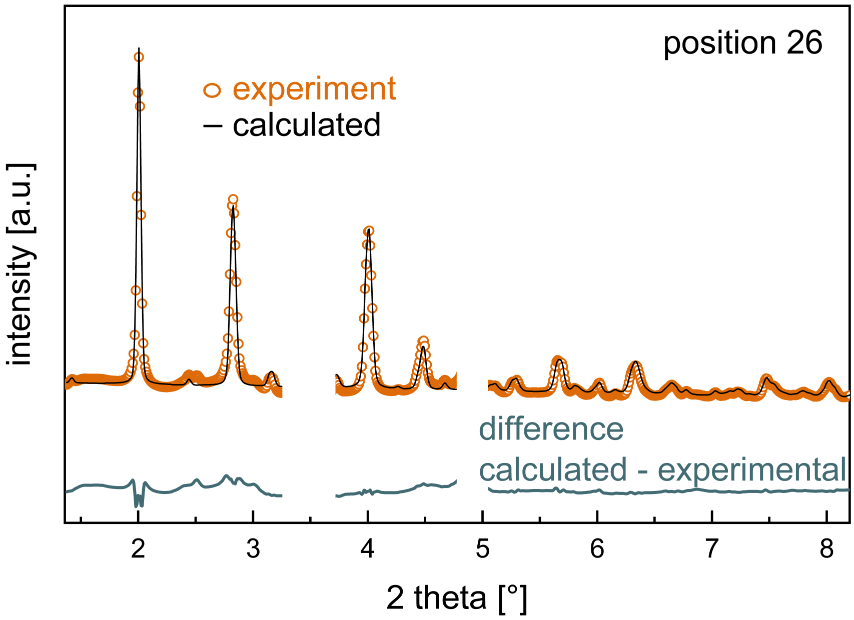

Figure 6.10: Experimental XRD pattern measured *operando* at position 26 mm and results of the Rietveld refinement (experimental data in orange, calculated in black, difference calculated-experimental in grey). The two areas around 3.5° and 4.9° have been masked out of the refinement because of the relatively large contribution from γ-Al_2O_3. Reaction conditions: $C_2H_6/O_2/N_2$:10/10/80, 515 °C, 1 bar, OD 6 mm/ID 5.6 mm, 38 mm catalyst bed, 15 ml/min, 30 wt% MoO_3/γ-Al_2O_3, beam size 0.5 × 0.5 mm^2 (h × v), 103.4 keV (λ = 0.1199 Å).

at full gas phase oxygen conversion. Catalyst reduction downstream of this position, as well as identified phases are in line with color, catalytic performance, and structural observations from XAS, demonstrated in previous chapters.

To summarize, the portfolio of spatially-resolved *operando* synchrotron-based catalyst characterization methods was expanded by means of XRD. Here, for the first time temperature-, gas composition-, and high-energy XRD profile measurements were performed simultaneously through a catalytic fixed-bed. The high data quality enabled quantitative gas and crystalline phase analysis of identified phases which allow to deduce catalyst structure-function relations based on position within the reactor. While the applied test reaction system was essential for well-grounded method development, the methodology represents a promising approach for systematic studies of various reaction systems in the future, and to understand how bulk structural changes affect end of pipe reactor performance.

7 Summary and Future Perspective

In this thesis, new measurement concepts were developed to expand the characterization portfolio for *operando* profile experiments employing synchrotron-based X-ray techniques. *Operando* profiling comprises the simultaneous measurement of spatially-resolved gas composition, gas temperature, and structural information of the catalyst. The main methodological achievements are *operando* profiling using X-Ray Absorption spectroscopy (XAS) and X-Ray Diffraction (XRD).

In order to ensure a systematic development and validation of these complex methodologies, the oxidative dehydrogenation (ODH) of ethane to ethylene over a $MoO_3/\gamma\text{-}Al_2O_3$ catalyst was chosen as a test system. This reaction system possesses optimal characteristics required for well-grounded method development, for example distinct catalyst dynamics in color, performance and structure as well as structural reversibility as a function of the reaction environment. In addition to this, gas phase species are easy to handle, the catalyst is quickly synthesized, stable catalyst performance is reached within a short time, and for a long time on stream.

The synchrotron-based *operando* profile measurements required a complex experimental setup, mainly consisting of a gas dosing system, a profile reactor, gas phase analytics, and a spectroscopic or scattering instrument. Additionally, the setup was equipped with an automated process control system, including heating, gas dosage, reactor positioning and communication with the beamline. Beamlines usually have limited space for large setups and experiments follow strict time constraints. Consequently, the experimental setup must be tailored to match these requirements with an integrated and fully automated design, enabling time-saving setup assembly as well as straightforward sample changeover, operation, and control. Setup operation conditions include a broad range of feasible reaction parameters (e.g., reaction temperature: up to 550 °C, trace heating: 200 °C, pressure: 1 – 10 bar), allowing for probing numerous heterogeneously catalyzed gas-solid or gas-liquid-solid reaction systems. The heart of this setup is the Compact Profile Reactor (CPR) developed by Reacnostics GmbH. The CPR utilizes the capillary sampling technique to resolve spatial gradients and is originally designed for *operando* measurements coupled to spectroscopic measurements such as Raman-spectroscopy in reflection mode or via optical fibers.

To test the new setup before the *operando* profile experiments were conducted at the synchrotron, a set of catalytic performance studies was carried out using three statistically well-defined experimental design plans, comprising 38 concentration and temperature profiles in total. Key objectives were as follows: to verify the catalyst stability with time on stream, to evaluate the reproducibility of the capillary sampling technique and reactor system, to obtain a detailed picture of the catalyst under various reaction conditions, as well as to develop a kinetic model predicting the species profiles for oxidation reactions. The standard reaction mixture was composed of the feed components ethane and oxygen, the main products ethylene and water, as well as the undesired carbon oxides CO and CO_2. By comparing species concentration profiles and corresponding replicate profiles, which were evenly distributed throughout the measurement campaign, a good match is observed. This demonstrates the long-term stability and reproducibility of the profile measurement technique with the CPR for the used reaction system.

To investigate the effects of feed and product concentrations, mixtures of ethane and oxygen were fed to the reactor as well as mixtures of ethylene and oxygen. In both cases, the concentration of oxygen in the feed inlet was varied. The experiments showed a minor effect on ethane and ethylene rates of consumption, indicating that processes related to oxygen are fast. In contrast, different feed compositions for ethane or ethylene, respectively, show a clear impact on oxygen consumption and ethylene formation rates along the catalytic bed. These observations suggest that the rate determining step is related to the ethane or ethylene activation, respectively. With regard to undesired byproduct formation, ethylene was found to mainly contribute to the formation of carbon oxides in the presence of gas phase oxygen. The experimentally obtained profile results support the Mars-van Krevelen (MVK) mechanism, in which all hydrocarbon reactions occur via lattice oxygen and the catalyst participates actively by undergoing cycles of oxidation and reduction. Therefore, the kinetic model to describe and understand this reaction system follows the MVK approach, considering the oxidation state of molybdenum as a parameter. The kinetic model was developed by fitting the complete reactor profiles to the aforementioned reaction mechanism. The resulting coefficients confirm previous observations that the partial pressure of oxygen has only a minor impact on the reoxidation of the catalyst. Additionally, the kinetic model reveals that the reoxidation of the catalyst has a low activation energy, providing evidence that the reoxidation is not the rate determining step. It can be concluded that the exchange between gas phase oxygen and catalyst is a fast process. Hence, as long as the gas phase contains oxygen, the reaction mechanism and color do not change because oxygen can be refilled in the catalyst structure. In contrast, distinct changes of the catalyst in color, performance, and structure are induced by switching from oxidative to non-oxidative reaction conditions. With regard to the spatial profile measurements, this means that full gas phase oxygen conversion must be reached at a certain point along the probed catalyst bed to measure pronounced changes due to catalyst reduction.

By running the reaction with full gas phase oxygen conversion, a color gradient along the axial position of the catalyst bed, i.e., in the flow direction, is observed. Similar colors are visible in different regions along the catalyst bed, which allows separating the bed into three zones. In the first zone, the catalyst possesses a gray color, followed by a dark gray region, and finally, a dark blue/black zone. It is noteworthy, that the second bed zone is particularly short with only a few mm in length. Furthermore, in this second bed zone species concentration profiles reveal full gas phase oxygen conversion, leading to a change in performance from oxidation reactions to steam reforming and water-gas shift, while the temperature profiles show a minor hot spot formation. The observed changes in the reaction mechanism and the color of the catalyst are inseparably linked to structural changes in the catalyst, further addressed through *operando* profile experiments.

The first methodological focus of this work was the development of an experimental approach for simultaneously measuring concentration, temperature, and XAS profiles through a catalyst bed, also referred to as *operando* profiling coupled to XAS. Experiments were carried out at the PETRA III storage ring at DESY using the photon beamline P64 in collaboration between the group of Raimund

Horn at TUHH, the group of Christian Schroer at DESY, and the group of Jan-Dierk Grunwaldt at KIT. To enable XAS measurements in transmission mode, the CPR was modified to the CPR-XAS version. In order to tune photon transmittance through the rather thick CPR reactor tubes to suitable values for XAS experiments, the catalyst weight loading was reduced to 10 wt% MoO_3 (standard is 30 wt%) and the reactor tube wall thickness to 600 μm (standard is 1 mm). The average bulk molybdenum oxidation state profile was deduced from the spatially-resolved Mo K-edge XANES spectra. Similar to the distinction in three catalyst bed zones based on color, XAS spectra show the same zones comparing measured oxidation states present in the catalyst. In the beginning of the catalyst bed (first zone), i.e., in the presence of gas phase oxygen, an almost unchanged molybdenum oxidation state of Mo(VI) is observed while the oxygen partial pressure declines rapidly. This indicates that only a low concentration of oxygen vacancies is formed in the deep bulk, and therefore, reduction and reoxidation are obviously restricted to the near-surface region. At very low oxygen concentrations, oxygen vacancies in the catalyst structure cannot be refilled, resulting in strong and rapid oxidation state changes (second zone) towards a rather constant average molybdenum oxidation state close to Mo(IV) (third zone). Linear combinations of spectra at the beginning and end of the catalyst bed show that the spectrum at the point of full gas phase oxygen conversion (second zone) can be created by mixing the two. Hence, a direct phase transformation without a stable or new intermediate phase is detected via XAS. The experimental molybdenum oxidation state profile was used to validate the predicted local catalyst oxidation state profile by our kinetic model. This provides a quantitative link between catalyst structure and reactivity and allows to include catalyst dynamics in reactor simulations.

The second methodological focus of this work was to extend the previously developed *operando* profile methodology for XAS to XRD. This approach allows the simultaneous measurement of concentration, temperature, and diffraction profiles. Experiments were carried out at the PETRA III storage ring at DESY. Two beamtimes were performed at dedicated photon beamlines optimized for high energy X-ray science (P07, P21.1) in collaboration with the experts on-site. High-energy X-rays are required to provide sufficient penetration power to measure reliably and accurately through the rather thick catalyst bed. In preparation for the beamtime, ex-situ measurements of the CPR reactor tubes were performed to examine data quality for varying reactor inner diameters (constant reactor outer diameter of 6 mm), particle sizes, catalyst materials, as well as different reactor outer diameters. Based on the promising results of the pretests, the CPR-XAS was further modified to the CPR-XRD, allowing the collection of scattered X-ray signals in transmission mode over a certain solid angle range. The optimal size of the reactor opening is determined by various parameters, including photon energies feasible by the beamline, the angular range containing the relevant sample information, and preferably a small opening window for improved sample heating through a direct contact between the reactor tube and oven. By using high-energy X-rays, small reactor windows with a solid angle of $10 - 20°$ are suitable for most catalyst materials. In this work, the feasibility of total scattering was tested in parallel and the reactor was thus cut to a 2θ of up to $32°$. The results obtained from spatially-resolved *operando* XRD, as in the case for XAS, enable likewise the distinction in three catalyst bed zones based on crystallographic similarities. In the presence of gas phase oxygen a rather stable mixture of various Mo_nO_{3n-x} phases exists (first zone), while in the absence of oxygen a highly crystalline monoclinic MoO_2 phase is formed (third zone). The second zone, the particularly short one, starts at the point of full gas phase oxygen conversion and shows the distinct phase transformation from the first to the third zone with characteristic signals from both regions. Interestingly, no gradual reduction is observed despite the strongly varying gas compositions along the catalyst bed until the point of full gas phase oxygen. This is in line with results from *operando* XAS, supporting the assumption that gas phase oxygen exchange is fast and restricted to the near-surface region of the catalyst.

Overall, the new *operando* profile measurement concept has been proven to be a promising approach for systematic catalytic studies, allowing the correlation between catalyst activity and chemical structure in response to the change of local operating conditions. The methodologies demonstrate their strengths by providing numerous insights from different aspects of the chemical system within one profile measurement. In one *operando* profile, a wide range of kinetic and structural data with high quality are measured within short times. The obtained profile results display detailed information on underlying processes related to the catalyst structure, which in combination with theoretical models of the reaction system explain the observed changes in catalyst performance. While the reaction and the catalyst used in this study are only model systems, the methods are transferable to all catalytic reactions that display distinct catalyst dynamics, and thus, offer a broad field of potential applications for deepened investigations of industrially relevant reaction systems. In future works, the achievable information content can be increased further by the simultaneous application of multiple characterization techniques such as XRD, XAS, and Raman spectroscopy, as well as by extending the method to other techniques such as total scattering, small angle X-ray scattering, and related methods. To conclude, the developed *operando* profile methodologies provide a versatile and valuable set of techniques that can significantly contribute to gain a deeper understanding of heterogeneously catalyzed reactions and therefore, can be an asset on the path to a more efficient and sustainable chemical industry.

A Appendix

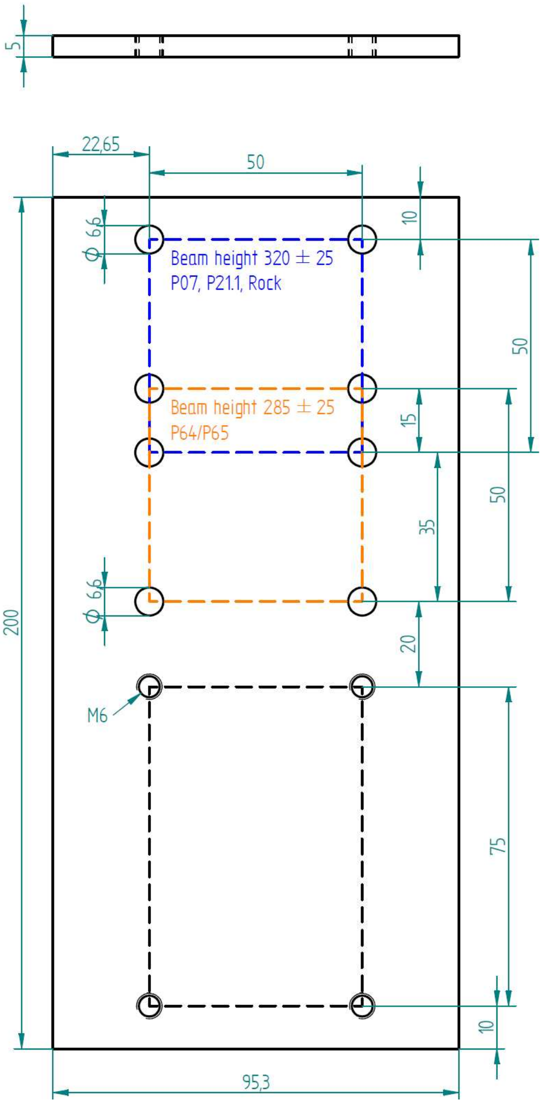

Figure A.1: Adapter Plate 1 facilitates to adjust the reactor window in height to beam positions at several beamlines.

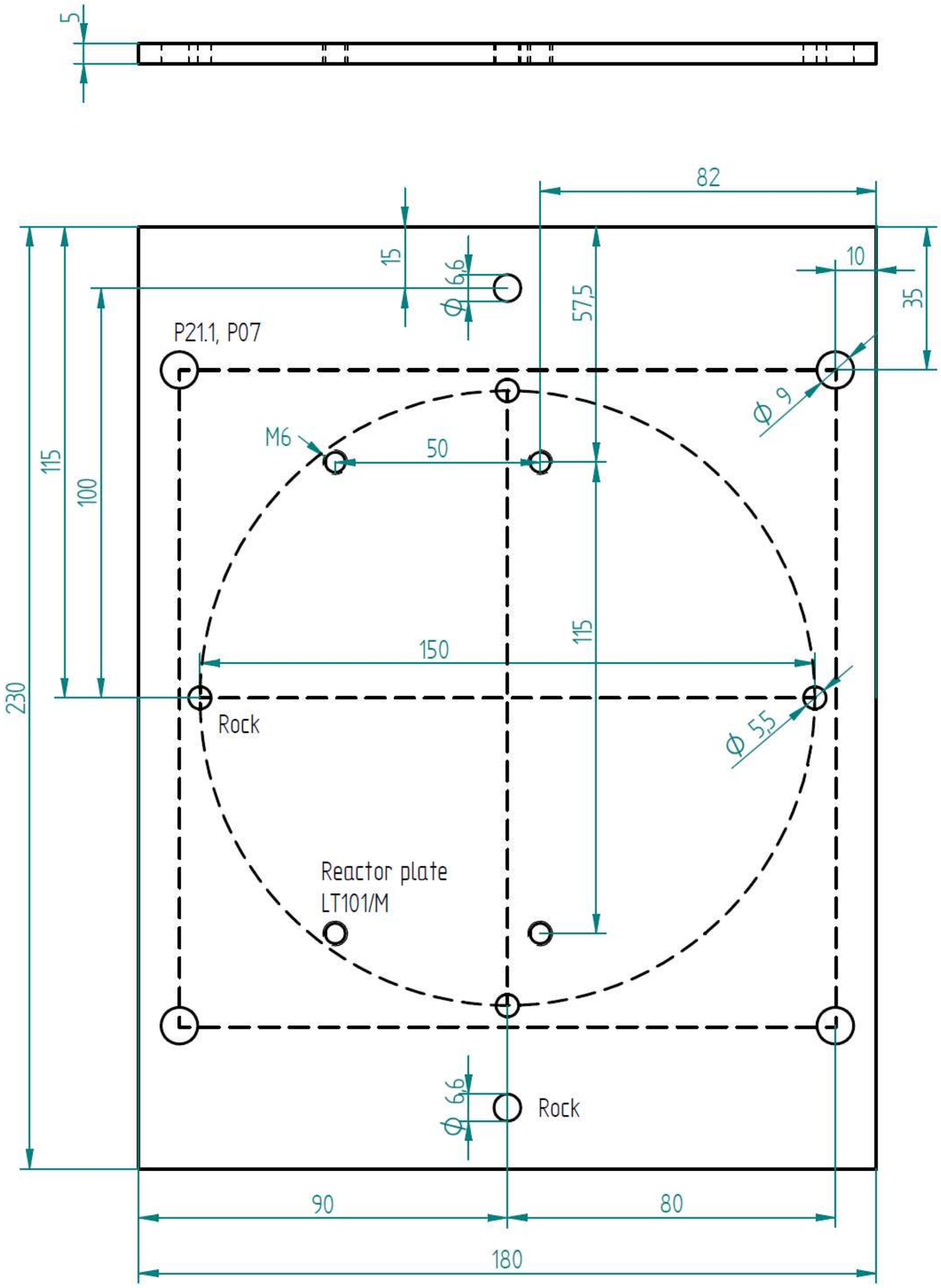

Figure A.2: Adapter Plate 2 facilitates to mount the reactor on the sample stages at beamlines P07/P21.1.

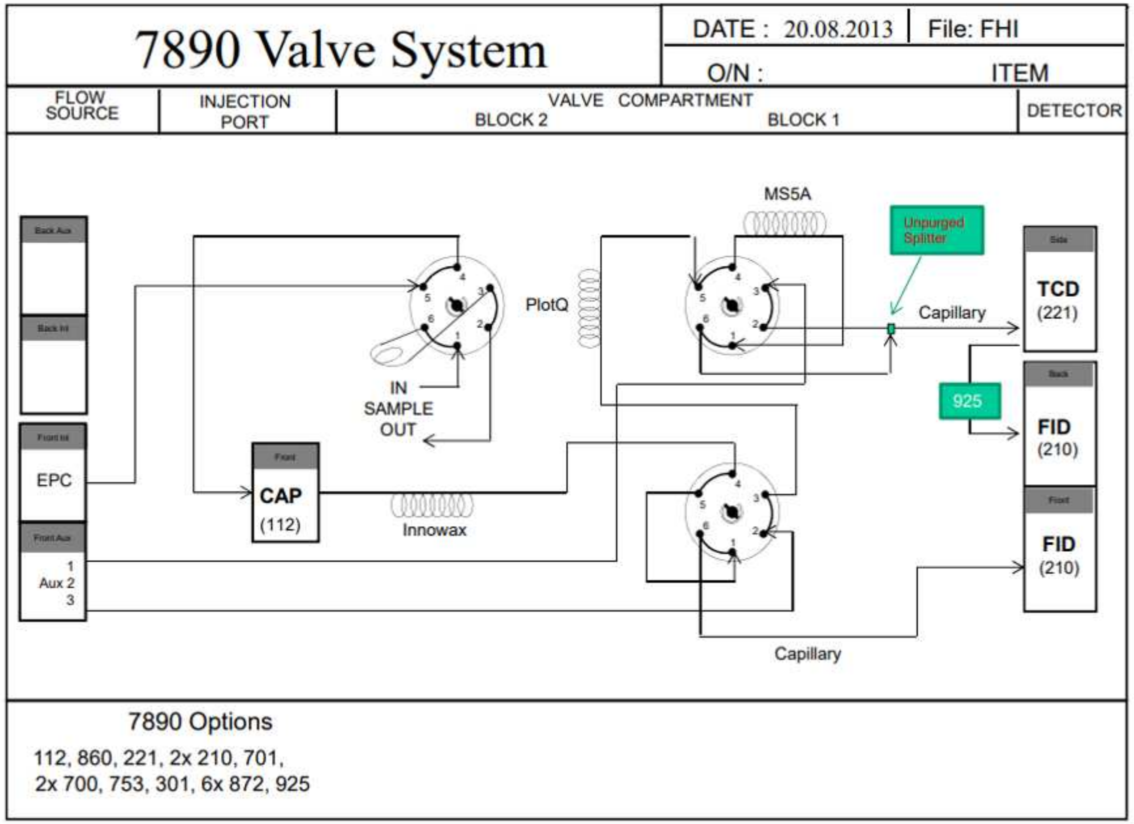

Figure A.3: Flow chart of the valve system installed in the Agilent 7890B GC system.

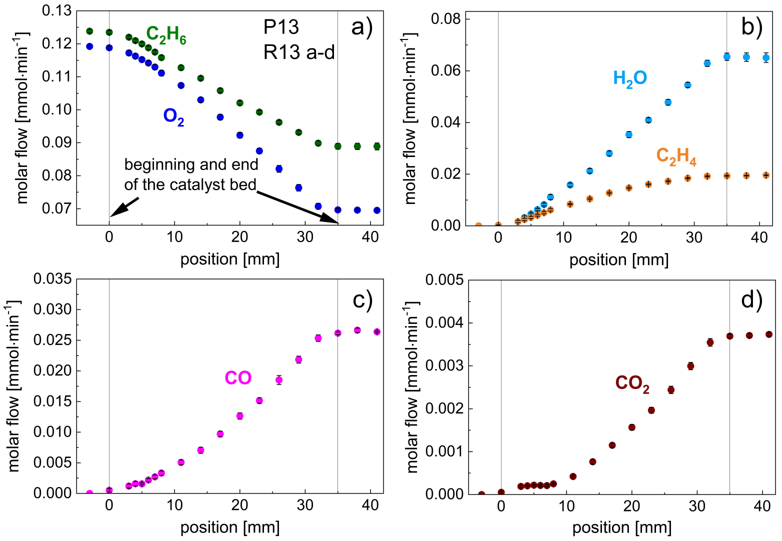

Figure A.4: Profile runs measured in the second measurement design plan are shown of the original profile (P13) with standard errors calculated from its replicates (R13a – d). Profiles of all species are shown in molar flow rates. Reaction conditions: C_2H_6/O_2/inert:10/10/80, 530 °C, 1 bar, 32 mm catalyst bed, 30 ml/min, 30 wt% $MoO_3/\gamma\text{-}Al_2O_3$.

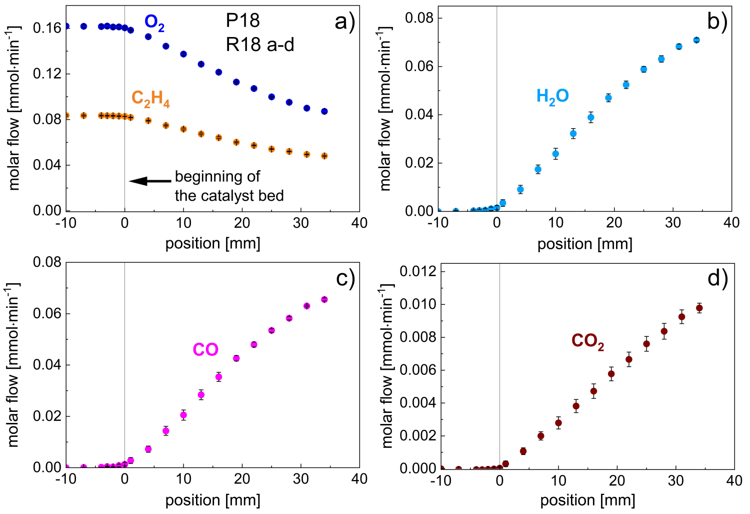

Figure A.5: Profile runs measured in the second measurement design plan of ethylene are shown of the original profile (P18) with standard errors calculated from its replicates (R18a-d). Profiles of all species are shown in molar flow rates. Reaction conditions: C_2H_4/O_2/inert:5/10/85, 530 °C, 1 bar, 32 mm catalyst bed, 40 ml/min, 30 wt% $MoO_3/\gamma\text{-}Al_2O_3$.

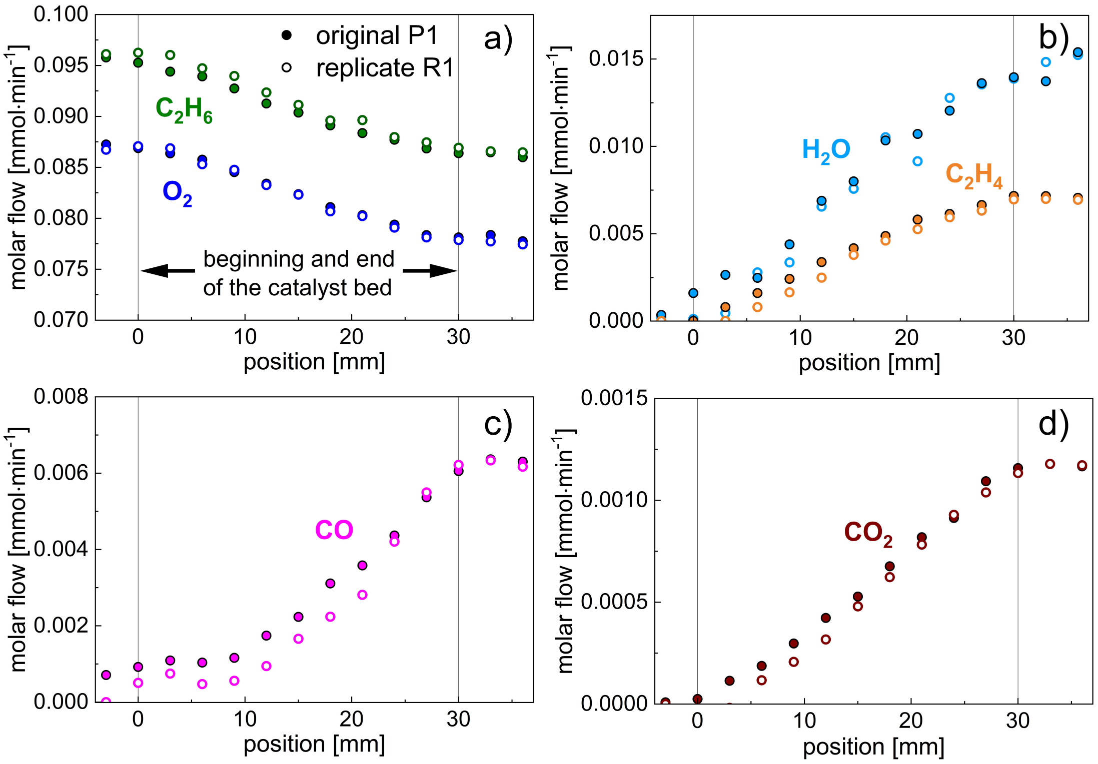

Figure A.6: Profile runs measured in the first measurement design plan are shown of the original profile (P1) and its replicate (R1a). a-d) Profiles of all species are shown in molar flow rates. Reaction conditions: C_2H_6/O_2:7.5/7.5, 480 °C, 1 bar, 30 mm catalyst bed, 30 ml/min, 30 wt% $MoO_3/\gamma\text{-}Al_2O_3$.

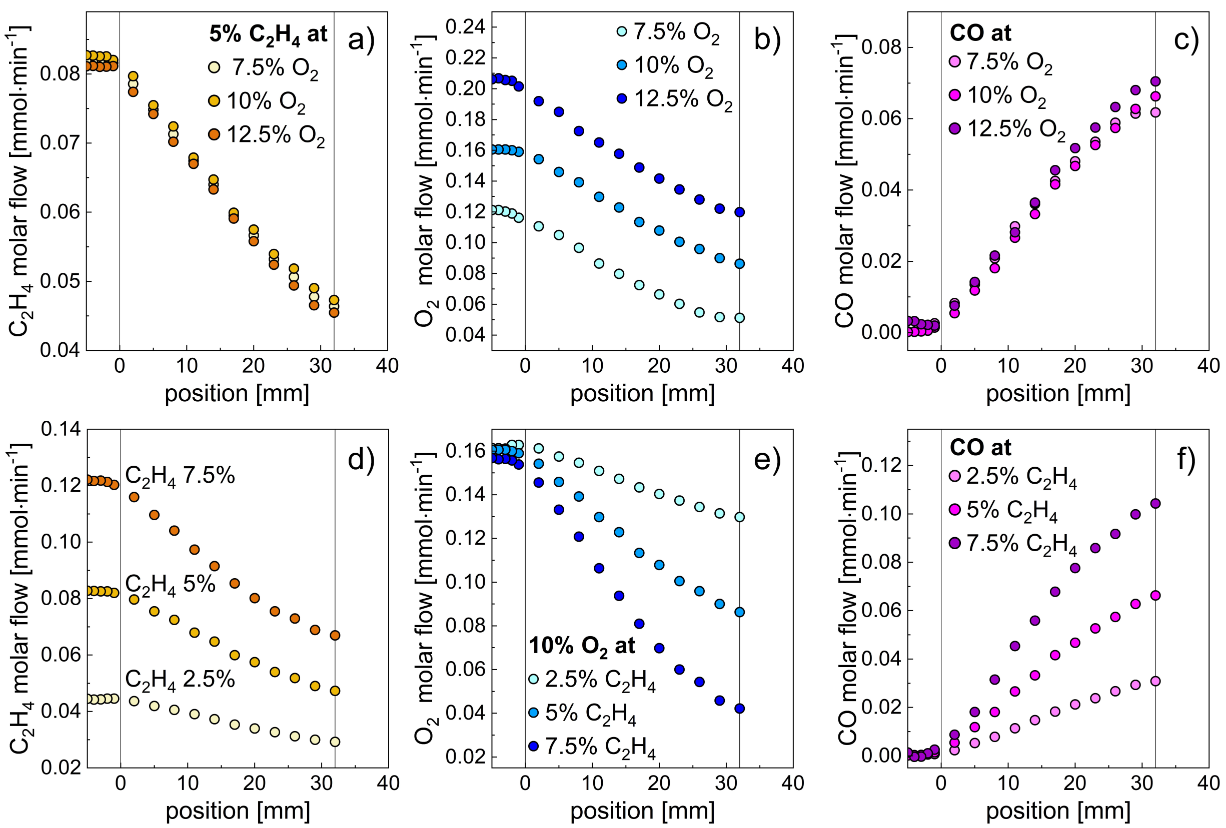

Figure A.7: Feed variations of O_2 (1_{st} row) at reactant concentrations of 7.5, 10 and 12.5 % and C_2H_4 (2_{nd} row) at reactant concentrations of 2.5, 5 and 7.5 % (P15, P17 – 19, P21). All percentage values are in a molar base. (a,d) C_2H_4; (b,e) O_2; (c,f) CO concentration profiles. Reaction conditions: 530 °C, 1 bar, 32 mm catalyst bed, 40 ml/min, 30 wt% $MoO_3/\gamma\text{-}Al_2O_3$.

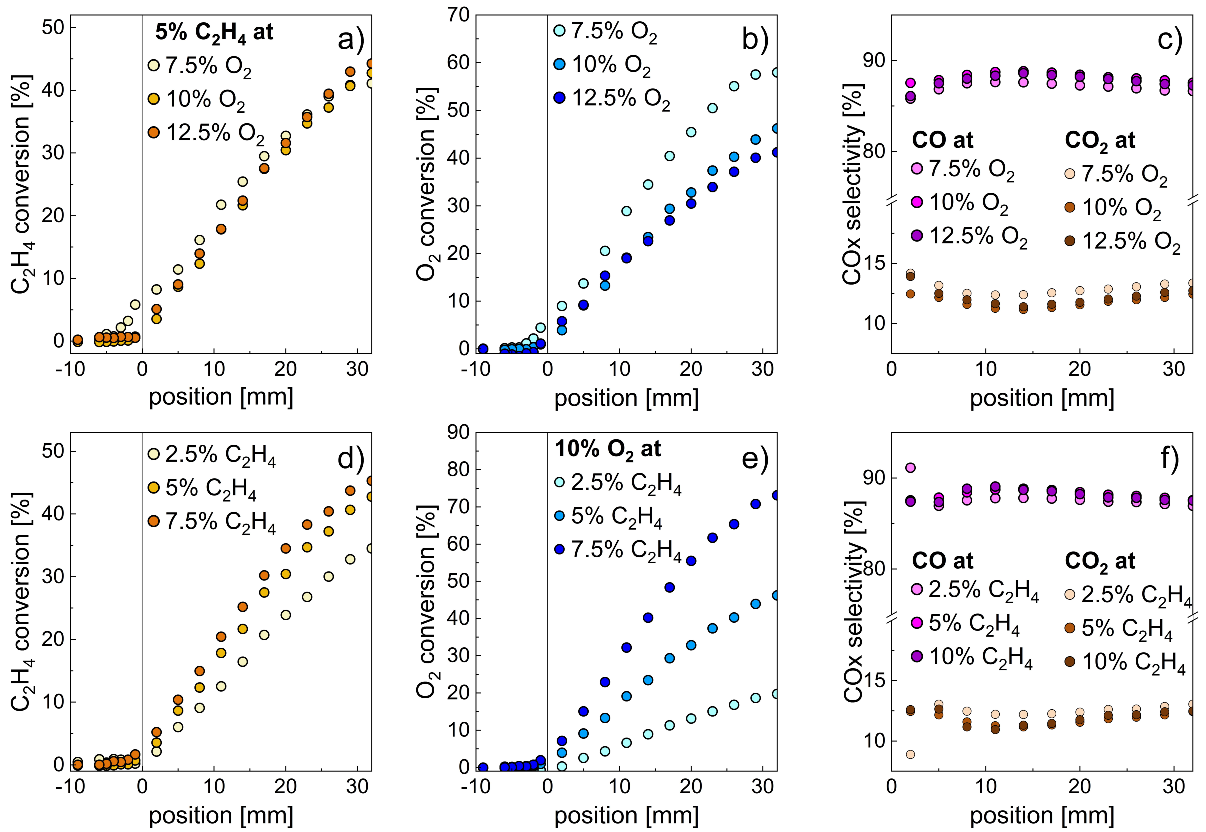

Figure A.8: Feed variations of O_2 (1_{st} row) at reactant concentrations of 7.5, 10 and 12.5 % and C_2H_4 (2_{nd} row) at reactant concentrations of 2.5, 5 and 7.5 % (P15, P17 – 19, P21). All percentage values are in a molar base. (a,d) C_2H_4; (b,e) O_2 conversion profiles. (c,f) CO selectivity profiles. Reaction conditions: 530 °C, 1 bar, 32 mm catalyst bed, 40 ml/min, 30 wt% $MoO_3/\gamma\text{-}Al_2O_3$.

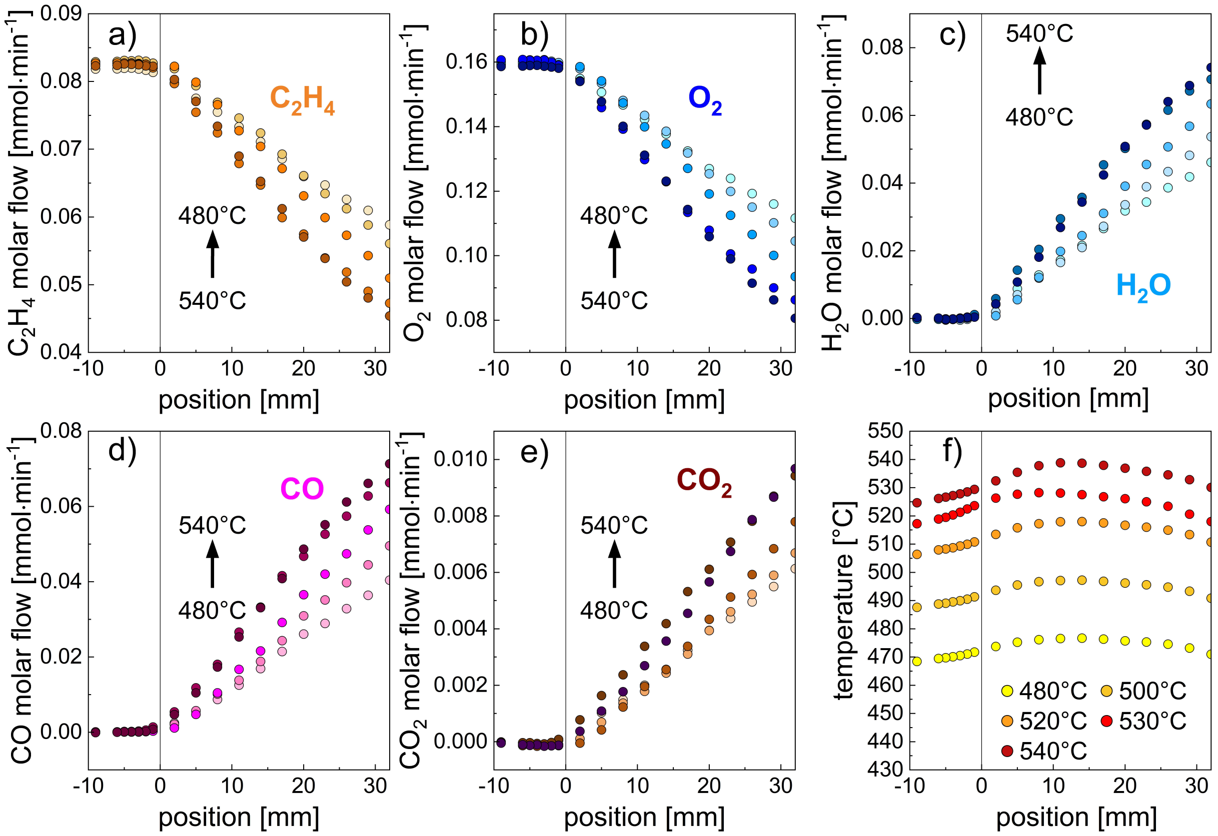

Figure A.9: Species concentration (a-e) and temperature profiles (f) for all components measured at 480 (T18a), 500 (18b), 520 (T18c), 530 (T18) and 540 °C (T18d) obtained in the C_2H_4 measurement plan. Reaction conditions: 530 °C, 1 bar, 32 mm catalyst bed, 40 ml/min, 30 wt% MoO_3/γ-Al_2O_3.

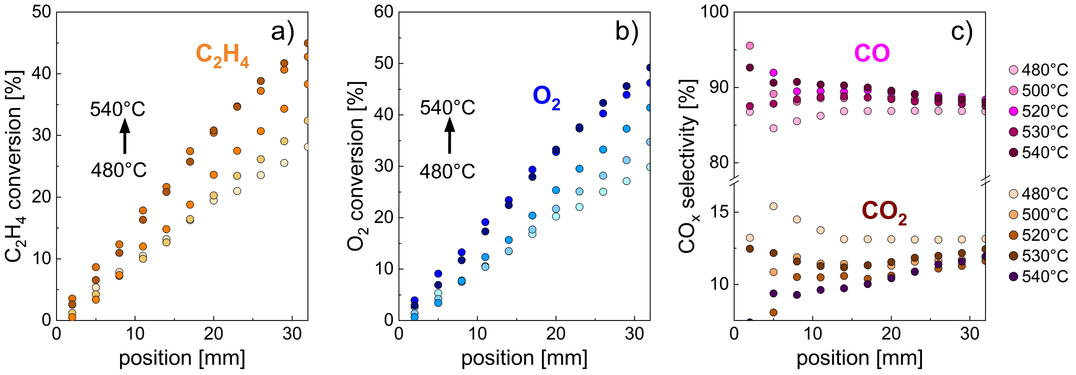

Figure A.10: C_2H_4 (a), O_2 (b) conversion profiles and CO (c) selectivity profiles measured at 480 (T18a), 500 (18b), 520 (T18c), 530 (T18) and 540 °C (T18d) obtained in the C_2H_4 measurement plan. Reaction conditions: 530 °C, 1 bar, 32 mm catalyst bed, 40 ml/min, 30 wt% $MoO_3/\gamma\text{-}Al_2O_3$.

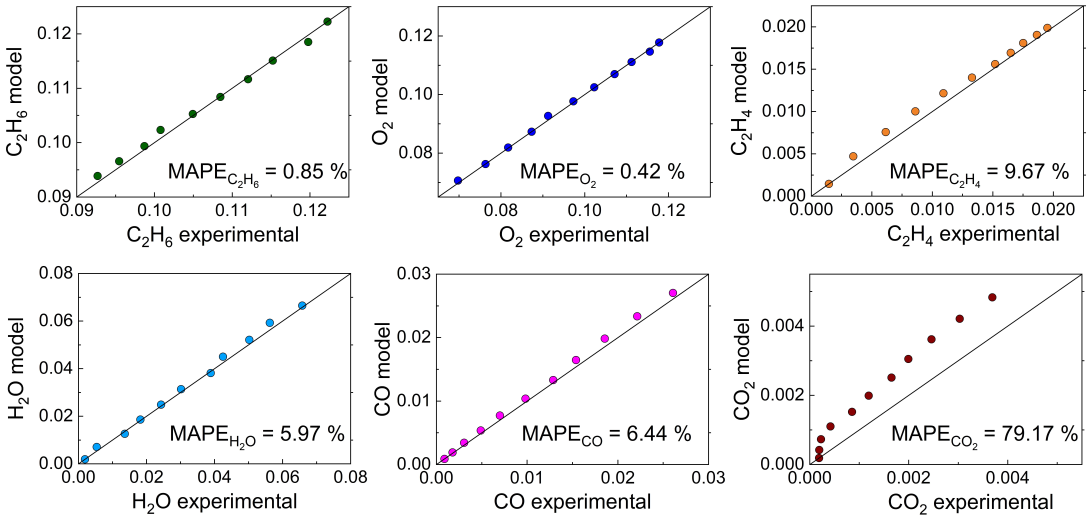

Figure A.11: Predicted components versus corresponding experimental results (P13) are shown (parity plots). Reaction conditions: C_2H_6/O_2/inert:10/10/80, 530 °C, 1 bar, 32 mm catalyst bed, 30 ml/min, 30 wt% $MoO_3/\gamma\text{-}Al_2O_3$.

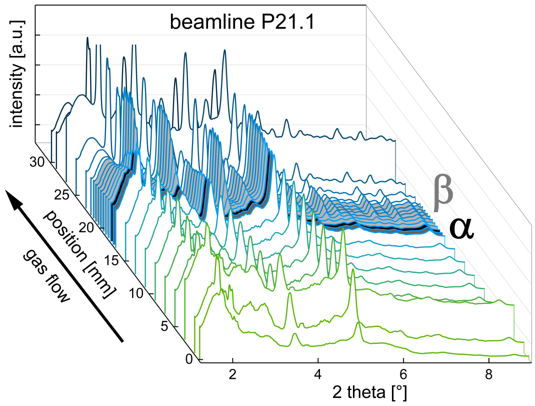

Figure A.12: *Operando* XRD profile simultaneously measured with temperature and gas concentration profiles at beamline P21.1, PETRA III (Hamburg, Germany) during ethane ODH. Alpha (black colored pattern, 18 mm) marks the position of full gas phase oxygen conversion with different catalyst performance before and after. Beta (grey colored patterns, 17.5 – 21.5 mm) marks the catalyst bed range where the catalyst undergoes distinct phase transformations. Reaction conditions: $C_2H_6/O_2/N_2$:10/10/80, 515 °C, 1 bar, OD 6 mm/ID 5.0 mm, 30 mm catalyst bed, 12 ml/min, 30 wt% $MoO_3/\gamma\text{-}Al_2O_3$, beam size 0.5 × 0.5 mm^2 (h × v), 101.6 keV (λ = 0.1220 Å).

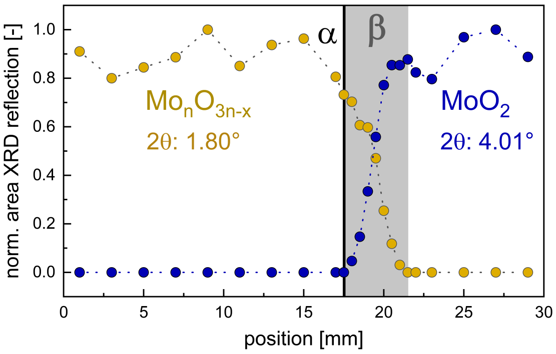

Figure A.13: Area evaluation of reflections at 1.80° (corresponding to Mo_nO_{3n-x}), as well as at 4.01° (corresponding to MoO_2) from P21.1 data. The areas were normalized to the maximum area obtained at the respective reflections. Alpha (black line, 18 mm) marks the position of full gas phase oxygen conversion with different catalyst performance before and after. Beta (grey area, 17.5 – 21.5 mm) marks the catalyst bed range where the catalyst undergoes distinct phase transformations. Reaction conditions: $C_2H_6/O_2/N_2$:10/10/80, 515 °C, 1 bar, OD 6 mm/ID 5.0 mm, 30 mm catalyst bed, 12 ml/min, 30 wt% $MoO_3/\gamma\text{-}Al_2O_3$, beam size 0.5 × 0.5 mm^2 (h × v), 101.6 keV.

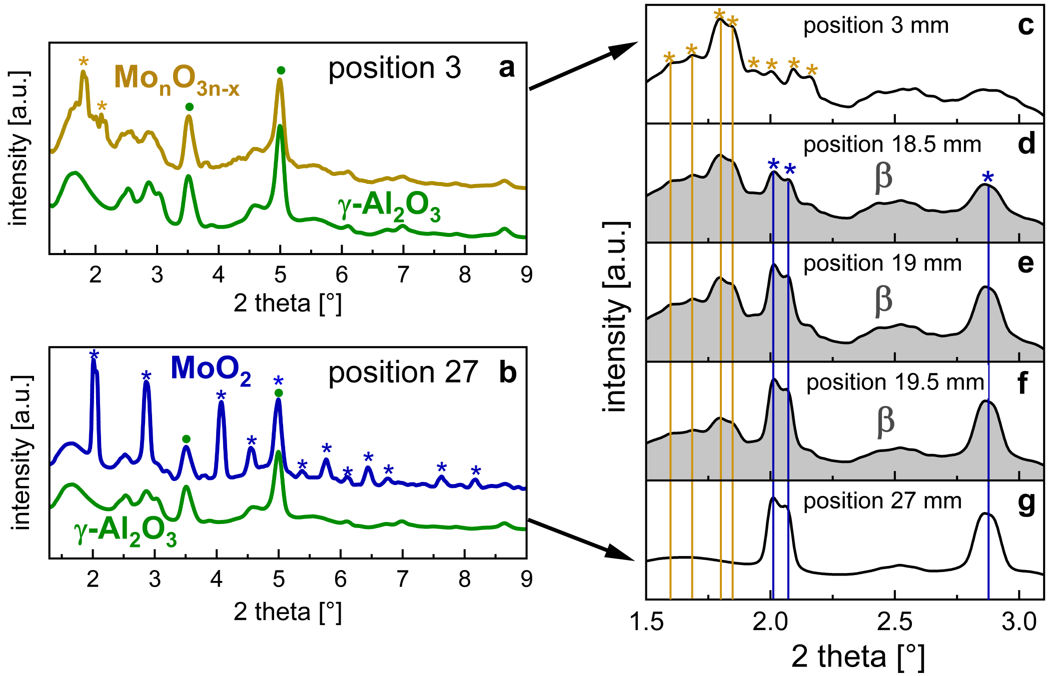

Figure A.14: XRD patterns measured *operando* at beamline P21.1, PETRA III (Hamburg, Germany). a, c) Diffractogram at the beginning of the catalyst bed (yellow, 3 mm, before) in the presence of gas phase oxygen; b, g) Diffractogram at the end of the catalyst bed (blue, 27 mm, beyond) in the absence of gas phase oxygen. a, b) Each pattern contains signal contributions from fused silica and alumina. A corresponding pattern is shown in green. d – f): XRD patterns measured at the catalyst bed position (17.5 – 21.5 mm). Reaction conditions: $C_2H_6/O_2/N_2$:10/10/80, 515 °C, 1 bar, OD 6 mm/ID 5.0 mm, 30 mm catalyst bed, 12 ml/min, 30 wt% $MoO_3/\gamma\text{-}Al_2O_3$, beam size 0.5 × 0.5 mm^2 (h × v), 101.6 keV ($\lambda = 0.1220$ Å).

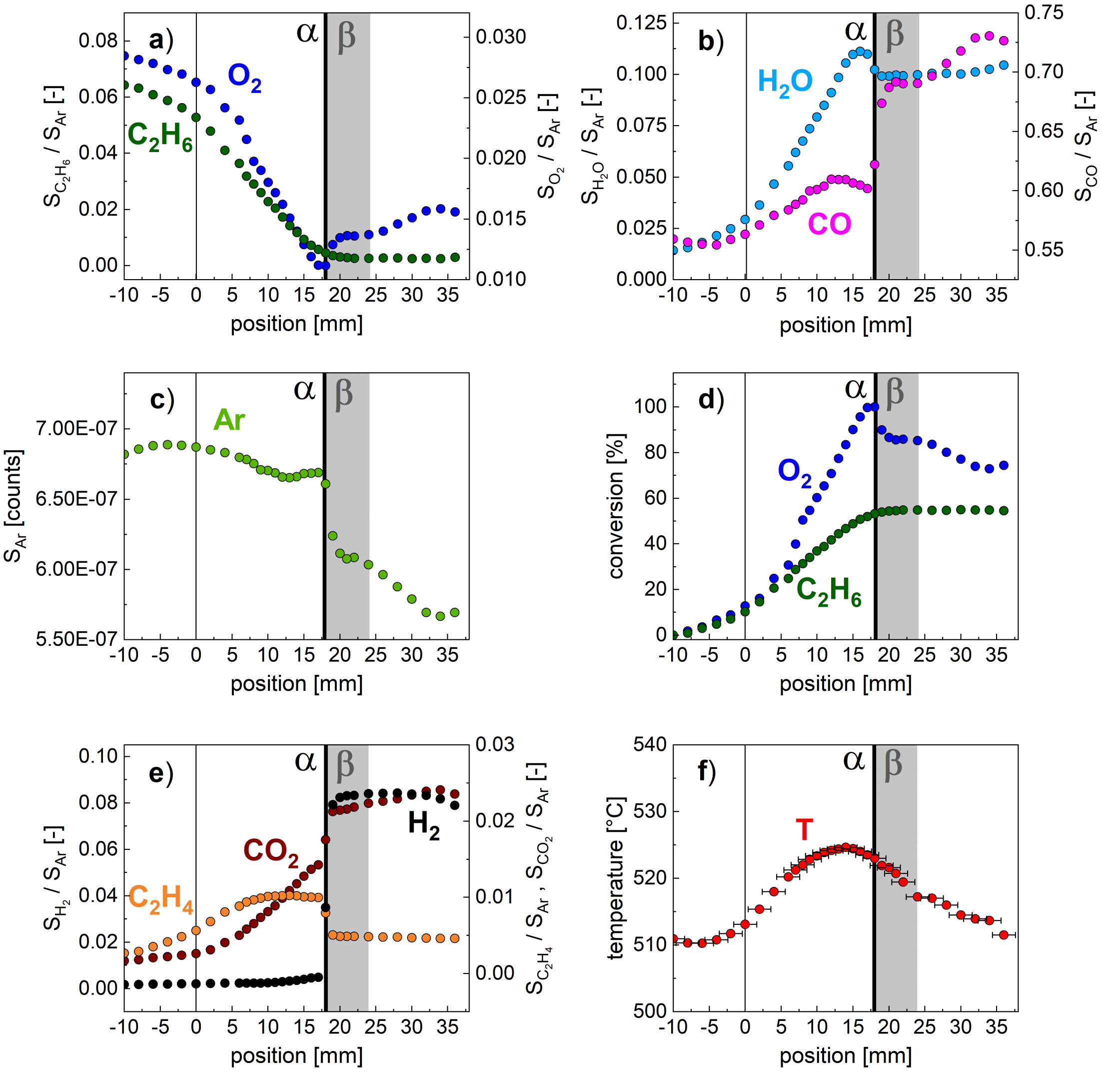

Figure A.15: Catalyst activity profiles measured *operando* at beamline P07 using a MS (a – f). Signal ratios of C_2H_6, O_2 (a), H_2O, CO (b), C_2H_4, H_2, CO_2 (c), inert Ar (d); conversion profiles of C_2H_6 and O_2 (e); and the temperature profile measured in the center of the catalyst bed (f). Alpha (black line, 18 mm) marks the position of full gas phase oxygen conversion with different catalyst performance before and after. Beta (gray area, 17.5 – 21.5 mm) marks the catalyst bed range where the catalyst undergoes distinct phase transformations. Reaction conditions: C_2H_6/O_2/inert:10/10/80, 515 °C, 1 bar, OD 6 mm/ID 5.6 mm, 38 mm catalyst bed, 15 ml/min, 30 wt% $MoO_3/\gamma\text{-}Al_2O_3$.

List of Symbols

Latin symbols:

Variable	Meaning	Unit
a	slope	$-$
A_m	atomic mass	kg
k_j	forward reaction rate constant reaction j	$\frac{1}{s}\left(\frac{m^2}{mol}\right)^{n-1}$
$\dot{n}$	molar flow rate	$\frac{mol}{s}$
p	pressure	Pa
$R_{i,net}$	weight base net rate of consumption/ production of component i	$\frac{mol}{kg \cdot s}$
r_j	reaction rate of a specific reaction j	$\frac{mol}{kg \cdot s}$
q	length of the reciprocal lattice vector	Å^{-1}
S	selectivity	$-$
t	time	s
T	temperature	K
X	conversion	$-$
Y	yield	$-$
Z	atomic number	$-$

Greek Symbols:

Variable	Meaning	Value
α	color inflection point in the catalyst bed	mm
β	transition zone in the catalyst bed from an oxidized to reduced catalyst state	mm
θ_{ox}	fraction of oxidized catalyst sites	$-$
θ_{red}	fraction of reduced catalyst sites	$-$
θ	angle	$^\circ$

λ	wavelength	m
μ	absorption coefficient	$\frac{1}{cm}$
μ_m	mass absorption coefficient	$\frac{cm^2}{g}$
ν	stoichiometric coefficient	$-$
ρ	density	$\frac{kg}{m^3}$

Fundamental Constants:

Constants	**Meaning**	**Value**
R	universal gas constant	$8.31451\ \frac{J}{mol\ K}$
π	circle constant	3.1415

List of Abbreviations

.poni	Point Of Normal Incidence
AHM	Ammonium Heptamolybdate Tetrahydrate
BW	Bandwidth
CMRs	Capillary Micro-Reactors
CPO	Catalytic Partial Oxidation
CPR	Compact Profile Reactor
ESRF	European Synchrotron Radiation Facility
EXAFS	Extended X-ray Absorption Fine Structure Spectroscopy
FID	Flammable Ionization Detector
FWHM	Full Width at Half Maximum
GC	Gas Chromatography
GHSV	Gas Hourly Space Velocity
ID	Inner Diameter
IP	Color Inflection Point
LCA	Linear Combination Analysis
MAPE	Mean Absolute Percentage Error

MID	Multiple Ion Detection
MS	Mass Spectrometry
MVK	Mars-Van Krevelen
OD	Outer Diameter
ODEs	Ordinary Differential Equations
ODH	Oxidative Dehydrogenation
PLOT	Porous Layer Open Tubular
QW	Quartz Wool
RLP	Reciprocal Lattice Points
SPACI-FB	Spatially Resolved Capillary Inlet Reactor System for Fixed Beds
TCD	Thermal Conductivity Detector
WGSR	Water-Gas Shift Reaction
XANES	X-ray Absorption Near Edge Spectroscopy
XAS	X-ray Absorption Spectroscopy
XRD	X-ray Diffraction

List of Figures

List of Tables

Bibliography

[1] G. Eigenberger, W. Ruppel, Catalytic fixed-bed reactors, in: Ullmann's Encyclopedia of Industrial Chemistry, Wiley-VCH Verlag GmbH & Co. KGaA, Weinheim, Germany, 2000. `doi:10.1002/14356007.b04_199.pub2`.

[2] H. F. Rase, Fixed-Bed Reactor Design and Diagnostics, Elsevier, 1990. `doi:10.1016/C2013-0-04268-5`.

[3] R. Horn, Reaktoren für Fluid-Feststoff-Reaktionen: Festbettreaktoren, in: W. Reschetilowski (Ed.), Handbuch Chemische Reaktoren, Springer Berlin Heidelberg, 2020, pp. 1–70. `doi:10.1007/978-3-662-56444-8_22-1`.

[4] Website hte: The High Throughput Experimentation, High throughput reactor systems for catalyst testing workflows (25.07.2022).
URL `https://www.hte-company.com/en/solutions/technology-solutions-ts/high-throughput-reactor-systems`

[5] D. Farrusseng, High-throughput heterogeneous catalysis, Surface Science Reports 63 (11) (2008) 487–513. `doi:10.1016/j.surfrep.2008.09.001`.

[6] A. Hagmeyer, P. Strasser, A. F. Volpe, High-Throughput Screening in Heterogeneous Catalysis, Wiley, 2004. `doi:10.1002/3527604103`.

[7] R. Schlögl, Heterogeneous Catalysis, Angewandte Chemie (International ed. in English) 54 (11) (2015) 3465–3520. `doi:10.1002/anie.201410738`.

[8] K. F. Kalz, R. Kraehnert, M. Dvoyashkin, R. Dittmeyer, R. Gläser, U. Krewer, K. Reuter, J.-D. Grunwaldt, Future challenges in heterogeneous catalysis: Understanding catalysts under dynamic reaction conditions, ChemCatChem 9 (1) (2017) 17–29. `doi:10.1002/cctc.201600996`.

[9] M. A. Bañares, Operando methodology: combination of in situ spectroscopy and simultaneous activity measurements under catalytic reaction conditions, Catalysis Today 100 (1-2) (2005) 71–77. `doi:10.1016/j.cattod.2004.12.017`.

[10] J. Frenken, Operando Research in Heterogeneous Catalysis, Vol. v.114 of Springer Series in Chemical Physics Ser, Springer International Publishing, Cham, 2017.

[11] H. Topsøe, Developments in operando studies and in situ characterization of heterogeneous catalysts, Journal of Catalysis 216 (1-2) (2003) 155–164. `doi:10.1016/S0021-9517(02)00133-1`.

[12] B. M. Weckhuysen, Operando spectroscopy: fundamental and technical aspects of spectroscopy of catalysts under working conditions, Physical Chemistry Chemical Physics 5 (20) (2003) 1. `doi:10.1039/B309654H`.

[13] A. M. Beale, A. M. J. van der Eerden, K. Kervinen, M. A. Newton, B. M. Weckhuysen, Adding a third dimension to operando spectroscopy: a combined UV-Vis, Raman and XAFS setup to study heterogeneous catalysts under working conditions, Chemical communications (Cambridge, England) (24) (2005) 3015–3017. `doi:10.1039/B504027B`.

[14] K. H. Cats, B. M. Weckhuysen, Combined operando X-ray Diffraction/Raman Spectroscopy of catalytic solids in the laboratory: The Co/TiO2 fischer-tropsch synthesis catalyst showcase, ChemCatChem 8 (8) (2016) 1531–1542. `doi:10.1002/cctc.201600074`.

[15] T. Günter, D. E. Doronkin, H. W. P. Carvalho, M. Casapu, J.-D. Grunwaldt, HERFD-XANES and XES as complementary operando tools for monitoring the structure of Cu-based zeolite catalysts during NOx-removal by ammonia SCR (2016). `doi:10.5445/IR/1000068659`.

[16] F. Meirer, B. M. Weckhuysen, Spatial and temporal exploration of heterogeneous catalysts with synchrotron radiation, Nature Reviews Materials 3 (9) (2018) 324–340. `doi:10.1038/s41578-018-0044-5`.

[17] S. J. Tinnemans, J. G. Mesu, K. Kervinen, T. Visser, T. A. Nijhuis, A. M. Beale, D. E. Keller, A. M. van der Eerden, B. M. Weckhuysen, Combining operando techniques in one spectroscopic-reaction cell: New opportunities for elucidating the active site and related reaction mechanism in catalysis, Catalysis Today 113 (1-2) (2006) 3–15. `doi:10.1016/j.cattod.2005.11.076`.

[18] L. Grajciar, C. J. Heard, A. A. Bondarenko, M. V. Polynski, J. Meeprasert, E. A. Pidko, P. Nachtigall, Towards operando computational modeling in heterogeneous catalysis, Chemical Society reviews 47 (22) (2018) 8307–8348. `doi:10.1039/c8cs00398j`.

[19] X. Shi, X. Lin, R. Luo, S. Wu, L. Li, Z.-J. Zhao, J. Gong, Dynamics of heterogeneous catalytic processes at operando conditions, JACS Au 1 (12) (2021) 2100–2120. `doi:10.1021/jacsau.1c00355`.

[20] M. A. Newton, Dynamic adsorbate/reaction induced structural change of supported metal nanoparticles: heterogeneous catalysis and beyond, Chemical Society reviews 37 (12) (2008) 2644–2657. `doi:10.1039/b707746g`.

[21] Y. Zhou, C. Jin, Y. Li, W. Shen, Dynamic behavior of metal nanoparticles for catalysis, Nano Today 20 (2018) 101–120. `doi:10.1016/j.nantod.2018.04.005`.

[22] M. Geske, O. Korup, R. Horn, Resolving kinetics and dynamics of a catalytic reaction inside a fixed bed reactor by combined kinetic and spectroscopic profiling, Catal. Sci. Technol. 3 (1) (2013) 169–175. `doi:10.1039/C2CY20489D`.

[23] A. Gaur, M. Schumann, K. V. Raun, M. Stehle, P. Beato, A. D. Jensen, J. Grunwaldt, M. Høj, Operando XAS/XRD and Raman spectroscopic study of structural changes of the iron molybdate catalyst during selective oxidation of methanol, ChemCatChem 11 (19) (2019) 4871–4883. `doi:10.1002/cctc.201901025`.

[24] K. Morgan, J. Touitou, J.-S. Choi, C. Coney, C. Hardacre, J. A. Pihl, C. E. Stere, M.-Y. Kim, C. Stewart, A. Goguet, W. P. Partridge, Evolution and enabling capabilities of spatially resolved techniques for the characterization of heterogeneously catalyzed reactions, ACS Catalysis 6 (2) (2016) 1356–1381. `doi:10.1021/acscatal.5b02602`.

[25] A. Urakawa, A. Baiker, Space-resolved profiling relevant in heterogeneous catalysis, Topics in Catalysis 52 (10) (2009) 1312–1322. `doi:10.1007/s11244-009-9312-3`.

[26] J.-D. Grunwaldt, B. Kimmerle, A. Baiker, P. Boye, C. G. Schroer, P. Glatzel, C. N. Borca, F. Beckmann, Catalysts at work: From integral to spatially resolved X-ray absorption spectroscopy, Catalysis Today 145 (3-4) (2009) 267–278. `doi:10.1016/j.cattod.2008.11.002`.

[27] S. Alizadehfanaloo, J. Garrevoet, M. Seyrich, V. Murzin, J. Becher, D. E. Doronkin, T. L. Sheppard, J. D. Grunwaldt, C. G. Schroer, A. Schropp, Tracking dynamic structural changes in catalysis by rapid 2D-XANES microscopy, Journal of synchrotron radiation 28 (Pt 5) (2021) 1518–1527. `doi:10.1107/S1600577521007074`.

[28] J. Becher, D. F. Sanchez, D. E. Doronkin, D. Zengel, D. M. Meira, S. Pascarelli, J.-D. Grunwaldt, T. L. Sheppard, Chemical gradients in automotive Cu-SSZ-13 catalysts for NOx removal revealed by operando X-ray spectrotomography, Nature Catalysis 4 (1) (2021) 46–53. `doi:10.1038/s41929-020-00552-3`.

[29] J.-D. Grunwaldt, S. Hannemann, C. G. Schroer, A. Baiker, 2D-mapping of the catalyst structure inside a catalytic microreactor at work: partial oxidation of methane over Rh/Al2O3, The journal of physical chemistry. B 110 (17) (2006) 8674–8680. `doi:10.1021/jp060371n`.

[30] F. Maurer, J. Jelic, J. Wang, A. Gänzler, P. Dolcet, C. Wöll, Y. Wang, F. Studt, M. Casapu, J.-D. Grunwaldt, Tracking the formation, fate and consequence for catalytic activity of Pt single sites on CeO2, Nature Catalysis 3 (10) (2020) 824–833. `doi:10.1038/s41929-020-00508-7`.

[31] D. Matras, A. Vamvakeros, S. D. M. Jacques, M. Di Michiel, V. Middelkoop, I. Z. Ismagilov, E. V. Matus, V. V. Kuznetsov, R. J. Cernik, A. M. Beale, Multi-length scale 5D diffraction imaging of Ni–Pd/CeO2 –ZrO2 /Al2O3 catalyst during partial oxidation of methane, Journal of Materials Chemistry A 9 (18) (2021) 11331–11346. `doi:10.1039/D1TA01464A`.

[32] M. G. O'Brien, A. M. Beale, S. D. M. Jacques, M. Di Michiel, B. M. Weckhuysen, Spatiotemporal multitechnique imaging of a catalytic solid in action: Phase variation and volatilization during molybdenum oxide reduction, ChemCatChem 1 (1) (2009) 99–102. `doi:10.1002/cctc.200900042`.

[33] A. Vamvakeros, S. D. M. Jacques, M. Di Michiel, D. Matras, V. Middelkoop, I. Z. Ismagilov, E. V. Matus, V. V. Kuznetsov, J. Drnec, P. Senecal, A. M. Beale, 5D operando tomographic diffraction imaging of a catalyst bed, Nature communications 9 (1) (2018) 4751. `doi:10.1038/s41467-018-07046-8`.

[34] A. Vamvakeros, D. Matras, S. D. Jacques, M. Di Michiel, S. W. Price, P. Senecal, M. A. Aran, V. Middelkoop, G. B. Stenning, J. F. W. Mosselmans, I. Z. Ismagilov, A. M. Beale, Real-time multi-length scale chemical tomography of fixed bed reactors during the oxidative coupling of methane reaction, Journal of Catalysis 386 (2020) 39–52. `doi:10.1016/j.jcat.2020.03.027`.

[35] D. S. Wragg, M. G. O'Brien, F. L. Bleken, M. Di Michiel, U. Olsbye, H. Fjellvåg, Watching the methanol-to-olefin process with time- and space-resolved high-energy operando X-ray diffraction, Angewandte Chemie (International ed. in English) 51 (32) (2012) 7956–7959. `doi:10.1002/anie.201203462`.

[36] R. Horn, N. J. Degenstein, K. A. Williams, L. D. Schmidt, Spatial and temporal profiles in millisecond partial oxidation processes, Catalysis Letters 110 (3-4) (2006) 169–178. `doi:10.1007/s10562-006-0117-8`.

[37] R. Horn, K. Williams, N. Degenstein, L. Schmidt, Syngas by catalytic partial oxidation of methane on rhodium: Mechanistic conclusions from spatially resolved measurements and numerical simulations, Journal of Catalysis 242 (1) (2006) 92–102. `doi:10.1016/j.jcat.2006.05.008`.

[38] M. Wolf, N. Raman, N. Taccardi, R. Horn, M. Haumann, P. Wasserscheid, Capturing spatially resolved kinetic data and coking of Ga-Pt supported catalytically active liquid metal solutions during propane dehydrogenation in situ, Faraday discussions 229 (2021) 359–377. `doi:10.1039/d0fd00010h`.

[39] H. Schwarz, Y. Dong, R. Horn, Catalytic methane combustion on a Pt gauze: Laser-Induced Fluorescence Spectroscopy, species profiles, and simulations, Chemical Engineering & Technology 39 (11) (2016) 2011–2019. `doi:10.1002/ceat.201600286`.

[40] C. Stewart, E. K. Gibson, K. Morgan, G. Cibin, A. J. Dent, C. Hardacre, E. V. Kondratenko, V. A. Kondratenko, C. McManus, S. Rogers, C. E. Stere, S. Chansai, Y.-C. Wang, S. J. Haigh, P. P. Wells, A. Goguet, Unraveling the H2 promotional effect on palladium-catalyzed CO oxidation using a combination of temporally and spatially resolved investigations, ACS Catalysis 8 (9) (2018) 8255–8262. `doi:10.1021/acscatal.8b01509`.

[41] M. A. Newton, S. Checchia, A. J. Knorpp, D. Stoian, W. van Beek, H. Emerich, A. Longo, J. A. van Bokhoven, On isothermality in some commonly used plug flow reactors for X-ray based investigations of catalysts, Catal. Sci. Technol. 9 (12) (2019) 3081–3089. `doi:10.1039/C9CY00464E`.

[42] R. Prins, A. Wang, X. Li, Introduction to heterogeneous catalysis, Vol. Vol. 1 of Advanced textbooks in chemistry, World Scientific and ICP Imperial College Press, London and Singapore and London, 2016.

[43] M. Appl, Ammonia, in: Ullmann's Encyclopedia of Industrial Chemistry, Wiley-VCH Verlag GmbH & Co. KGaA, Weinheim, Germany, 2000. `doi:10.1002/14356007.a02_143.pub2`.

[44] M. A. Benvenuto, H. Plaumann (Eds.), Industrial catalysis, De Gruyter, Berlin, 2021. `doi:10.1515/9783110542868`.

[45] Clariant Ltd. Basel, Steam methane reforming (20.01.2022).
URL `https://www.clariant.com/de/Business-Units/Catalysts/Syngas-Catalysts/Steam-Reforming`

[46] H. S. Fogler, Elements of chemical reaction engineering, 3rd Edition, Prentice-Hall international series in the physical and chemical engineering sciences, Prentice-Hall of India, 2006, 1999.

[47] D. E. Mears, Tests for transport limitations in experimental catalytic reactors, Industrial & Engineering Chemistry Process Design and Development 10 (4) (1971) 541–547. `doi:10.1021/i260040a020`.

[48] D. Mears, Diagnostic criteria for heat transport limitations in fixed bed reactors, Journal of Catalysis 20 (2) (1971) 127–131. `doi:10.1016/0021-9517(71)90073-X`.

[49] Website INEOS Chemicals - Base Chemicals (27.07.2022).
URL `https://www.ineos.com/industry/products/chemicals/base-chemicals/`

[50] H. Zimmermann, R. Walzl, Ethylene, in: Ullmann's Encyclopedia of Industrial Chemistry, Wiley-VCH Verlag GmbH & Co. KGaA, Weinheim, Germany, 2000. `doi:10.1002/14356007.a10_045.pub3`.

[51] C. A. Gärtner, A. C. van Veen, J. A. Lercher, Oxidative dehydrogenation of ethane: Common principles and mechanistic aspects, ChemCatChem 5 (11) (2013) 3196–3217. `doi:10.1002/cctc.201200966`.

[52] Website der BASF - Crackerproducts (27.07.2022).
URL `https://chemicals.basf.com/global/en/Petrochemicals/crackerproducts.html`

[53] Website der BASF - Steamcracker (27.07.2022).
URL `https://www.basf.com/global/de/who-we-are/organization/locations/europe/german-sites/ludwigshafen/production/the-production-verbund/Steamcracker.html`

[54] T. Ren, M. Patel, K. Blok, Olefins from conventional and heavy feedstocks: Energy use in steam cracking and alternative processes, Energy 31 (4) (2006) 425–451. `doi:10.1016/j.energy.2005.04.001`.

[55] I. Amghizar, J. N. Dedeyne, D. J. Brown, G. B. Marin, K. M. van Geem, Sustainable innovations in steam cracking: CO2 neutral olefin production, Reaction Chemistry & Engineering 5 (2) (2020) 239–257. `doi:10.1039/C9RE00398C`.

[56] Website of the Federal Government, More climate protection: climate-neutral eu by 2050 (27.07.2022).
URL `https://www.bundesregierung.de/breg-en/issues/climate-action/more-climate-protection-in-eu-1797114`

[57] Website der BASF - BASF, SABIC und Linde arbeiten gemeinsam an der Realisierung des weltweit ersten elektrisch beheizten Steamcracker-Ofens (27.07.2022).
URL `https://www.basf.com/global/de/who-we-are/sustainability/whats-new/sustainability-news/2021/basf-sabic-and-linde-join-forces-to-realize-wolds-first-electrically-heated-steam-cracker-furnace.html`

[58] G. Ertl, H. Knzinger, F. Schth, J. Weitkamp (Eds.), Handbook of Heterogeneous Catalysis, Wiley-VCH Verlag GmbH & Co. KGaA, Weinheim, Germany, 2008. `doi:10.1002/9783527610044`.

[59] S. F. Hkonsen, A. Holmen, Oxidative dehydrogenation of alkanes, in: G. Ertl, H. Knzinger, F. Schth, J. Weitkamp (Eds.), Handbook of Heterogeneous Catalysis, Wiley-VCH Verlag GmbH & Co. KGaA, Weinheim, Germany, 2008. `doi:10.1002/9783527610044.hetcat0171`.

[60] F. Cavani, N. Ballarini, A. Cericola, Oxidative dehydrogenation of ethane and propane: How far from commercial implementation?, Catalysis Today 127 (1-4) (2007) 113–131. `doi:10.1016/j.cattod.2007.05.009`.

[61] C. Baroi, A. M. Gaffney, R. Fushimi, Process economics and safety considerations for the oxidative dehydrogenation of ethane using the M1 catalyst, Catalysis Today 298 (2017) 138–144. `doi:10.1016/j.cattod.2017.05.041`.

[62] J. M. L. Nieto, The selective oxidative activation of light alkanes. From supported vanadia to multicomponent bulk V-containing catalysts, Topics in Catalysis 41 (1-4) (2006) 3–15. `doi:10.1007/s11244-006-0088-4`.

[63] A. Bielański, J. Haber, Oxygen in catalysis on transition metal oxides, Catalysis Reviews 19 (1) (1979) 1–41. `doi:10.1080/03602457908065099`.

[64] J. Haber, E. M. Serwicka, The role of oxygen in catalysis, Reaction Kinetics and Catalysis Letters 35 (1-2) (1987) 369–379. `doi:10.1007/BF02062172`.

[65] J. Haber, Molecular mechanism of heterogeneous oxidation — organic and solid state chemists' views, in: 3rd World Congress on Oxidation Catalaysis, Proceedings of the 3rd World Congress on Oxidation Catalysis, Vol. 110 of Studies in Surface Science and Catalysis, Elsevier, 1997, pp. 1–17. `doi:10.1016/S0167-2991(97)80966-4`.

[66] P. Mora-Briseño, G. Jiménez-García, C.-O. Castillo-Araiza, H. González-Rodríguez, R. Huirache-Acuña, R. Maya-Yescas, Mars van Krevelen mechanism for the selective partial oxidation of ethane, International Journal of Chemical Reactor Engineering 17 (7) (2019). `doi:10.1515/ijcre-2018-0085`.

[67] Y. Chen, D. Dang, B. Yan, Y. Cheng, Mixed metal oxides of M1 MoVNbTeOx and TiO2 as composite catalyst for oxidative dehydrogenation of ethane, Catalysts 12 (1) (2022) 71. `doi:10.3390/catal12010071`.

[68] P. Kube, B. Frank, S. Wrabetz, J. Kröhnert, M. Hävecker, J. Velasco-Vélez, J. Noack, R. Schlögl, A. Trunschke, Functional analysis of catalysts for lower alkane oxidation, ChemCatChem 9 (4) (2017) 573–585. `doi:10.1002/cctc.201601194`.

[69] R. Naumann d'Alnoncourt, L.-I. Csepei, M. Hävecker, F. Girgsdies, M. E. Schuster, R. Schlögl, A. Trunschke, The reaction network in propane oxidation over phase-pure MoVTeNb M1 oxide catalysts, Journal of Catalysis 311 (2014) 369–385. `doi:10.1016/j.jcat.2013.12.008`.

[70] J. S. Valente, H. Armendáriz-Herrera, R. Quintana-Solórzano, P. del Ángel, N. Nava, A. Massó, J. M. López Nieto, Chemical, structural, and morphological changes of a MoVTeNb catalyst during oxidative dehydrogenation of ethane, ACS Catalysis 4 (5) (2014) 1292–1301. `doi:10.1021/cs500143j`.

[71] B. C. Michael, D. N. Nare, L. D. Schmidt, Catalytic partial oxidation of ethane to ethylene and syngas over Rh and Pt coated monoliths: Spatial profiles of temperature and composition, Chemical Engineering Science 65 (12) (2010) 3893–3902. `doi:10.1016/j.ces.2010.03.033`.

[72] J.-Y. Luo, X. Hou, P. Wijayakoon, S. J. Schmieg, W. Li, W. S. Epling, Spatially resolving SCR reactions over a Fe/zeolite catalyst, Applied Catalysis B: Environmental 102 (1-2) (2011) 110–119. `doi:10.1016/j.apcatb.2010.11.031`.

[73] R. Horn, O. Korup, M. Geske, U. Zavyalova, I. Oprea, R. Schlögl, Reactor for in situ measurements of spatially resolved kinetic data in heterogeneous catalysis, The Review of scientific instruments 81 (6) (2010) 064102. `doi:10.1063/1.3428727`.

[74] O. Korup, S. Mavlyankariev, M. Geske, C. F. Goldsmith, R. Horn, Measurement and analysis of spatial reactor profiles in high temperature catalysis research, Chemical Engineering and Processing: Process Intensification 50 (10) (2011) 998–1009. `doi:10.1016/j.cep.2011.05.024`.

[75] J. Pottbacker, Resolving gradients in an ammonia oxidation reactor under industrial conditions, Ph.D. thesis, TUHH Universitätsbibliothek (2022). `doi:10.15480/882.4465`.

[76] J. Touitou, K. Morgan, R. Burch, C. Hardacre, A. Goguet, An in situ spatially resolved method to probe gas phase reactions through a fixed bed catalyst, Catal. Sci. Technol. 2 (9) (2012) 1811. `doi:10.1039/C2CY20141K`.

[77] J. Touitou, R. Burch, C. Hardacre, C. McManus, K. Morgan, J. Sá, A. Goguet, An in situ spatially resolved analytical technique to simultaneously probe gas phase reactions and temperature within the packed bed of a plug flow reactor, The Analyst 138 (10) (2013) 2858–2862. `doi:10.1039/C3AN00250K`.

[78] A. Goguet, C. Stewart, J. Touitou, K. Morgan, In situ spatially resolved techniques for the investigation of packed bed catalytic reactors: Current status and future outlook of Spaci-FB, in: Spatially Resolved Operando Measurements in Heterogeneous Catalytic Reactors, Vol. 50 of Advances in Chemical Engineering, Elsevier, 2017, pp. 131–160. `doi:10.1016/bs.ache.2017.05.001`.

[79] M. Serrer, M. Stehle, M. L. Schulte, H. Besser, W. Pfleging, E. Sarai, J. Grunwaldt, Spatially-resolved insights into local activity and structure of Ni-based CO2 methanation catalysts in fixed-bed reactors, ChemCatChem 13 (13) (2021) 3010–3020. `doi:10.1002/cctc.202100490`.

[80] F. Wolke, Y. Hu, M. Schmidt, O. Korup, R. Horn, E. Reichelt, M. Jahn, A. Michaelis, Spatially-resolved reaction profiles in fischer-tropsch synthesis – influence of operating conditions and promotion for iron-based catalysts, Catalysis Communications 158 (2021) 106335. `doi:10.1016/j.catcom.2021.106335`.

[81] A. Aquino, Liquid phase selective oxidation of propylene to propylene oxide on titanium silicalite catalyst in a compact profile reactor, Master thesis, Hambburg University of Technology (2021).

[82] Y. Dong, M. Geske, O. Korup, N. Ellenfeld, F. Rosowski, C. Dobner, R. Horn, What happens in a catalytic fixed-bed reactor for n-butane oxidation to maleic anhydride? insights from spatial profile measurements and particle resolved CFD simulations, Chemical Engineering Journal 350 (2018) 799–811. `doi:10.1016/j.cej.2018.05.192`.

[83] J. Touitou, F. Aiouache, R. Burch, R. Douglas, C. Hardacre, K. Morgan, J. Sá, C. Stewart, J. Stewart, A. Goguet, Evaluation of an in situ spatial resolution instrument for fixed beds through the assessment of the invasiveness of probes and a comparison with a micro-kinetic model, Journal of Catalysis 319 (2014) 239–246. `doi:10.1016/j.jcat.2014.09.006`.

[84] A. Aguilar-Tapia, S. Ould-Chikh, E. Lahera, A. Prat, W. Delnet, O. Proux, I. Kieffer, J.-M. Basset, K. Takanabe, J.-L. Hazemann, A new high temperature reactor for operando XAS: Application for the dry reforming of methane over Ni/ZrO2 catalyst, The Review of scientific instruments 89 (3) (2018) 035109. `doi:10.1063/1.4998929`.

[85] N. E. Tsakoumis, A. P. E. York, Chen, M. Rønning, Catalyst characterisation techniques and reaction cells operating at realistic conditions; towards acquisition of kinetically relevant information, Catal. Sci. Technol. 5 (11) (2015) 4859–4883. `doi:10.1039/C5CY00269A`.

[86] J. Becher, S. Weber, D. Ferreira Sanchez, D. E. Doronkin, J. Garrevoet, G. Falkenberg, D. Motta Meira, S. Pascarelli, J.-D. Grunwaldt, T. L. Sheppard, Sample environment for operando Hard X-ray Tomography—an enabling technology for multimodal characterization in heterogeneous catalysis, Catalysts 11 (4) (2021) 459. `doi:10.3390/catal11040459`.

[87] F. C. Meunier, The design and testing of kinetically-appropriate operando spectroscopic cells for investigating heterogeneous catalytic reactions, Chemical Society reviews 39 (12) (2010) 4602–4614. `doi:10.1039/b919705m`.

[88] Website Lightsources.org - light sources of the world (07.06.2023).
URL `https://lightsources.org/lightsources-of-the-world/`

[89] P. Willmott, An Introduction to Synchrotron Radiation, Wiley, 2019. `doi:10.1002/9781119280453`.

[90] H. Wiedemann, Overview of synchrotron radiation, in: H. Wiedemann (Ed.), Particle accelerator physics, Graduate Texts in Physics, Springer, Cham and Heidelberg and New York and Dordrecht and London, 2015, pp. 815–855. `doi:10.1007/978-3-319-18317-6_24`.

[91] L. Spieß, G. Teichert, R. Schwarzer, H. Behnken, C. Genzel, Moderne Röntgenbeugung: Röntgendiffraktometrie für Materialwissenschaftler, Physiker und Chemiker, 2nd Edition, Vieweg + Teubner, Wiesbaden, 2009.

[92] A. M. Beale, S. D. M. Jacques, B. M. Weckhuysen, Chemical imaging of catalytic solids with synchrotron radiation, Chemical Society reviews 39 (12) (2010) 4656–4672. `doi:10.1039/c0cs00089b`.

[93] C. R. A. Catlow, P. Wells, D. Gianolio, Synchrotron radiation techniques in catalytic science, Physical Chemistry Chemical Physics 22 (34) (2020) 18745–18746. `doi:10.1039/d0cp90186e`.

[94] M. A. Newton, Operando catalysis using synchrotron methods, Catalysis, Structure & Reactivity 3 (1-2) (2017) 2–4. `doi:10.1080/2055074X.2017.1281605`.

[95] ESRF Website - ESRF 4th generation synchrotron light source (19.10.2020).
URL `https://www.esrf.fr/about/synchrotron-science`

[96] DESY Website - how does a synchrotron radiation source work? (08.05.2017).
URL `https://photon-science.desy.de/research/students__teaching/primers/synchrotron_radiation/index_eng.html`

[97] C. G. Schroer, I. Agapov, W. Brefeld, R. Brinkmann, Y. C. Chae, H. C. Chao, M. Eriksson, J. Keil, X. Nuel Gavaldà, R. Röhlsberger, O. H. Seeck, M. Sprung, M. Tischer, R. Wanzenberg, E. Weckert, PETRA IV: the ultralow-emittance source project at DESY, Journal of synchrotron radiation 25 (Pt 5) (2018) 1277–1290. `doi:10.1107/S1600577518008858`.

[98] Financed research facility in germany, DESY (19.09.2022).
URL `https://www.research-in-germany.org/en/research-landscape/why-germany/research-infrastructure/DESY-%E2%80%93-Deutsches-Elektronen-Synchrotron.html`

[99] DESY Website - PETRA III: Facility information (30.08.2021).
URL `https://photon-science.desy.de/facilities/petra_iii/facility_information/index_eng.html`

[100] DESY Website - aerial view PETRA III, mediabank (30.08.2021).
URL `https://photon-science.desy.de/facilities/petra_iii/index_eng.html`

[101] DESY Website - storage rings as synchrotron radiation sources (02.02.2018).
URL `https://photon-science.desy.de/research/students__teaching/primers/storage_rings__beamlines/index_eng.html`

[102] DESY Website - accelerator overview, mediabank (19.09.2022).
URL `https://photon-science.desy.de/sites/site_photonscience/content/e62/e189219/e189248/e189421/e196711/e189440/accelerator_DESY_eng.png`

[103] ESRF Website - what is a beamline? (01.02.2017).
URL `https://www.esrf.fr/about/synchrotron-science/beamline`

[104] DESY Website - key parameters of undulators operated at PETRA III (11.08.2022). URL `https://photon-science.desy.de/research/technical_groups/undulators/undulators_at_petraiii/index_eng.html`

[105] DESY Website - PETRA III Beamlines (18.05.2022). URL `https://photon-science.desy.de/facilities/petra_iii/beamlines/index_eng.html`

[106] C. Garino, E. Borfecchia, R. Gobetto, J. A. van Bokhoven, C. Lamberti, Determination of the electronic and structural configuration of coordination compounds by synchrotron-radiation techniques, Coordination Chemistry Reviews 277-278 (2014) 130–186. `doi:10.1016/j.ccr.2014.03.027`.

[107] A. I. Frenkel, J. A. Rodriguez, J. G. Chen, Synchrotron techniques for in situ catalytic studies: Capabilities, challenges, and opportunities, ACS Catalysis 2 (11) (2012) 2269–2280. `doi:10.1021/cs3004006`.

[108] J. Als-Nielsen, Elements of modern X-ray physics, 2nd Edition, Wiley, Hoboken, 2011. `doi:10.1002/9781119998365`.

[109] G. Bunker, Introduction to XAFS, Cambridge University Press, 2011. `doi:10.1017/CBO9780511809194`.

[110] S. Calvin, XAFS for Everyone, CRC Press, Hoboken, 2013. `doi:10.1201/b14843`.

[111] D. C. Koningsberger (Ed.), X-ray absorption: Principles, applications, techniques of EXAFS, SEXAFS and XANES, Vol. 92 of A Wiley Interscience publication, Wiley, New York, 1988.

[112] V. K. Pecharsky, P. Y. Zavalij, Fundamentals of Powder Diffraction and Structural Characterization of Materials, Springer US, Boston, MA, 2009. `doi:10.1007/978-0-387-09579-0`.

[113] Y. Waseda, E. Matsubara, K. Shinoda, X-Ray Diffraction Crystallography: Introduction, Examples and Solved Problems, Springer Berlin Heidelberg, Berlin, Heidelberg, 2011.

[114] W. T. Elam, B. D. Ravel, J. R. Sieber, A new atomic database for X-ray spectroscopic calculations, Radiation Physics and Chemistry 63 (2) (2002) 121–128. `doi:10.1016/S0969-806X(01)00227-4`.

[115] D. L. Source, Diamond Light Source Website - powder diffraction for industry (20.09.2022). URL `https://www.diamond.ac.uk/industry/Industry-News/Latest-News/Synchrotron-Industry-News-Powder-Diffraction.html#`

[116] H. M. McNair, J. M. Miller, N. H. Snow, Basic Gas Chromatography, Wiley, 2019. `doi:10.1002/9781119450795`.

[117] C. F. Poole (Ed.), Gas chromatography, 2nd Edition, Handbooks in separation science, Elsevier, Amsterdam, 2021.

[118] P. de Coning, J. Swinley, A practical guide to gas analysis by gas chromatography, Elsevier, Amsterdam and Oxford and Cambridge, MA, 2019.

[119] Agilent Website - Agilent J&W PLOT Columns (18.09.2022). URL `https://www.agilent.com/en/product/gc-columns/plot-gc-columns`

[120] Agilent Website - eliminating the fear: Factor flame ionization detector ((07.06.2023)). URL `https://www.agilent.com/cs/library/eseminars/public/gc-detector-design-troubleshooting-flame-ionization-fid-theory-basics-gas-flows-july212020.pdf`

[121] J. H. Gross, Massenspektrometer, in: J. H. Gross (Ed.), Massenspektrometrie, Springer Berlin Heidelberg, Berlin, Heidelberg, 2013, pp. 129–244. `doi:10.1007/978-3-8274-2981-0_4`.

[122] C. Dass, Fundamentals of Contemporary Mass Spectrometry, John Wiley & Sons, Inc, Hoboken, NJ, USA, 2007. `doi:10.1002/0470118490`.

[123] M. Linscheid, Mass Spectrometry, in: H. Gnzler, A. Williams (Eds.), Handbook of Analytical Techniques, Wiley-VCH Verlag GmbH, Weinheim, Germany, 2001, pp. 579–626. `doi:10.1002/9783527618323.ch20`.

[124] Sasol Website - spheres and extrudates (17.09.2022). URL `https://www.sasolgermany.de/alumina-products/spheres-extrudates0/`

[125] B. Wollak, D. Espinoza, A. Dippel, M. Sturm, F. Vrljic, O. Gutowski, I. G. Nielsen, T. L. Sheppard, O. Korup, R. Horn, Catalytic reactor for operando spatially-resolved structure-activity profiling using high-energy XRD, Journal of synchrotron radiation 30 (2023) 571–581. `doi:10.1107/S1600577523001613`.

[126] B. Wollak, D. E. Doronkin, D. Espinoza, T. Sheppard, O. Korup, M. Schmidt, S. Alizadefanaloo, F. Rosowski, C. Schroer, J.-D. Grunwaldt, R. Horn, Exploring catalyst dynamics in a fixed bed reactor by correlative operando spatially-resolved structure-activity profiling, Journal of Catalysis 408 (2022) 372–387. `doi:10.1016/j.jcat.2021.08.029`.

[127] DESY Website - unified data sheet (23.06.2020). URL `https://photon-science.desy.de/facilities/petra_iii/beamlines/p64_advanced_xafs/unified_data_sheet/index_eng.html`

[128] B. Ravel, M. Newville, ATHENA, ARTEMIS, HEPHAESTUS: data analysis for X-ray absorption spectroscopy using IFEFFIT, Journal of synchrotron radiation 12 (Pt 4) (2005) 537–541. `doi:10.1107/S0909049505012719`.

[129] DESY Website - P07 the high energy materials science beamline of Helmholtz-Zentrum Hereon and DESY (20.07.2022). URL `https://photon-science.desy.de/facilities/petra_iii/beamlines/p07_high_energy_materials_science/index_eng.html`

[130] DESY Website - P21.1 high energy X-Ray Diffraction for physics and chemistry (19.07.2022). URL `https://photon-science.desy.de/facilities/petra_iii/beamlines/p21_swedish_materials_science/p211_high_energy_x_ray_diffraction_for_physics_and_chemistry/index_eng.html`

[131] D. Espinoza, B. Wollak, T. L. Sheppard, A. Dippel, M. Sturm, O. Gutowski, M. Schmidt, O. Korup, R. Horn, Catalytic profile reactor for multimodal operando measurements during periodic operation, ChemCatChem (2022). `doi:10.1002/cctc.202200337`.

[132] J. Kieffer, V. Valls, N. Blanc, C. Hennig, New tools for calibrating diffraction setups, Journal of synchrotron radiation 27 (Pt 2) (2020) 558–566. `doi:10.1107/S1600577520000776`.

[133] T. Degen, M. Sadki, E. Bron, U. König, G. Nénert, The HighScore suite, Powder Diffraction 29 (S2) (2014) S13–S18. `doi:10.1017/S0885715614000840`.

[134] J. Rodríguez-Carvajal, Recent advances in magnetic structure determination by neutron powder diffraction, Physica B: Condensed Matter 192 (1-2) (1993) 55–69. `doi:10.1016/0921-4526(93)90108-I`.

[135] D. Espinoza, Catalyst activity profiling using a compact spatial profile reactor, Master thesis, Hamburg University of Technology (2021).

[136] A. Katrib, P. Leflaive, L. Hilaire, G. Maire, Molybdenum based catalysts. I. MoO2 as the active species in the reforming of hydrocarbons, Catalysis Letters 38 (1-2) (1996) 95–99. `doi:10.1007/BF00806906`.

[137] J. G. Speight, Gasification reaction kinetics for synthetic liquid fuel production, in: Gasification for Synthetic Fuel Production, Elsevier, 2015, pp. 103–117. `doi:10.1016/B978-0-85709-802-3.00005-9`.

[138] T. Ressler, O. Timpe, T. Neisius, J. Find, G. Mestl, M. Dieterle, R. Schlögl, Time-resolved XAS investigation of the reduction/oxidation of MoO3x, Journal of Catalysis 191 (1) (2000) 75–85. `doi:10.1006/jcat.1999.2772`.

[139] E. Heracleous, A. A. Lemonidou, Homogeneous and heterogeneous pathways of ethane oxidative and non-oxidative dehydrogenation studied by temperature-programmed reaction, Applied Catalysis A: General 269 (1-2) (2004) 123–135. `doi:10.1016/j.apcata.2004.04.007`.

[140] T. Ressler, Bulk structural investigation of the reduction of MoO3 with propene and the oxidation of MoO2 with oxygen, Journal of Catalysis 210 (1) (2002) 67–83. `doi:10.1006/jcat.2002.3659`.

[141] T. Ressler, J. Wienold, R. E. Jentoft, F. Girgsdies, Evolution of defects in the bulk structure of MoO3 during the catalytic oxidation of propene, European Journal of Inorganic Chemistry 2003 (2) (2003) 301–312. `doi:10.1002/ejic.200390040`.

[142] M. Dieterle, G. Weinberg, G. Mestl, Raman spectroscopy of molybdenum oxides, Physical Chemistry Chemical Physics 4 (5) (2002) 812–821. `doi:10.1039/b107012f`.